East European Journal of Physics. **3.** 53-58 (2022)
DOI:10.26565/2312-4334-2022-3-07 ISSN 2312-4334

COMPREHENSIVE ASSESSMENT OF BIOLOGICAL SUBSTRATES OF PROFESSIONAL SICK PERSON GROUP BY CHEMOMETRIC AND NUCLEAR PHYSICAL METHODS[†]

Maryna F. Kozhevnikova*, Volodymyr V. Levenets, Oleksandr P. Omelnyk, Andriy O. Shchur
NSC "Kharkiv Institute of Physics & Technology" NASU
1, Academichna str., 61108, Kharkiv, Ukraine
**Corresponding Author: marko@kipt.kharkov.ua*
Received July 3, 2022; accepted August 15, 2022

The article deals with the influence of negative factors of working conditions on the health status of NSC KIPT personnel when working with beryllium. Beryllium and its compounds render a general toxic, allergenic and carcinogenic effect on the organism. The high biological activity and toxicity of Be is due to its chemical activity and penetrating ability. The chronic professional disease such as berylliosis occurs as a result of prolonged systematic exposure on the organism of adverse factors. Elemental analysis of biosubstrates provides important information, that in combination with symptoms and other laboratory parameters, can help in the early diagnostics of physiological violations associated with metabolic disorders and exposure of toxic elements. The blood and hair samples were taken from 28 people, among which 5 patients were selected as a control group, and a group of 23 people were former employees of the beryllium production. The content of chemical elements in the biological substrates (blood and hair) of employees was determined by nuclear-physical methods. An elemental analysis was performed on the analytical nuclear physics complex appliance "Sokol". The methods based on registration of characteristic X-ray radiation of atoms and γ-radiation of nuclei excited by accelerated protons is used. After measurements, data arrays were obtained on the content of 14 chemical elements (N, Na, S, Cl, K, Ca, Ti, Mn, Fe, Cu, Zn, Br, Sr, Pb) in blood and hair. The processing of data arrays was carried out using the principal component method which is related to chemometrics technologies. As a result of the work, an analytical program was composed in MATLAB codes which were used to determine the content of elements in biosubstrates that are most sensitive to changes in external conditions. This made it possible to identify certain groups of patients who have different health state indicators, as well as to see the similarities or differences between patients depending on the different concentrations of chemical elements in the blood or hair.
Keywords: elemental analysis, biological substrates, berylliosis, characteristic X-ray radiation of atoms, chemometrics, principal component method.
PACS: 87.64.-t

Despite compliance with safety regulations, which practically exclude the interaction of personnel with harmful substances, the problem of professional diseases remains very relevant. Since the existence of the nuclear industry, NSC KIPT employees have been working with beryllium (Be). Be has high strength, heat capacity and heat resistance, high anti-corrosion properties, resistant to radiation, and has used as addition to metal alloys. Under production conditions, employees are exposed to soluble and sparingly soluble Be compounds, which differ significantly in their toxicological properties. The main intake of Be occurs by inhalation. With oral intake, sparingly soluble Be compounds are formed in the intestine. With the inhalation route of intake of soluble compounds, most part of Be remains in the lungs and tracheobronchial lymph nodes, a smaller part is distributed in the bones, liver, and kidneys.

Beryllium is determined in biological substrates both in practically healthy people who have worked in contact with the metal or its compounds, and in people who have undergone intoxication with its compounds, in patients with berylliosis and in people who lived in coal mining areas with a high Be content. Beryllium and its compounds can have a general toxic, allergenic and carcinogenic effect on the body. The high biological activity and toxicity of Be is due to its chemical activity and penetrating ability.

An essential toxicological feature of insoluble Be compounds is the lack of correlation between the dose of the affecting substance and the possible development of the disease. The development of berylliosis is often observed in people who worked with metal or its alloys, the content of which in the air did not always exceed the maximum allowable concentration. The occurrence of the disease is possible both after short-term contact with metal (from 6 hours to 2-3 weeks), and after long-term contact (within 10-20 years).

The chronic occupational disease such as berylliosis occurs as a result of long-term systematic exposure of the body to adverse factors. Berylliosis is characterized by diverse clinical symptoms with a predominance of signs of lung damage, a recurrent course of the disease, and damage to many organs.

For the correct diagnosis of professional disease, it is especially important to carefully study sanitary and hygienic working conditions, the patient's history, his "professional route", which includes all types of work performed by him from the beginning of his labor activity [1]. Currently, there is a group of professional patients with berylliosis among the former and current employees of the NSC KIPT.

[†] ***Cite as***: M.F. Kozhevnikova, V.V. Levenets, O.P. Omelnyk, and A.O. Shchur, East Eur. J. Phys. **3**, 53 (2022), https://doi.org/10.26565/2312-4334-2022-3-07

Heavy metal compounds can enter the body in various ways such as inhalationly, orally, parenterally, as well as through the skin and mucous membranes. They are excreted most often very slowly, through the kidneys, liver, salivary and sweat glands, mucous membranes, which is accompanied by damage to these organs.

Recently, along with blood tests, there has been increasing interest in the study of hair to identify the state of microelement metabolism in the body and the toxic effects of individual heavy metals [2-6]. The available data show that the content of elements in hair reflects the elemental status of the organism as a whole, and hair samples are an integral indicator of mineralogical metabolism.

Spectral analysis of hair for trace elements is a study of the content of "useful" and "harmful" chemical elements in the human body by hair. Such chemical elements as K, Ca, Fe, Cu, Zn, Cr, Se are "useful" minerals that ensure the normal functioning of the body, but a toxic elements of industrial origin Hg, Cd, Pb, As are poisonous.

An elemental analysis of biosubstrates (blood and hair) provides important information that, in combination with symptoms and other laboratory parameters, can help in the early diagnosis of physiological disorders associated with metabolic disorders and exposure to toxic elements.

The aim of this work is a comprehensive assessment of the biological substrates of a group of professional patients by chemometric and nuclear physic methods.

SUBJECT OF STUDY AND INPUT DATA

The content of chemical elements in biological substrates (blood and hair) of employees was determined by nuclear-physical methods. Blood and hair samples were taken from 28 people, among which 5 patients were selected as a control group, and a group of 23 people were former workers in the beryllium production (9 women and 14 men). The age of the examined patients was from 52 to 78 years. Samples were prepared according to standard technology. The measurements were carried out at analytical nuclear physics complex “Sokol” of the NSC KIPT [7]. Methods based on the registration of the characteristic X-ray radiation of atoms (it is method1) and γ-radiation of nuclei excited by accelerated protons (it is method 2) were used. Elements with an atomic number of 16 or more were determined using the method 1, elements with an atomic number less than 16 were determined by the method 2. The spectra were measured at a proton beam energy of 1.7 MeV, a current of 20..50 nA, and a proton charge on the target of 100..150 μC. The radiation was recorded by Si (Li) and Ge (Li) detectors. After the measurements, data arrays were obtained on the content of elements in the blood and hair. In the range of elements from N to Pb, 14 elements (N, Na, S, Cl, K, Ca, Ti, Mn, Fe, Cu, Zn, Br, Sr, Pb) were selected for further processing.

SPATIAL ANALYSIS METHODS

Currently, when processing large data arrays, the possibilities of chemometrics are often used. Chemometrics is a scientific discipline that applies mathematical, statistical and other methods based on formal logic to construct or select optimal measurement methods and experimental designs, as well as to extract the most important information in the analysis of experimental data [8]. One of the main objects that chemometrics works with is chemical data. However, over time, chemometrics has become an independent discipline. Two circumstances contributed to this such as the complication of the mathematical apparatus used in chemometrics, and the emergence of numerous applications in which the chemometric approach is successfully applied in areas far from chemistry [9].

Chemometrics is closely related to mathematics. Therefore, chemometrics has found numerous applications in various fields related to and far from chemistry, for example, in multivariate statistical control of processes [10], in image analysis [11], and in biological applications [12]. It is used in physical chemistry to study kinetics [13], in organic chemistry to predict the activity of compounds based on their structure (QSAR – quantitative structure-activity relationship) [14], in polymer chemistry [15], in theoretical and quantum chemistry [16] .

Data is the main object that chemometrics works with. The simplest case is one-dimensional data, i.e. just one number. A more complex case is multidimensional, unimodal data, i.e. a set of results from several measurements related to the same sample. The next most common data type is bimodal data, which is represented by a 2D matrix, a table of numbers with I rows and J columns. Recently, much attention has been paid to three (or more) modal data. The main task of chemometrics is to extract the necessary information from the data. The concept of information is key in chemometrics. What is information depends on the purpose of the problem being solved. For example, in some cases it is sufficient to know that the desired substance is present in the system, while in others it is necessary to obtain quantitative values. All data contains noise, such as errors that hide useful information.

The principles of the chemometric approach to data analysis: 1) the use of a multidimensional approach in designing experiments and analyzing their results; 2) the definition of what is considered noise and what is information is decided taking into account the goal and the methods used to achieve it.

The traditional approach to processing measurement results is to identify individual, especially significant quantities. To select useful information in chemometrics, data compression methods are used. The idea behind this approach is to represent the original data using new hidden variables. In this case, two conditions must be met. Firstly, the number of new variables should be significantly less than the number of original variables, and, secondly, the losses from such data compression should be comparable to the noise in the data. Data compression methods allow you to present useful information in a more compact form that is convenient for visualization and interpretation.

The most popular method of data compression is principal component analysis (PCA), which underlies some other similar chemometric methods [17].

From a mathematical point of view, the method of principal component analysis is a decomposition of the original 2D matrix X, i.e. its representation as a product of two 2D matrices T and P [18]:

$$X = TP^t + E = \sum_{a=1}^{A} t_a p_a^t + E \,, \tag{1}$$

where T is the score matrix; P is the load matrix; E is the matrix of residuals.

The transposition operation is denoted by the superscript t. The number of columns t_a in matrix T and p_a in matrix P is equal to the effective rank of matrix X. A is the number of principal components, and it is less than the number of columns in matrix X.

To illustrate a method PCA, a dataset should be considered. It is containing only two variables x_1 and x_2 that are strongly correlated. On Figure 1 (a) these data are presented in original coordinates. On Figure 1(b) the same data are shown in new coordinates. The load vector p_1 of the first principal component (PC1) determines the direction of the new axis along which the greatest data change occurs. The projections of all initial points onto this axis make up the vector t_1. The second principal component p_2 is orthogonal to the first, and its direction (PC2) corresponds to the largest change in the residuals by segments which are perpendicular to the p_1 axis (it is shown on Figure 1 (b)).

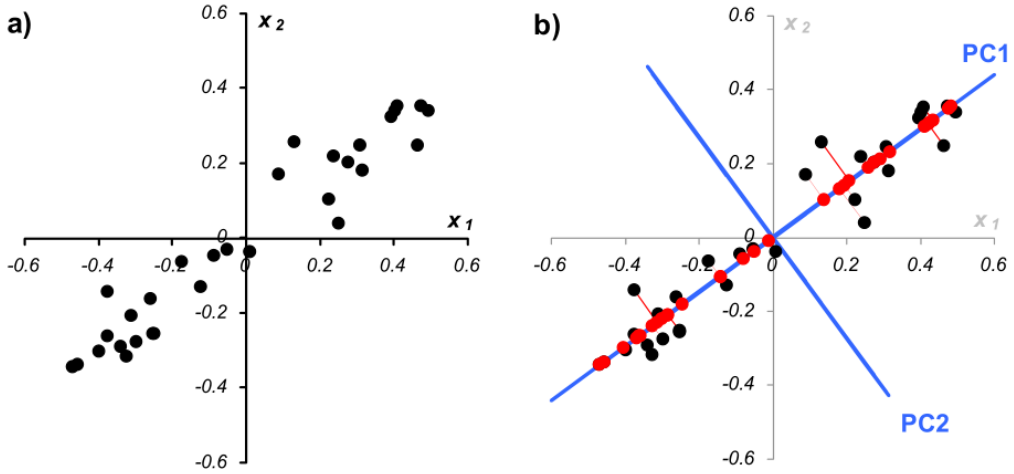

Figure 1. Graphical representation of the data set in the method of principal components: a) data in the initial coordinates of the variables x_1 and x_2; b) data in principal component coordinates [18]

An application of principal components analysis method is carried out sequentially, step by step. At each step, the residuals E_a are examined, and among them the direction of the greatest change is selected. The data are projected onto this axis, new residuals are calculated, and so on. This algorithm is called non-linear iterative projections by alternating least-squares (NIPALS) [19].

Principal component method can be interpreted as the projection of data onto a subspace of lower dimension. The residuals E arising in this case are considered as noise that does not contain significant information.

When examining data using the PCA method, special attention is paid to the graphs of accounts and loads. They carry information useful for understanding how the data is structured. On the score chart, each sample is depicted in coordinates (t_i, t_j), most often as (t_1, t_2). The proximity of two points means their similarity, i.e. positive correlation. Points located at right angles are uncorrelated, and diametrically opposite points are negatively correlated.

If the score chart is used to analyze the relationship of samples, then the load chart is used to study the role of variables. On the load graph, each variable is displayed as a dot in the coordinates (p_i, p_j), for example (p_1, p_2). By analyzing it in a similar way to a graph of accounts, one can understand which variables are related and which are independent. However, the most informative is the joint study of paired graphs of scores and loads [18].

RESULTS OF THE RESEARCH

The processing of data arrays obtained by nuclear-physical methods was carried out in order to determine the content of elements in human biosubstrates that are most sensitive to changes in external conditions. Based on the analysis of the obtained data, it was supposed to study the possibilities of using nuclear-physical methods for analyzing the composition of a substance for diagnosing certain types of diseases.

For a comprehensive assessment of the data obtained by nuclear-physical methods, the Analytica program has been developed, which implements the selection in a given factor space of the initial features of the m main components, or generalized features.

The Analytica program was created in MATLAB package codes. The process of data processing using the program includes the following steps:

1) a calculation of probabilistic-statistical values: mean, variance, deviation, variation;
2) a determination of the correlation matrix and correlation coefficients;
3) a calculation of eigenvalues for the correlation matrix;
4) using the NIPALS function, the obtaining a matrix of loads and a matrix of accounts;
5) a construction of graphs of accounts and loads.

When processing the obtained data, it was revealed that the hair is a more informative object, therefore, it is for this object the application of the principal component method is illustrated.

In the general case for biological objects it is rather difficult to determine the content of elements in the norm. Even when labeled, this value varies greatly for the control group as well. But the ratio of the contents of a number of elements is characteristic and is very constant. It is these relationships that can serve as an indicator of changes in the body's metabolism. In the process of data processing, various pairs of elements were selected, but normalization to the content of total N turned out to be the most informative. When processing the initial data for hair with normalization to N, a 28 × 13 matrix was compiled, where 28 is the number of patients, 13 is the number of chemical elements. Not included in the statistical processing of As and Cd, because the content of these elements is at the boundary and below the limits of detection.

According to the developed data processing algorithm, the eigenvectors (or load vectors) in the new coordinate system were determined. The coordinates of the samples for each component were calculated, which shows in what logic this or that component determines the structure of the samples and their position relative to each other.

The calculations were made for all components, allowing you to see how the samples relate to each other in one-dimensional (within one component) and two-dimensional spaces (planes formed by two components). The position of a single sample on a particular component was examined, as well as the percentage of features for the sample that explains the component. By varying the various main components, results were obtained linking the ratio of the content of separate elements in the hair with the presence of professional disease.

Considering the load vectors, we can conclude that in the first vector the load of element S is 86.2%, in the second vector the load Ca is 80%. Therefore, within the framework of component 1, the S index (it has the largest positive weight) acts as the most significant index. Within the framework of component 2 it is Ca, i.e. the following chemical elements predominate in the hair: S, Ca.

On Figure 2 shows the projection of the structure of hair samples in terms of elemental composition onto the plane of the principal components (1 comp and 2 comp).

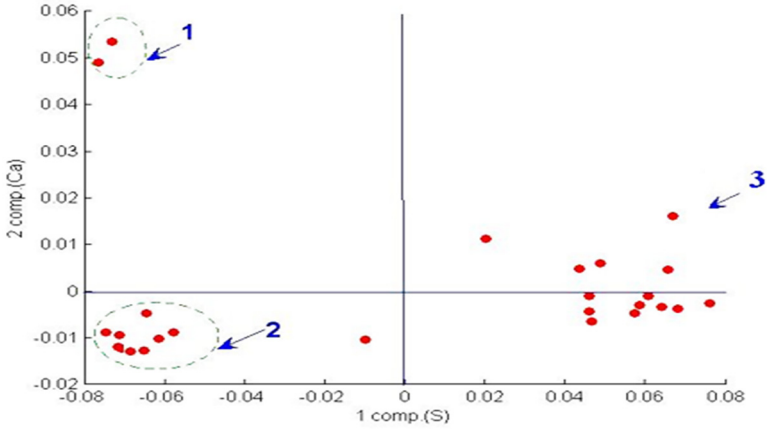

Figure 2. Chart of accounts for the data array on the content of chemical elements in the hair of 28 patients

On the given graph of scores, all points are located along the first principal component and form three groups. Group number 2 includes patients of the control group who do not have deviations in their state of health. They are characterized by a relatively low content of Ca and S. The first group of patients has a high content of Ca and low S and located apart. Based on the data set on the composition of the hair of these patients, it could be assumed that their hair was dyed (this was later confirmed). The third group includes patients with a certain professional disease. They are characterized by an increased content of S in the hair.

An application of the principal components method allows us to draw a conclusion about the microelemental state of the human body. Any pathology or any deviation in health is caused either by a deficiency of vital (essential) elements, or an excess of both essential and toxic microelements. Such imbalance of macro- and microelements has received its unifying name as microelementosis [20]. For example, it follows from the processed data that a group of patients with a professional disease is characterized by a higher content of N, K, Fe in the blood than in patients of the control group. The information [21] that an excess of Zn can lead to a deficit of Cu and Fe is confirmed, and, conversely, an excess of

Fe leads to a deficiency of Cu and Zn. For patients with a professional disease, there is an increased content of S in the hair than in patients of the control group.

The majority of patients (when examining hair samples) have approximately the same Ca/Mn ratio, in patients with an professional disease the Mn content is slightly increased. Ca content remains approximately the same as in patients in the control group. In the composition of the hair of patients with a professional disease, the content of Fe is increased, while the content of Ca is the same as in patients of the control group. It has been confirmed that an excess of calcium in the hair occurs when it is intensively excreted from the body [21].

CONCLUSIONS

The content of chemical elements in biological substrates (blood and hair) of 28 employees with a professional disease was determined by nuclear-physical methods. After the measurements, data arrays were obtained on the content of elements in the blood and hair. In the range of elements from N to Pb, 14 elements (N, Na, S, Cl, K, Ca, Ti, Mn, Fe, Cu, Zn, Br, Sr, Pb) were selected.

For complex data evaluation, the Analytica program has been developed, which implements the principal component method. The principal component method is effective in identifying the content of the main components of each sample and allows you to present useful information in a more compact form that is convenient for visualization and interpretation. Thus, with the help of graphs of accounts, certain groups of patients who have different indicators of health status are clearly identified. From the processed data, it follows that the group of patients with professional diseases is characterized by a higher concentration of N, K, Fe in the blood and an increased content of S in the hair than in patients of the control group.

It follows from the obtained results that hair is a more informative object than blood. Unlike blood, the chemical composition of hair is more stable. The study of hair shows the level of not only vital, but also conditionally essential, as well as toxic and potentially toxic trace elements.

The use of nuclear-physical methods and the mathematical apparatus of chemometrics made it possible to obtain information on the microelemental state of professional patients. As a result of the study, a conclusion was made about the possibility of using nuclear physics methods in the diagnosis of professional diseases.

Acknowledgements

This work has been supported organization and concret peoples: SMSP №13, which has selected of bloods; Avramenko N.A. who has done targets; Glazunov L.S., Kuzmenko V.V., who has works on “Sokol”.

ORCID IDs

Maryna F. Kozhevnikova, https://orcid.org/0000-0003-2464-3847;
Volodymyr V. Levenets, https://orcid.org/0000-0002-6439-0576;
Oleksandr P. Omelnyk, https://orcid.org/0000-0003-2467-3632;
Andriy O. Shchur, https://orcid.org/0000-0002-6619-4069;

REFERENCES

[1] V.V. Kosarev, and S.A. Babanov, *Профессиональные болезни: Учеб. Пособие* [*Professional diseases: textbook*], (Vuzovsky textbook, INFRA-M, Moscow, 2011), pp. 252. (in Russian)
[2] E.A. Luzhnikov, *Медицинская токсикология* [*Medical toxicology*], (GEOTAR-Media, Moscow, 2014), pp. 928. (in Russian)
[3] N. Singh, V.K. Gupta, A Kumar, and B. Sharma, Front. Chem. **5**(70), (2017). https://doi.org/10.3389/fchem.2017.00070
[4] A.V. Skalny, *Микроэлементозы человека (диагностика и лечение)* [Human microelementosis (diagnosis and treatment)], (M.: KMK, 2001), 96 p. (in Russian)
[5] S.L. Gerstenberger, C.L. Cross, D.D. Divine, M.L. Gulmatico, and A.M. Rothweiler, Environmental Toxicology, **21**, 583 (2006). https://doi.org/10.1002/tox.20221
[6] S.X. Chen, C.L. Wiseman, D. Chakravartty, and D.C. Cole, Int. J Environ. Res. Public Health, **14**(3), 277 (2017), https://doi.org/10.3390/ijerph14030277
[7] V.N. Bondarenko, L.S. Glazunov, A.V. Goncharov, A.V. Zats, V.Ya. Kolot, V.V. Kuzmenko, V.V. Levenets, A.P. Omelnik, V.M. Pistryak, V.I. Sukhostavets, and A.A. Shchur, Scientific Vedomosti. Series: Physics, **2**(15), 86 (2001). (in Russian)
[8] D.L. Massart, B.G.M. Vandeginste, S.M. Deming, Y. Michotte, and L. Kaufman, *Chemometrics: A Textbook,* (Elsevier: Amsterdam, 1988), pp. 464.
[9] O. Rodionova, S. Kucheryavskiy, and A. Pomerantsev, Chemom. Intell. Lab. Syst, **213**, 104304 (2021). https://doi.org/10.1016/j.chemolab.2021.104304
[10] P. Nomikos, and J.F. MacGregor, American Inst. Chem. Engin. J. **40**(8), 1361 (1994). https://doi.org/10.1002/aic.690400809
[11] P. Geladi, K. Esbensen, J. Chemom. **5**, 97-103 (1991). https://doi.org/10.1002/cem.1180050206
[12] D. Granato, P. Putnik, D.B. Kovacevic, J.S.V. Calado, R.S. Rocha, A.G. Da Cruz, B. Jarvis, O.Ye Rodionova, and A. Pomerantsev, Comp. Rev. Food Sc. Food Saf. **17,** 663-677 (2018), https://doi.org/10.1111/1541-4337.12341
[13] O.E. Rodionova, A.L. Pomerantsev, Kinetics and catalysis, **45**, 485 (2004). (in Russian)
[14] H.-L. Koh, W.-P. Yau, P.-S. Ong, A. Hegde, Drug Discov. Today, **8**, 889 (2003). https://doi.org/10.1016/S1359-6446(03)02846-0
[15] A.L. Pomerantsev, and I.E. Rodionova, Chemom. Intell. Lab. Syst. **79,** 73 (2005). https://doi.org/10.1016/j.chemolab.2005.04.004
[16] L.A. Gribov, *Математические методы и ЭВМ в аналитической химии* [*Mathematical methods and computers in analytical chemistry*], (Nauka, Moscow, 1989), pp. 302. (in Russian)
[17] S. Wold, K. Esbensen, and P.Geladi, Chemom. Intell. Lab.Syst. **2,** 37 (1987). https://doi.org/10.1016/0169-7439(87)80084-9

[18] K.H. Esbensen, *Multivariate Data Analysis – In Practice 5-th Ed.*, (Camo, Oslo, 2012), pp. 588.
[19] O.E. Rodionova, and A.L. Pomerantsev, Advances in chemistry, **75**, 302 (2006). (in Russian)
[20] A.P. Avtsyn, A.A. Zhavoronkov, M.A. Rish, L.S. Strochkova, *Микроэлементозы человека* [*Microelementoses human*], (Medicine, Moscow, 1991), pp. 496. (in Russian)
[21] M.N. Bates, J.W. Hamilton, J.S. LaKind, P. Langenberg, M. O'Malley, and W. Snodgrass, Environmental Health Perspectives, 113, **11**, 1615-1621 (2005). https://doi.org/10.1289/ehp.8197

КОМПЛЕКСНА ОЦІНКА БІОЛОГІЧНИХ СУБСТРАТІВ ГРУПИ ПРОФХВОРИХ ХЕМОМЕТРИЧНИМ ТА ЯДЕРНО-ФІЗИЧНИМ МЕТОДАМИ

М.Ф. Кожевнікова, В.В. Левенець, О.П. Омельник, А.О. Щур
Національний науковий центр «Харківський фізико-технічний інститут», НАНУ
1, вул. Академічна, 61108, Харків, Україна

В роботі розглядається вплив негативних факторів виробничих умов на стан здоров'я персоналу ННЦ ХФТИ при роботі з берилієм. Берилій та його сполуки здійснюють загальнотоксичний, алергенний та канцерогенний вплив на організм. Висока біологічна активність та токсичність берилію обумовлена його хімічною активністю та проникаючою здатністю. Хронічне професійне захворювання берилліозу виникає як результат тривалого систематичного впливу на організм несприятливих факторів. Елементний аналіз біосубстратів надає важливу інформацію, яка в поєднанні із симптомами та іншими лабораторними показниками, може допомогти в ранній діагностиці фізіологічних порушень, пов'язаних із порушеннями обміну речовин та впливом токсичних елементів. Проби крові та волосся отобрано у 28 людей, серед яких 5 пацієнтів обрано в якості контрольної групи, а група з 23 людей – колишні працівники берилліевого виробництва. Ядерно-фізичними методами визначено вміст хімічних елементів у біологічних субстратах співробітників (кров і волосся). Елементний аналіз виконано на аналітичному ядерно-фізичному комплексі «Сокол». Використовувались методи, засновані на реєстрації характеристичного рентгенівського випромінювання атомів і γ-випромінювання ядер, що збуджуються швидкими протонами. Після проведення вимірювань отримано масиви даних по вмісту 14 хімічних елементів (N, Na, S, Cl, K, Ca, Ti, Mn, Fe, Cu, Zn, Br, Sr, Pb) в крові та волоссі. Обробка масивів даних проводилась при використанні методу головних компонентів, який має відношення до технологій хемометрики. В результаті роботи була складена програма Analytica в кодах MATLAB, яка використовувалась для визначення вмісту в біосубстратах елементів, найбільш чутливих до зміни зовнішніх умов. Це дозволило виявити певні групи пацієнтів, які мають різні показники стану здоров'я, а також побачити схожість або відмінність між пацієнтами в залежності від концентрації хімічних елементів в крові чи волоссі.

Ключові слова: елементний аналіз, біологічні субстрати, берилліоз, характеристичне рентгеновське випромінювання атомів, хемометрика, метод головних компонентів.

EAST EUROPEAN JOURNAL OF PHYSICS. **3.** 59-66 (2022)
DOI:10.26565/2312-4334-2022-3-08 ISSN 2312-4334

MANUFACTURING FEATURES AND CHARACTERISTICS OF URANIUM DIOXIDE PELLETS FOR SUBCRITICAL ASSEMBLY FUEL RODS[†]

Igor A. Chernov[a], Anton V. Kushtym[a], Volodymyr R. Tatarinov[a], Dmytro V. Kutniy[b]
[a]*«Nuclear Fuel Cycle» Science and Technology Establishment*
[b]*Scientific and Technical Service of Nuclear Materials and Export Control*
National Science Center «Kharkiv Institute of Physics and Technology»
1, Akademichna St., Kharkiv, 61108, Ukraine
**Corresponding Author: chernov@kipt.kharkov.ua*
Received August 1, 2022; accepted August 27, 2022

The influence of technological processes and manufacturing of uranium dioxide fuel pellets for fuel elements for experimental fuel assembly (FA-X) which was designed as an alternative fuel for the nuclear research installation (NRI) "Neutron Source Controlled by Electron Accelerator" were investigated. Unlike standard production processes of UO_2 pellets, the special feature fabrication process of this nuclear fuel type is production of uranium dioxide powder with enrichment of 4.4 %wt. of ^{235}U achieved by mixing of two batches of powders with different uranium contents: 0.4 %wt. ^{235}U and 19.7%wt. ^{235}U, as well as ensuring the required tolerance of fuel pellets without the use of machining operations. A set of design and process documentation were developed in the R&D Center at NSC KIPT. Experimental stack of fuel pellets, fuel elements and a pilot fuel assembly FA-X were fabricated and designed to be compatible and interchangeable with VVR-M2 fuel assembly adopted as a standard assembly for the first fuel loading at the "Neutron Source Driven by an Electron Accelerator" FA. As opposition to the variant of VVR-M2 fuel assembly which consisted of three fuel rods of tubular shape with dispersion composition UO_2-Al, FA-X accommodates six fuel rods of pin-type with UO_2 pellet which located in the zirconium cladding (E110) as the closest analogue of fuel rods of VVER-1000 power reactor. Inside cladding locate a 500 mm high fuel stack which is secured against displacement by a spacer. In the basic variant of FA-X the fuel pellets are made of UO_2 with ^{235}U enrichment near 4.4 %wt.
Keywords: fuel rod, pellet, fuel assembly, powder, uranium dioxide, enrichment, mixture uniformity, density, microstructure.
PACS: 28.41.Bm, 28.50.Dr, 29.25.Dz, 47.51.+a, 81.05.Je, 81.20.Ev, 83.50.Xa

SUBCRITICAL ASSEMBLY OF THE "NEUTRON SOURCE" NUCLEAR FACILITY

The subcritical assembly (SCA) of the "Accelerator Driven Neutron Source" nuclear facility serves to multiply primary neutrons from the fission of uranium-235 and includes: a core of fissile material, a moderator and reflector of neutrons, and a coolant [1].

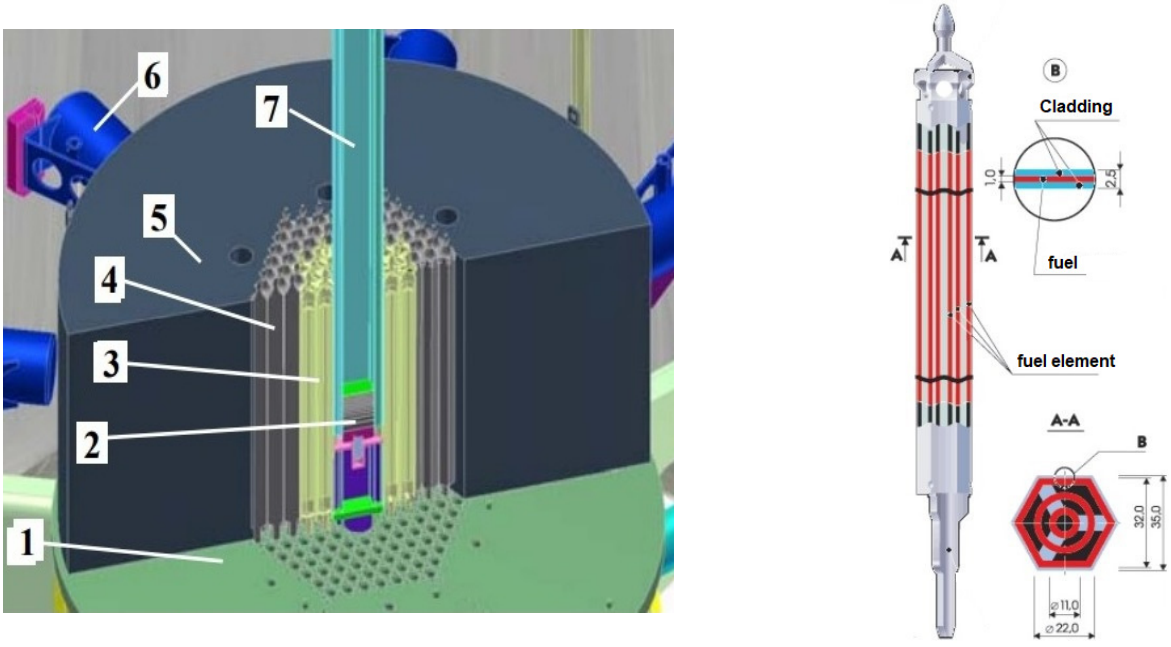

a b

Figure 1. 3D model of the subcritical assembly (a) [1]: 1 - baseplate; 2 - neutron-forming target; 3 - VVR-M2 type fuel assembly; 4 - beryllium reflectors; 5 - graphite reflector; 6 - neutron channel; 7 - vacuum channel of electron beam; standard fuel assemblies of VVR-M2 type (b) [2]

[†] ***Cite as:*** I.A. Chernov, A.V. Kushtym, V.R. Tatarinov, and D.V. Kutniy, East Eur. J. Phys. **3**, 59 (2022), https://doi.org/10.26565/2312-4334-2022-3-08

DESCRIPTION OF FA-X DESIGN

As an analog of fuel element for VVER-1000 reactor was choose a good approbated with characteristics was selected a fuel element FA-X (Fig. 2a, c) [3]: the length of the fuel element was decreased from 3800 mm to 600 mm, the height of fuel stack - from 3530 mm to 500 mm. Similar parameters of fuel elements are as follows: material and diameter of cladding - zirconium alloy E110, Ø 9.1 mm, type of the fuel composition - UO_2, enrichment of pellets with uranium-235 isotope – 4.4 %. Productions of UO_2 pellets according with technical requirements [4], must have specified characteristics (Fig. 2b): appearance, geometry, density, uranium content, oxygen coefficient, enrichment, and chemical composition.

As part of project R515 "Design and technology for fabrication of fuel pellets and fuel assemblies for subcritical assembly and testing for reliability and safety" the laboratory technology for fabrication of uranium dioxide pellet fuel with the required set of characteristics including pellet geometric dimensions, enrichment, density, uranium content was developed.

The peculiarity of the fabrication process of fuel pellets with content of ^{235}U near 4.4%wt. for FA-X is the preparation of uranium dioxide powder by mixing of two powder batches with enrichment: 0.4%wt. ^{235}U and 19.7 %wt. ^{235}U. Another peculiarity of the technology was obtaining of samples with required geometric dimensions within the tolerance range without additional mechanical operations.

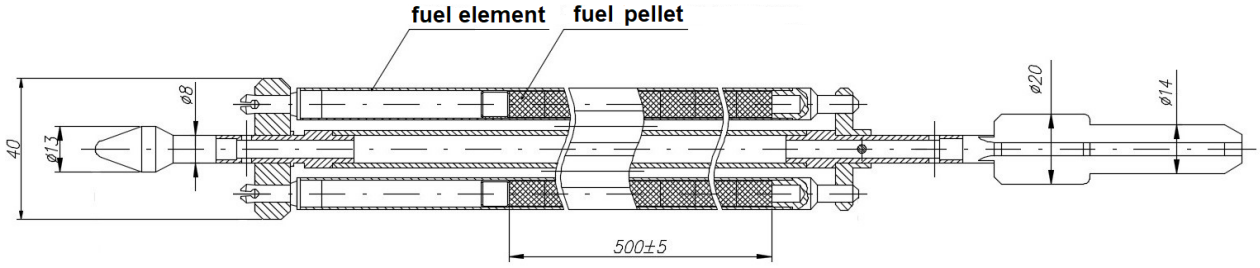

a

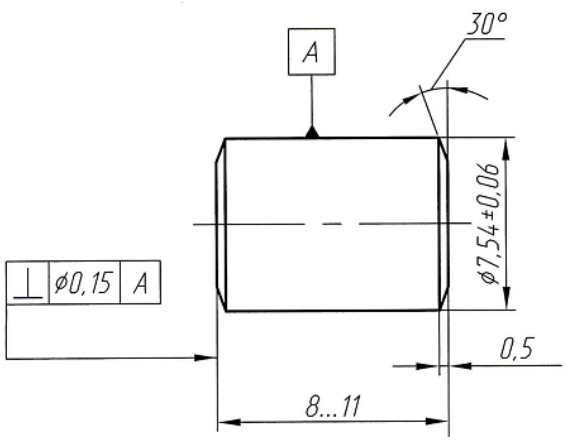

diameter 7.48-7.60 mm
height 8-11 mm
density 10.30-10.60 g/cm^3
enrichment 4.40-4.43% wt. ^{235}U
uranium content – more 87.4%
oxygen coefficient 1.92-2.05

b

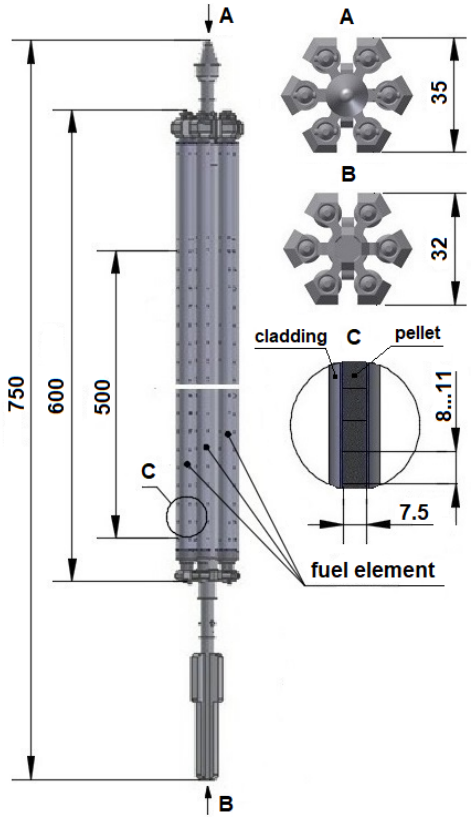

c

Figure 2. Fuel assembly (FA-X) (a — common view, c - 3D-model); UO_2 pellet and main requirements (b)

MATERIALS AND RESEARCH METHODS

Uranium dioxide powders with different ^{235}U content - 19.905±0.224 %wt. and 0.454±0.044 %wt. were used as starting materials. Fuel pellets were formed by two-sided cold pressing in a steel mold with a diameter of 10 mm. Fuel pellets were sintered in furnace with graphite heater at 1700 ºC in vacuum with preliminary annealing of binder at 600 ºC.

The control of the uranium dioxide powder mixtures and fuel pellets enrichment with isotope ^{235}U was carried out according to the methodology №07-123:2011 "Uranium and its compounds. Methods for measuring the mass fraction of uranium-235 using semiconductor gamma spectrometer CANBERRAGL-0515R and MGAU program". The enrichment value is calculated from the ratio of intensities of the obtained hardware gamma spectra of ^{235}U and ^{238}U in the energy range of 89-100 keV using the program of multigroup analysis MGAU. The technique was validated for the relative error of measurements of 4 % at the confidence probability P = 0.95.

The powders were mixed in a rotating steel drum mixer. The homogeneity (quality) of the powder mixture was estimated by methods of mathematical statistics, by the so-called key-component – the ^{235}U content.

The non-uniformity coefficient in % (Fig. 6) determined from the ratio was used as the mixture uniformity criterion:

$$V_c = \frac{100}{\bar{c}} \sqrt{\frac{1}{n-1} \sum_{i=1}^{n} (c_i - \bar{c})^2} , \tag{1}$$

where c_i mass or volume fraction of the key-component in the *i*-sample; $\bar{c}$ - the average value of the mass or volume fraction of the key-component in the *i*-samples; *n* - the total count of samples taken from the mixture.

The homogeneity *M* was determined as (%):

$$M = 100 - V_c \tag{2}$$

The quality of the mixture is considered satisfactory at V_c = 6-8% (homogeneity *M*=92-94%), good at V_c= 4-6% (*M*=94-96%) and ideal at V_c<4% (*M*>96%).

The homogeneity of the obtained mixtures, located in a cube-shaped container with a side of 40 mm, was controlled in five different "source-detector" geometries. Four measurements were carried out with the detector against the side surface of the container with a mixture of uranium dioxide powders, each measurement differed from the previous one by rotating the container by 90°. The fifth measurement was carried out with the detector against the end surface of the container.

To control the homogeneity of the mixture, the heterogeneity factor was calculated by formula (1), where the values of the content of isotope ^{235}U obtained by processing five gamma-spectra with the MGAU software were used as and values.

In addition, another approach was used to control the homogeneity of the obtained mixtures. The results of the processing of five spectra for each mixture were subjected to statistical analysis: the mean values ($\bar{E}$) of the content of isotope ^{235}U, the standard deviation of $s(E_i)$ and the standard deviation of the mean $s(\bar{E})$:

$$\bar{E} = \frac{1}{n} \sum_{i=1}^{n} E_i , \tag{4}$$

$$s(E_i) = \left[\frac{1}{n-1} \sum_{i=1}^{n} \left(E_i - \bar{E} \right)^2 \right]^{1/2} , \tag{5}$$

$$s(\bar{E}) = \frac{s^2(E_i)}{n} , \tag{6}$$

where *n* is the number of measurements; E_i is the value of uranium isotope content obtained by processing the *i*-th spectrum.

Then we calculated the confidence interval for the confidence probability P = 0.95 using the relation:

$$\Delta = \sqrt{(s(\bar{E}) \times t)^2 + \delta^2} , \tag{7}$$

where *t* - is the Student coefficient for a given confidence probability and number of measurements, equal to 2.776, δ - statistical variance of the random variable of the MGAU program.

Control of trace impurities in fuel pellets was performed using the methodology №47:2018 from 28.06.2018 "Methodology for measuring the mass fraction of elements in uranium oxides, metallic uranium and its alloys by inductively coupled plasma mass spectrometry". Measurements are performed using an ELEMENT 2 type mass spectrometer. The technique covers measurement of mass concentration of such elements as uranium, chromium, iron, calcium, molybdenum, tungsten, silicon and vanadium.

The density of fuel pellets was determined by hydrostatic weighing in distilled water. The oxygen coefficient was determined by the calculation method based on weighing powders or UO_2 pellets before and after their calcination at 1000 ºC in a muffle furnace.

INFLUENCE OF TECHNOLOGICAL PARAMETERS FUEL PELLETS PRODUCTION ON THEIR CHARACTERISTICS

Many years of worldwide experience in nuclear fuel fabrication have developed the basic technological methods for producing uranium dioxide powders and fuel pellets using them, as well as methods for their control. Pressing and sintering of pellets are typical technological operations. A decisive role is also played by the preparation of powder materials before pressing, the type and amount of binder, and the method of mixing. Apart from the characteristics of powders themselves, the quality and characteristics of obtained fuel pellets depend on the design of used equipment and peculiarities of the technological process at all its stages.

Uranium dioxide powder with a nominal enrichment of 0.4 wt.% was used to develop the modes of pressing and sintering fuel pellets ^{235}U.

As a result of studies of the influence of the type of organic plasticizer (binder) in the form of polyethylene glycol and calcium stearate on the characteristics of pressed and sintered pellets, the optimal pressure, which provides the integrity and a necessary density of formed pellets was determined. Fuel pellets were formed at a pressure of 2.1-4.1 t/cm^2 (Fig. 3). Pressure exceeding 4 t/cm^3 negatively affects the quality of the pellets due to the appearance of cracks and delamination when pressing them out.

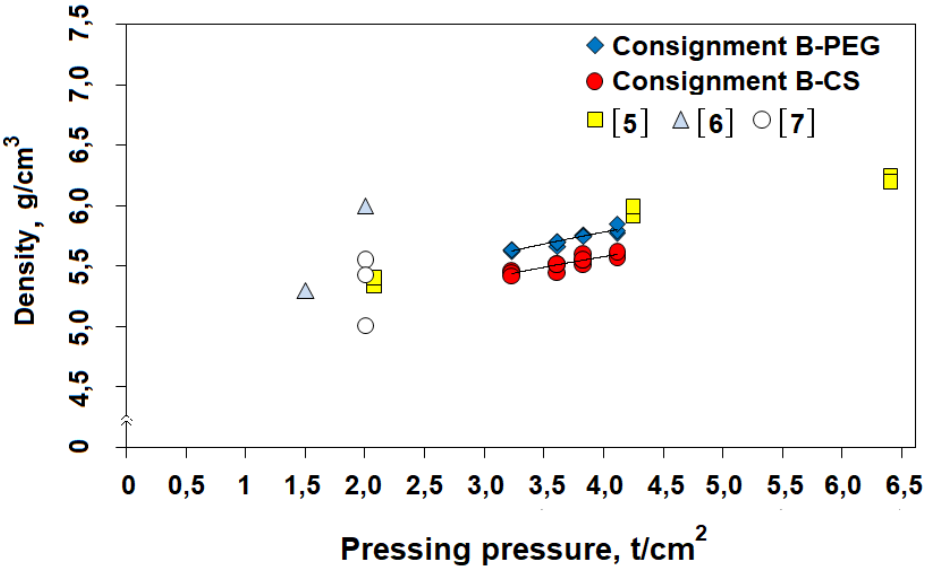

Figure 3. Dependence of the compressed (raw density) pellets on the pressing pressure and type of binder (in [5-7] literature data are given for comparison)

The optimal pressing pressure was 3 t/cm^2, at which two experimental batches of fuel pellets were subsequently pressed: V-CS (15 pcs.) and V-PEG (46 pcs.). The obtained data on the density of compressed tablets are in good agreement with other experimental data [5–8]. Sintered pellets were characterized by uniform shrinkage in height and diameter at the level of 20.2±0.6%, had no chips or cracks. Their appearance is satisfactory, which corresponds to the technical requirements of TR No. 12-1-081 [4] (Fig. 4).

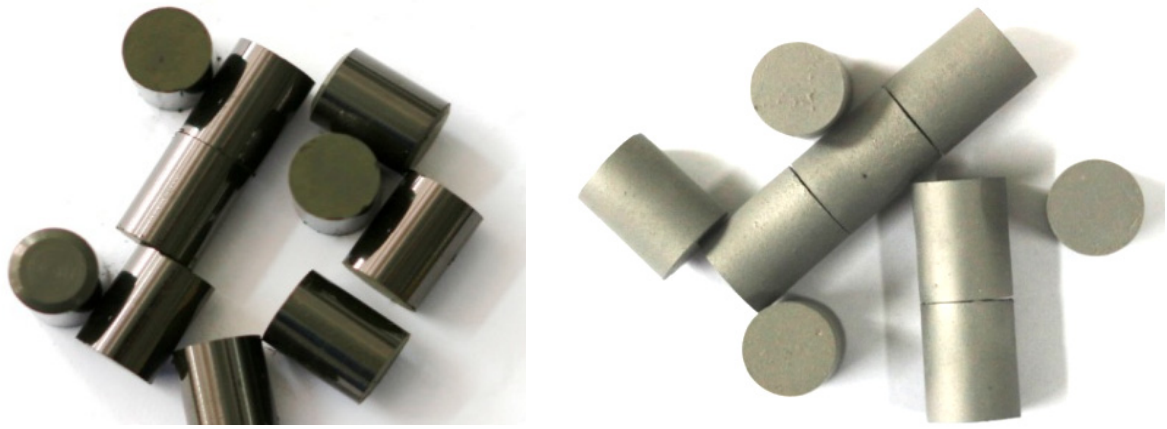

a b

Figure 4. Appearance of raw (a) and sintered (b) pellets

The results of measuring the geometric dimensions and density of fuel pellets are shown in Fig. 5.

Fuel pellets pressed on a dry binder - calcium stearate (B-CS batch), having an initial density of ~ 5.5 g/cm^3, after sintering have a density of 10.3-10.4 g/cm^3. Tablets pressed on a liquid binder - polyethyleneglycol (B-PEG batch), having an initial density of ~ 5.9 g/cm^3, after sintering have a density of 10.3-10.6 g/cm^3 (Fig. 5 b).

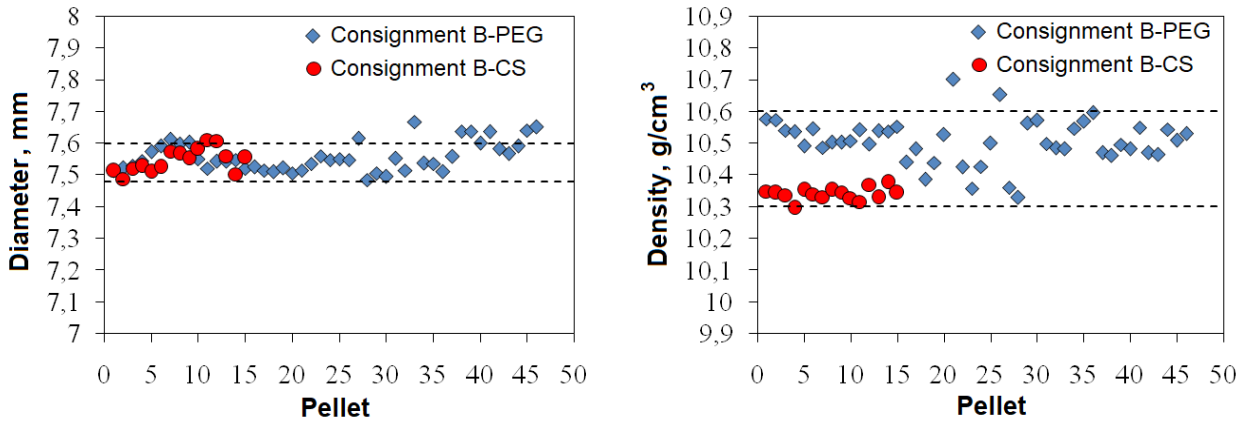

a b

Figure 5. Diameter (a) and density (b) of sintered pellets UO_2

It follows from the data obtained that a significant part of them meets the technical requirements for diameter (Ø7.54±0.06 mm) and density (10.45±0.15 g/cm^3). It follows from the conducted studies that in order to obtain the maximum density of fuel pellets, a liquid plasticizer, polyethyleneglycol, should be used as a binder. A study of the effect of isothermal holding time of 2 and 4 hours at 1700 ºC in vacuum did not reveal a significant increase in the density of sintered pellets. The average value of the density of tablets sintered at 1700 ºC for 4 hours for the B-PEG batch was 10.5 g/cm^3, and for the B-CS batch – 10.4 g/cm^3. The study of the microstructure of the pellets showed a uniform distribution of pores in their volume, the grain size was 2-7 μm, and the microhardness was 6-7 GPa.

Thus, the studies carried out made it possible to establish the optimal modes for obtaining fuel pellets, as well as to develop and manufacture molds in order to ensure the required tolerance for their diameter. The results of these studies made it possible to proceed to the manufacture of pilot batches of fuel pellets from a mixture of uranium powders with a given enrichment in ^{235}U according to the developed scheme. The results of measuring the ^{235}U content in the initial UO_2 powders were 19.905 ± 0.224 wt.%. and 0.454±0.044 wt.%.

Based on the obtained data, the mass of the initial powders was calculated to obtain a powder mixture with an enrichment of 4.4% wt. by ^{235}U. Figure 6 shows the results of monitoring the homogeneity of the mixtures obtained at different mixing times of the powders.

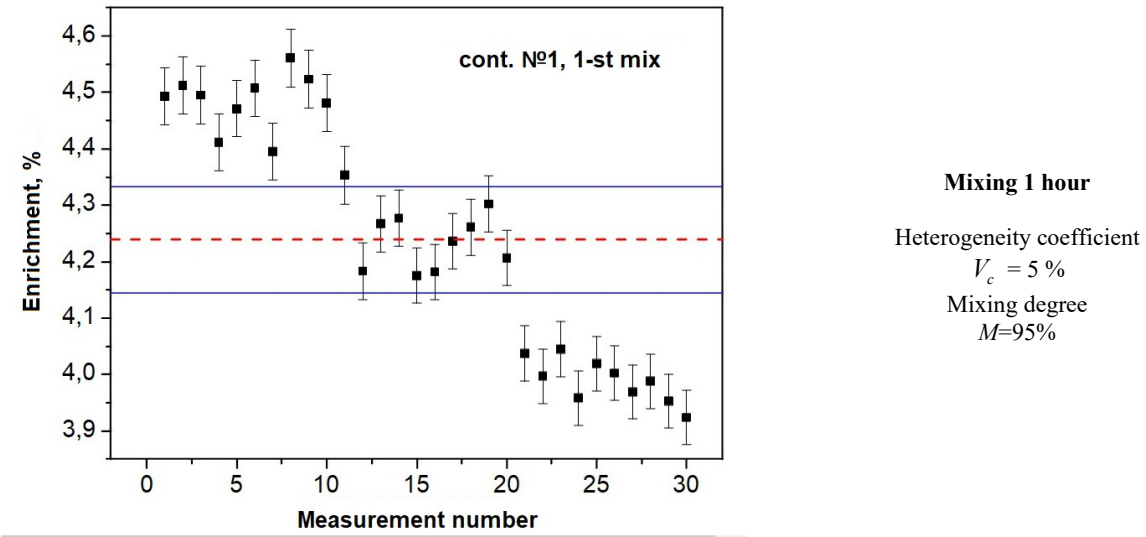

Figure 6. Dependence of the value of the coefficient of heterogeneity and the degree of mixing of UO_2 powders on time

(continued on next page)

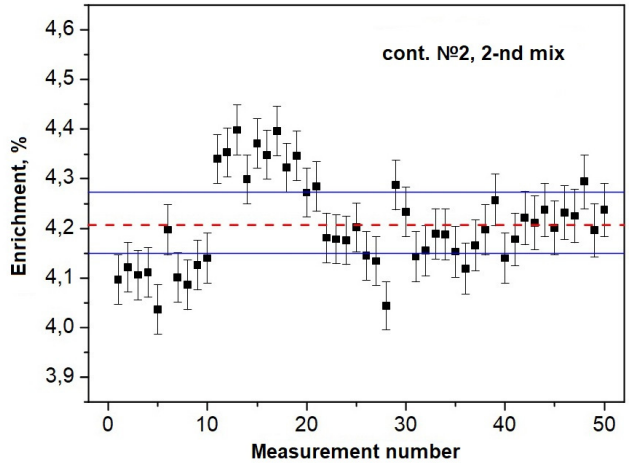

Mixing 3 hour

Heterogeneity coefficient
V_c = 2.14 %
Mixing degree
M=97.86%

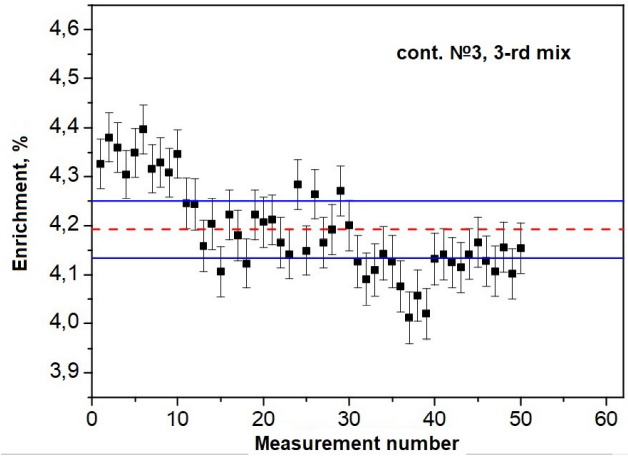

Mixing 8 hour

Heterogeneity coefficient
V_c = 2.24 %
Mixing degree
M=97.76%

Figure 6. Dependence of the value of the coefficient of heterogeneity and the degree of mixing of UO_2 powders on time

Thus, in this approach, the criterion for the homogeneity of the obtained mixtures of powders is the maintenance of the condition $\varepsilon \leq 4\ \%$ which will indicate that the possible inhomogeneity of the distribution of the ^{235}U isotope in the mixture is lower than the relative measurement error of the technique used.

Additional measurements of the enrichment of sintered fuel pellets located in the container amounted to 4.382±0.078% wt. by ^{235}U.

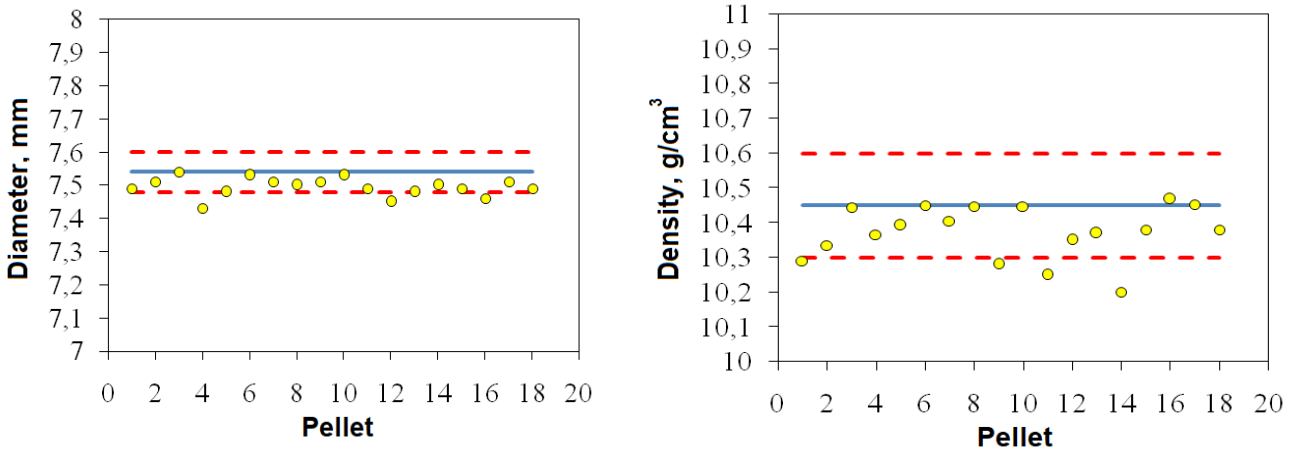

a b

Figure 7. Diameter (a) and density (b) of sintered fuel pellets UO_2

The pellets after sintering had a diameter of Ø7.48-7.60 mm (Fig. 7a) and a height of 8.6-10.7 mm. The density of sintered pellets was in the range of 10.4-10.6 g/cm^3 (Fig. 7b). The appearance of the pellets is satisfactory, there were no chips on the chamfers, and their microstructure is shown in Fig. 8.

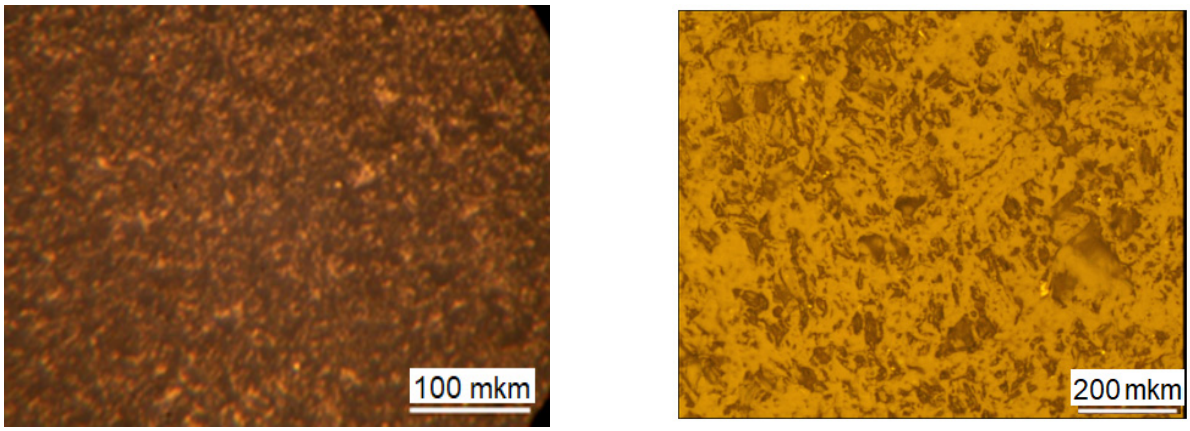

Figure 8. Microstructure of fuel pellets UO_2

The measured enrichment of fuel pellets was 4.395±0.058% weight ^{235}U (Table 1). The additionally measured average fuel enrichment of the experimental FA-X was 4.4±0.18 wt%. ^{235}U.

Table 1. Results of measurements a fuel pellets enrichment

№	Measured enrichment value, *X*	Instrumental measurement error, *d*	Statistical parameter	Value
1	4.392	0.049	Number of measurements, *n*	5.000
2	4.391	0.048	Mean, *Xcp*	4.395
3	4.415	0.048	Standard deviation, *S*	0.026
4	4.355	0.048	Standard deviation of the mean values, *Scp*	0.012
5	4.420	0.049	Student's coefficient for P=95%, *t*	2.776
6	4.392	0.049	Average instrumental error, *dcp*	0.048
			Confidence interval, *D*	0.058

At the measuring of impurities concentration in fuel pellets, it was found that the concentrations of such impurities as iron (Fe), chromium (Cr), molybdenum (Mo), tungsten (W) and others are quite low and do not exceed the limit values established by the ASTM standard [9], as well as the technical requirements of TR No. 12-1-081 [4] (Table 2). The limits of the relative error in measuring the mass contents of the analyzed elements do not exceed ± 20% at P = 0.95.

Table 2. Elemental composition of fuel pellets

Element	Element content, %wt.	
	Requirements № 12-1-081	Measurement
U	≥87.4	87.7
Cr	≤0.01	0.0086
Fe	≤0.03	0.0239
Na	≤0.01	0.0033
Mn	≤0.01	0.0065
Mo	≤0.01	0.0039
W	≤0.01	0.0047
Ca	≤0.015	0.0075
Si	≤0.01	0.0084
V	≤0.01	0.0006

CONCLUSION

Some characteristics of the subcritical assembly of the nuclear facility "Source of Neutrons" are given, as well as a description of the standard fuel assembly of the WWR-M2 type, used during the first fuel loading of the core, and the experimental FA-X, developed for subsequent loads.

A description of the technological scheme for the manufacture of fuel pellets with an enrichment of 4.4% by weight is presented on the ^{235}U isotope by mixing two powders with different uranium content: 0.4% wt. ^{235}U and 19.7% wt. ^{235}U.

The influence of technological regimes and parameters for the manufacture of fuel pellets from the obtained mixtures on their characteristics, such as enrichment, geometric dimensions, density, established in the design and technical documentation, has been studied.

On the basis of the conducted studies, the correctness of the choice of the technological scheme for the manufacture of fuel pellets and fuel rods of FA-X was shown.

ORCID IDs

Igor A. Chernov, https://orcid.org/0000-0003-1424-4471; **Anton V. Kushtym,** https://orcid.org/0000-0001-7058-373X
Dmytro V. Kutniy, https://orcid.org/0000-0001-9591-4013

REFERENCES

[1] N.I. Aizatskii, B.V. Borts, A.N. Vodin, P.A. Demchenko, A.Yu. Zelinskii, I.M. Karnaukhov, V.A. Kushnir, V.V. Mitrochenko, A.O. Mytsykov, I.M. Nekliudov, S.N. Oleinik, F.A. Peev, G.D. Pugachiov, S.A. Soldatov, I.V. Ushakov, I. Gohar, I. Bolshinskii, Ya.L. Chi, S.L. Pei, S.H. Wong, and V.B. Liu. PAST, **3**(79) (2012), https://vant.kipt.kharkov.ua/ARTICLE/VANT_2012_3/article_2012_3_3.pdf (in Russian)

[2] V.G. Aden, E.F. Kartashev, V.A. Lukitchev, P.I. Lavrenyuk, V.M. Tchernishov,A.V. Vatulin, A.V. Morozov, V.B. Suprun, A.B. Alexandrov, and A.A. Enin. PAST, **5**(88) (2005), https://vant.kipt.kharkov.ua/ARTICLE/VANT_2005_5/article_2005_5_3.pdf

[3] Draft specifications 12-1-044.00.00. *FA-X of a nuclear facility "Neutron source based on an accelerator-controlled subcritical assembly"*, «Nuclear Fuel Cycle» Science and Technology Establishment National Science Center «Kharkiv Institute of Physics and Technology», 2022.

[4] Technical requirements No. 12-1-081. *Fuel tablets from uranium dioxide*. «Nuclear Fuel Cycle» Science and Technology Establishment National Science Center «Kharkiv Institute of Physics and Technology», 2013.

[5] A.V. Kuleshov et al, Patent Russian Federation No. 2376663, (10.08.2010). (in Russian), https://patentimages.storage.googleapis.com/ea/b1/19/b700b304237012/RU2376665C2.pdf

[6] A.V. Kucherenko et al, Patent Russian Federation No. 2317601, (20.02.2008). (in Russian), https://patentimages.storage.googleapis.com/9c/56/4a/81d326afa6ef86/RU2317601C1.pdf)

[7] I.I. Loktev, A.B. Alexandrov et al. Proceedings of the Tomsk Polytechnic Institute. **7,** (307), (2004), https://doc365.ru/uploads/store/5fc416b5b45e60.45419985_hkgfmepliqnoj.pdf

[8] Yu. A. Stetsky et al, Patent Russian Federation No. 2182378, (20.12.2009). (in Russian)

[9] ASTM C776-00. *Standard Specification for Sintered Uranium Dioxide Pellets*, https://www.astm.org/c0776-00.html

ОСОБЛИВОСТІ ВИГОТОВЛЕННЯ І ХАРАКТЕРИСТИКИ ПАЛИВНИХ ТАБЛЕТОК ІЗ ДІОКСИДУ УРАНУ ДЛЯ СТРИЖНЕВИХ ТВЕЛІВ ПІДКРИТИЧНОЇ ЗБІРКИ

І.О. Чернов[a], А.В. Куштим[a], В.Р. Татарінов[a], Д.В. Кутній[b]

[a]Науково-технічний комплекс «Ядерний паливний цикл»
[b]Науково-технічна служба ядерних матеріалів і експортного контролю
Національного наукового центру «Харківський фізико-технічний інститут»
вул. Академічна, 1, м. Харків, 61108, Україна

Досліджено вплив технологічних режимів виготовлення паливних таблеток із діоксиду урану для твелів розроблюваної дослідної тепловидільної збірки ТВЗ-Х, призначеної в якості альтернативного палива для дослідницької ядерної установки (ДЯУ) «Джерело нейтронів, яке керується прискорювачем електронів». На відміну від стандартних технологічних процесів виготовлення таблеток UO_2, особливістю виготовлення даного типу ядерного палива, є одержання порошку діоксиду урану зі збагаченням 4.4% ваг. по ^{235}U шляхом змішування двох партій порошків з різним вмістом урану: 0.4% ваг. ^{235}U і 19.7% ваг. ^{235}U, а також забезпечення необхідного допуску паливних таблеток без застосування операцій механічної обробки. У НТК ЯПЦ ННЦ ХФТІ розроблено комплект конструкторської та технологічної документації, виготовлені експериментальні зразки паливних таблеток, твелів та дослідної тепловидільної збірки ТВЗ-Х, яка спроектована сумісною та взаємозамінною з ТВЗ ВВР-М2, яка прийнята в якості штатного при першому паливному завантаженні в ДЯУ «Джерело нейтронів, яке керується прискорювачем електронів». На відміну від варіанту ТВЗ типу ВВР-М2, що складається з трьох твелів трубчастої форми з дисперсійною паливною композицією UO_2-Al, в ТВЗ-Х розміщені шість твелів стрижневого типу з таблетковим паливом UO_2 в оболонці з цирконієвого сплаву Е110, як найближчого аналога твела енергетичного реактора ВВЕР-1000. Всередині оболонки розташований стовп паливних таблеток висотою 500 мм, який зафіксований від переміщення розпірною втулкою. В основному варіанті ТВЗ-Х паливні таблетки виготовлені з UO_2 зі збагаченням по ^{235}U 4.4% ваг.

Ключові слова: тепловидільний елемент, тепловидільна збірка, порошок, діоксид урану, збагачення, однорідність суміші, щільність, мікроструктура.

EAST EUROPEAN JOURNAL OF PHYSICS. **3.** 67-76 (2022)
DOI:10.26565/2312-4334-2022-3-09 ISSN 2312-4334

ENHANCED PERFORMANCE OF $CuIn_{1-x}G_xSe_2$ SOLAR CELL THROUGH OPTIMIZATION OF ABSORBER AND BUFFER LAYER PROPERTIES USING SCAPS-1D†

Godwin J. Ibeh[a], Celine O. Lawani[a], Jayeola O. Emmanuel[b], Peter O. Oyedare[c], Eli Danladi[d]*, Olumide O. Ige[a]

[a]*Department of Physics, Nigerian Defence Academy, Kaduna, Nigeria*
[b]*Department of Basic Science and General Studies, Federal College of Forestry Mechanization, Kaduna, Nigeria*
[c]*Department of Science Laboratory Technology, Federal Polytechnic Ede, Osun State, Nigeria*
[d]*Department of Physics, Federal University of Health Sciences, Otukpo, Benue State, Nigeria*
**Corresponding Author: Email: danladielibako@gmail.com, tel.: +2348063307256*
Received July 29, 2022; revised August 17, 2022; accepted August 21, 2022

This study is a follow up to our previously published article on "Numerical Simulation of Copper Indium Gallium Diselenide Solar Cells Using One Dimensional SCAPS Software". Five more parameters were optimized which are: absorber band gap, absorber electron affinity, buffer layer band gap, buffer layer electron affinity and working temperature using the same simulation tool initially used. When the absorber bandgap was varied between 0.8 eV and 1.6 eV, the efficiency of the solar cell increases until it reached its peak at 27.81%. This occurred at absorber bandgap of 1.4 eV. Other photovoltaic parameters at this optimum value are: V_{oc} of 1.00 V, J_{sc} of 31.99 mA/cm^2 and FF of 87.47 %. On varying the absorber electron affinity from 4.20 eV through 4.55 eV, we obtained an optimum value of 4.45 eV at V_{oc} of 0.82 V, J_{sc} of 37.96 mA/cm^2, FF of 84.99 % and an efficiency of 26.36%. The optimization of buffer bandgap resulted in an optimal value of 3.0 eV, when the buffer bandgap was varied between 1.6 eV and 3.2 eV. The photovoltaic parameters at this optimal value are: V_{oc} of 0.80 V, J_{sc} of 37.96 mA/cm^2, FF of 85.22 % and an efficiency of 25.86%. The effect of buffer electron affinity was studied by varying its value between 4.00 eV and 4.40 eV and its best value was found to be 4.05 eV at photovoltaic parameters with a V_{oc} of 0.82 V, J_{sc} of 37.96 mA/cm^2, FF of 84.98 % and an efficiency of 26.36 %. These optimized values in all parameters were used to simulate a solar cell which resulted to device with performances: V_{oc} of 1.11 V, J_{sc} of 31.50 mA/cm^2, FF of 88.91 % and an efficiency of 31.11 %. On varying the working temperature on the optimized solar cell, the optimized device with its best performance at 270 K with Photovoltaic (PV) values of V_{oc} of 1.15 V, J_{sc} of 31.55 mA/cm^2, FF of 88.64 % and an efficiency of 32.18%. The results obtained were encouraging and can serve as a guide to those involved in practical development of solar cells.
Keywords: SCAPS, Buffer Layer, Solar cells, photovoltaic
PACS: 61.43.Bn; *68.55.ag*; *68.55.jd*; 73.25.+i; 72.80.Tm; 41.20.Cv

1. INTRODUCTION

The process of getting energy from sources like fossil fuels which has been a major source of power for most countries of the world, has been found to pose a wide range of dangers (causing health concerns, ozone layer depletion, enhanced greenhouse effect, etc.) to human existence. Considering the very important role of electrical energy in the technological advancement of the society, its demand is far greater than ever in developed and developing countries. Nations without natural deposits of oil and gas are likely to find it very difficult in the nearest future to get supplies of these products since they are expensive, fast diminishing and politically regulated [1]. A good alternative to oil and gas sources for the production of electrical energy would have been found in nuclear energy sources such as uranium and plutonium but accidents in nuclear power plants and disposal of nuclear waste are a great challenge.

The search for a renewable and clean source of energy for industrial, technological and domestic purposes has led to the ongoing efforts at exploiting energy from the sun which is known alternatively as solar energy. Over the years, researchers have been finding the most efficient ways to harness solar energy and this has led to the development of the solar cell. In order to be able to understand the operation of solar cells, numerical modeling has been used in a number of instances and it has proven to be a very important tool in this regard [2,3].

As a follow up to our previously published article [3], we made use of SCAPS to optimize additional five parameters which include: absorber band gap, absorber electron affinity, buffer layer band gap, buffer layer electron affinity and working temperature.

2. DEVICE MODELLING AND SIMULATION

In line with the initial device set up demonstrated in our previous work [3], we utilized a solar capacitance simulation software based on the poisson and continuity equation to achieve the desired objective. The details of the set-up and simulation can be obtained in Lawani et al. [3]. In this study, similarly, a defect from double acceptor with a gaussian energy distribution, value of concentration of 1.0E + 14 cm^{-3} defect, and level of energy of 0.1, 0.4, eV slightly above valence band, were introduced into the CIGS (absorber) layer. The defect can be seen to arise as a result of Cu_{III} defect

† ***Cite as***: G.J. Ibeh, C.O. Lawani, J.O. Emmanuel, P.O. Oyedare, E. Danladi, and O.O. Ige, East Eur. J. Phys. **3**, 67 (2022), https://doi.org/10.26565/2312-4334-2022-3-09

which is most times noticed in CIGS absorbers [4]. The absorber band gap was varied from 0.8 – 1.6 eV, absorber electron affinity was varied from 4.20 – 4.55 eV, buffer layer band gap was varied from 1.6 – 3.2 eV, buffer layer electron affinity was varied from 4.00 – 4.40 eV. The simulated device structure is as shown in Fig 1. All other parameters were kept constant while varying the aforementioned parameters.

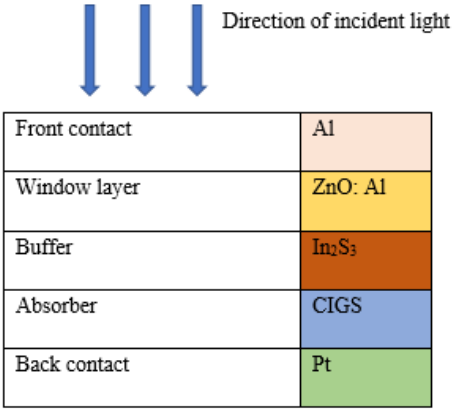

Figure 1. Model of the simulated solar cell [3]

3. RESULTS AND DISCUSSION

3.1. Effect of varying CIGS (absorber) bandgap

The effect of absorber band gap was investigated by varying the CIGS layer band gap from 0.8 eV through 1.6 eV. Figure 2 shows the variation of CIGS solar cells' photovoltaic parameters with increasing absorber layer bandgap.

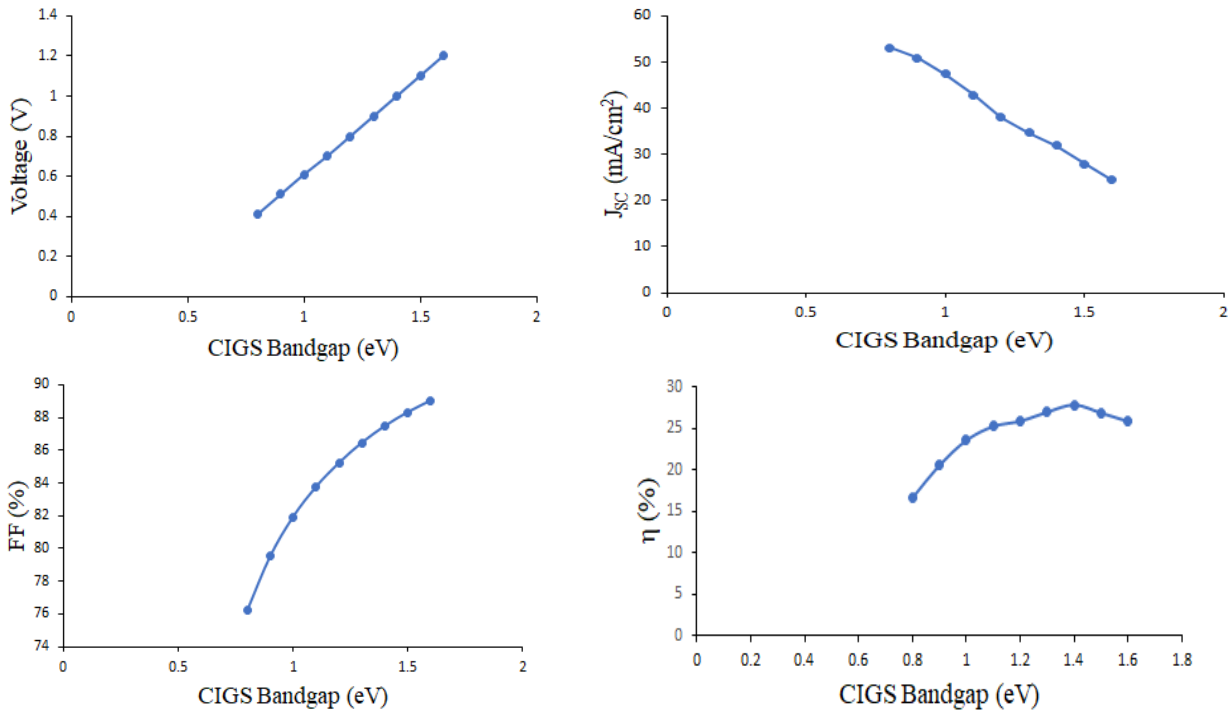

Figure 2. Variation of Voc, Jsc, FF and η with increasing CIGS bandgap

It was observed that J_{SC} decreased with increasing bandgap energy. This decrease occurs because part of the solar spectrum was not harvested by the solar cells [5]. An absorber with high bandgap energy absorbs photons with low wavelengths to release electrons from the valence band to conduction band in accordance with Einstein's equation [6,7] given in equation 1 below:

$$E_g = \frac{hc}{\lambda_g}, \tag{1}$$

where h is Plank's constant, c is the velocity of light and λ_g are wavelength which matches the band gap of the absorber. V_{OC} is seen to increase with increasing bandgap of the absorber.

According to Scheer and Schock [8], decreasing the bandgap of the absorber increases photocurrent but causes a decrease in V_{OC}. This is clear when the relationship between V_{OC} and bandgap in equation 2 is considered.

$$V_{OC} = \frac{E_a}{q} + \frac{AKT}{q} \ln\left(-\frac{J_{SC}\,\eta(V_{OC})}{J_{00}}\right) \tag{2}$$

where A is the solar cells' quality factor, q is the elementary charge, E_a is the activation energy of J_O (and is approximately equal to the absorber bandgap [8]), J_O is saturation current density and J_{00} is the reference current density of the solar cell.

The observed increase in efficiency is due to the increase in V_{OC} and fill factor [9], but as the J_{SC} drops with increasing bandgap of absorber, the efficiency begins to fall since light absorption reduces. This is detrimental to the solar cells as their performance goes down. Table 1 gives the dependence of the solar cells' performance on CIGS layer bandgap. It shows that the highest efficiency achieved after variation of CIGS absorber band gap is 27.81 % and this occurred at a bandgap of 1.4 eV. Other photovoltaic parameters at this optimized value of band gap are: V_{OC} of 1.0 V, J_{SC} of 31.99 mA/cm^2 and FF of 87.47 %.

Table 1. Dependence of solar cells' performance on absorber layer bandgap

CIGS bandgap (eV)	V_{OC}(V)	J_{SC}(mA/cm^2)	FF (%)	η (%)
0.8	0.41	53.13	76.20	16.55
0.9	0.51	50.83	79.51	20.50
1.0	0.61	47.43	81.92	23.52
1.1	0.70	42.86	83.76	25.22
1.2	0.80	37.96	85.22	25.85
1.3	0.90	34.76	86.45	26.94
1.4	1.00	31.99	87.47	27.81
1.5	1.10	27.86	88.31	26.82
1.6	1.20	24.45	89.02	25.82

The J-V curves in Figure 3(a) show that as bandgap of the absorber increases, the Jsc of the solar cells decreases but the open circuit voltage increases. Figure 3(b) depicts the QE as a function of wavelength for corresponding CIGS layer bandgap. For device with wavelength within the range 300 nm – 1600 nm the absorption efficiency remains the same.

The arrangement of the curves (curves corresponding to lower bandgaps are outermost, while those curves corresponding to higher bandgaps are innermost) show the inverse relationship existing between the various bandgaps and their corresponding wavelengths, as given in Equation 1.

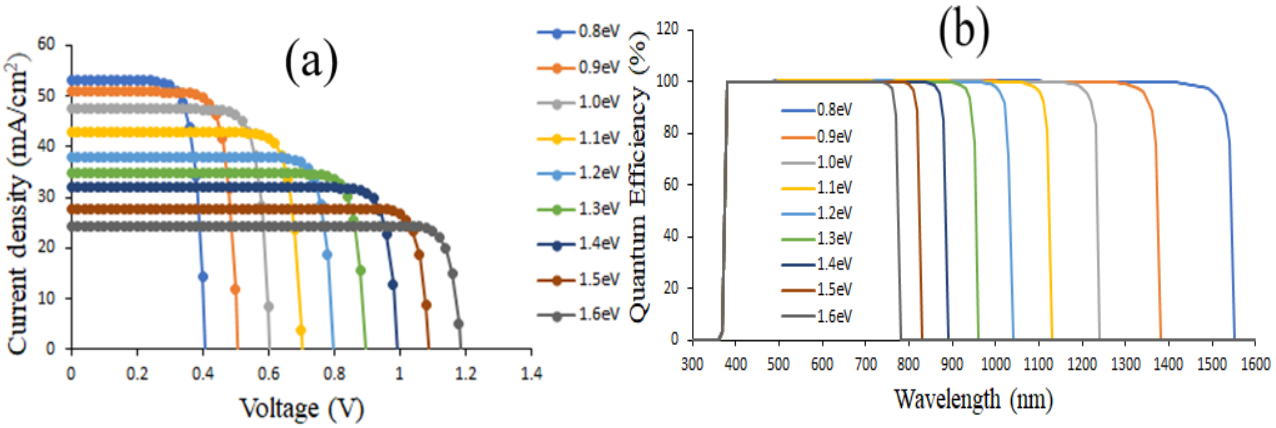

Figure 3. (a) J-V curves and (b) QE of CIGS solar cell with various values of absorber layer bandgap

3.2. Effect of varying electron affinity of CIGS (absorber) layer

Table 2 shows the dependence of solar cells' performance on electron affinity. In the case where the electron affinity of the n-type layer is smaller than that of the p-type layer, a positive conduction band offset (also known as a spike) given in equation 3 is formed otherwise a cliff is formed [10]

$$\Delta E_C = E_{C,n} - E_{C,P} > 0, \tag{3}$$

where $E_{C,n}$ is conduction band energy for n-type layer and $E_{C,P}$ is conduction band energy for p-type layer.

From Table 2, V_{OC} increases until it saturates at a bandgap of 4.35 eV (Figure 4). The increase in V_{OC} is very likely caused by a spike which reduces the occurrence of recombination (This is good for the solar cells as recombination degrades their performance.). This also explains the rise in efficiency of the CIGS solar cells as electron affinity of absorber increases. J_{SC} remains constant but fill factor rises to its optimum value and begins to fall due to the formation

of high spikes [11]. The optimum value of electron affinity for the absorber was found to be 4.45 eV and the metric parameters are: V_{OC} of 0.82 V, J_{SC} of 37.96 mA/cm^2, FF of 84.99 % and a PCE of 26.36 %.

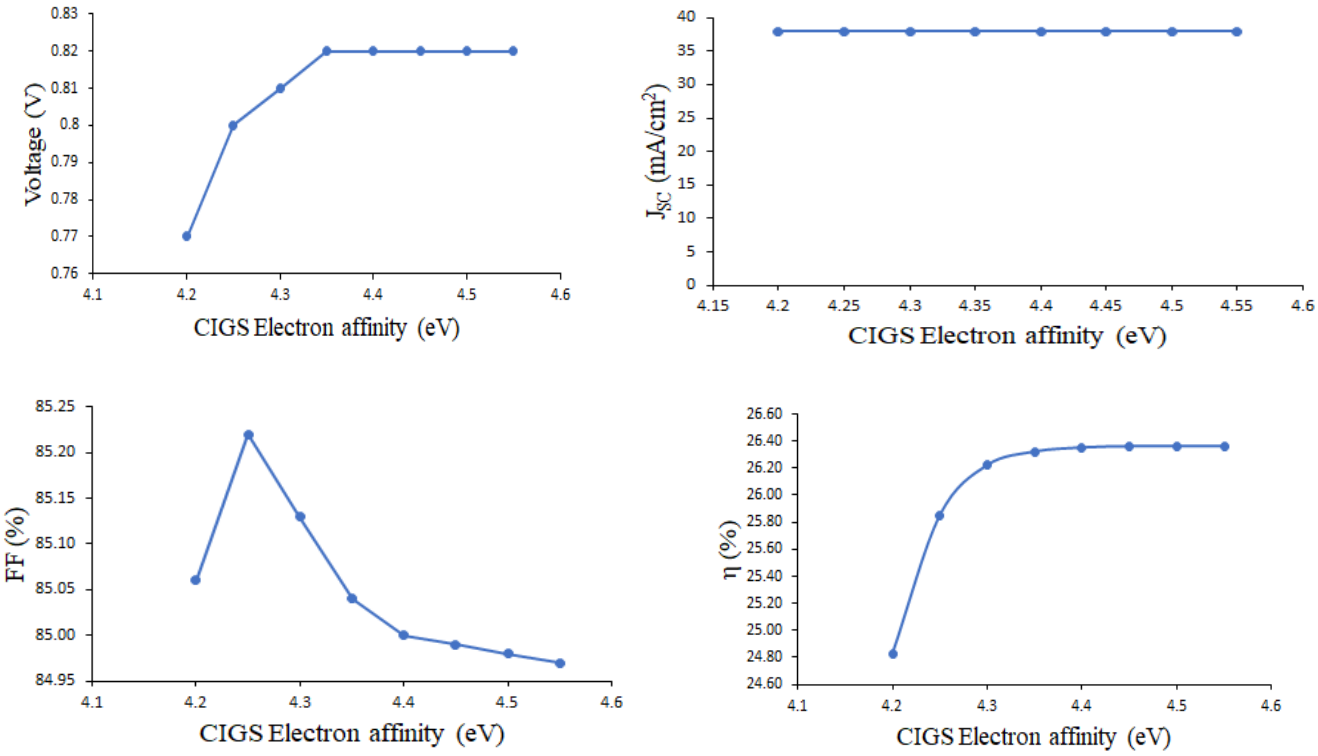

Figure 4. Variation of Voc, Jsc, FF and η with increasing CIGS Electron Affinity

Table 2. Dependence of solar cells' performance on electron affinity of absorber layer

CIGS electron affinity (eV)	Voc (V)	Jsc (mA/cm^2)	FF (%)	η (%)
4.20	0.77	37.96	85.06	24.83
4.25	0.80	37.96	85.22	25.85
4.30	0.81	37.96	85.13	26.22
4.35	0.82	37.96	85.04	26.32
4.40	0.82	37.96	85.00	26.35
4.45	0.82	37.96	84.99	26.36
4.50	0.82	37.96	84.98	26.36
4.55	0.82	37.96	84.97	26.36

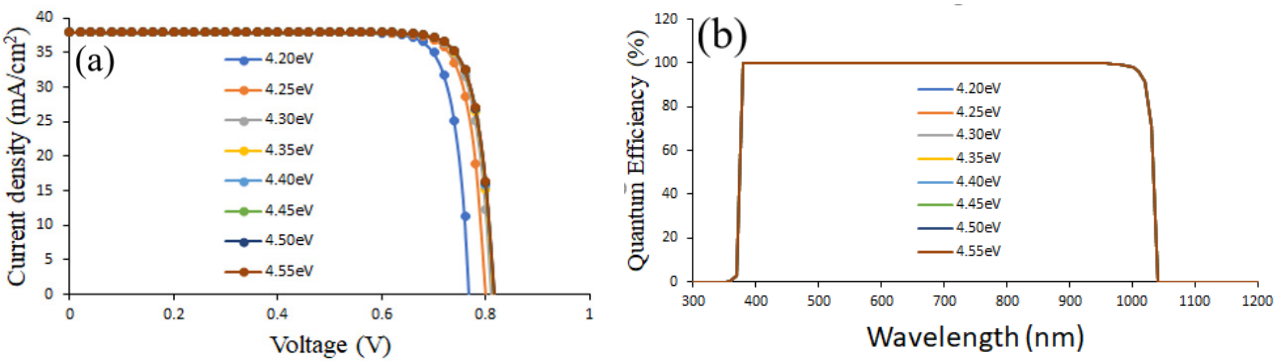

Figure 5. (a) J-V curves and (b) QE of CIGS solar cell with various values absorber (CIGS) electron affinity

The J-V curves in Fig. 5(a) show that for all values of electron affinity of absorber, J_{SC} remains the same while V_{OC} increased until it attained its optimum value and remained constant (this is shown in areas where the curves overlap). Figure 5(b) is the representation of QE as a function of wavelength for the selected values of CIGS electron affinity.

As demonstrated, within the wavelength range of 300 nm – 1200 nm, an overlap in the QE curves was observed which is attributed to the unchanged absorption efficiency within the selected values of the CIGS electron affinity. This

spectral response proves that absorber (CIGS) electron affinity has only a slight effect on the metric parameter of CIGS solar cells investigated.

3.3. Effect of varying In_2S_3 (buffer) bandgap

Figure 6 shows the variation of photovoltaic parameters with buffer layer bandgap. The buffer bandgap was varied from 1.6 eV through 3.2 eV.

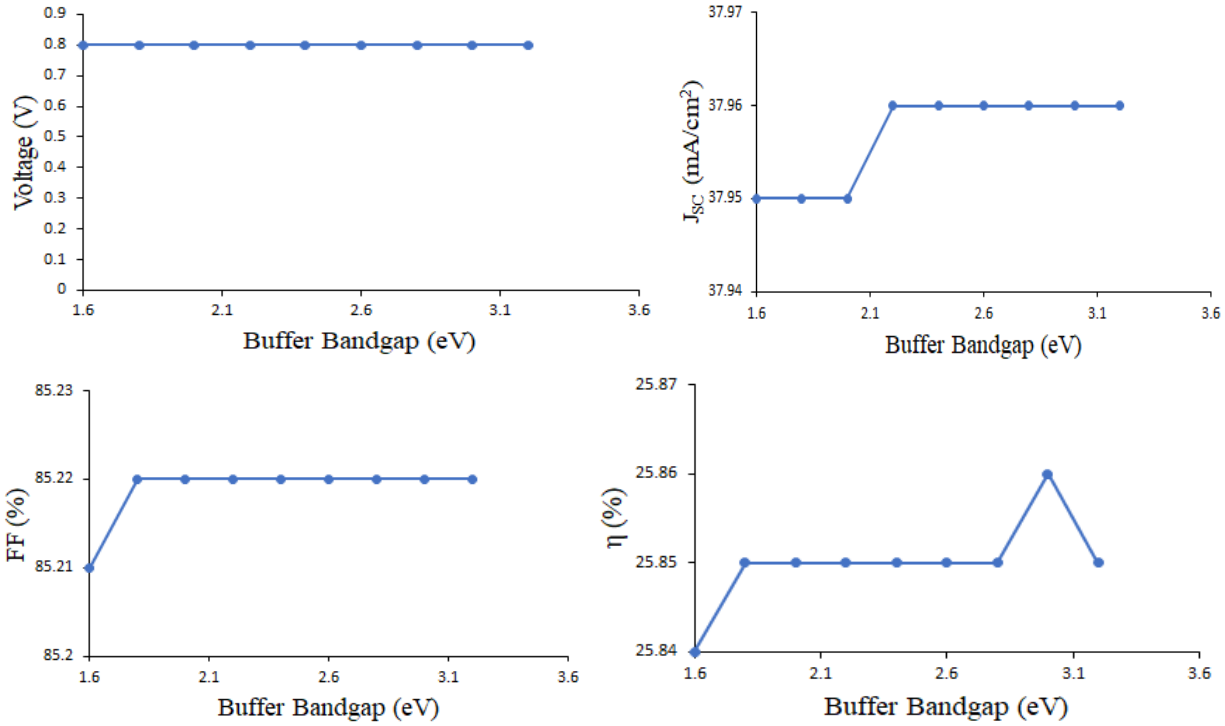

Figure 6. Variation of Voc, Jsc, FF and η with increasing CIGS Electron Affinity

It was discovered that while V_{OC} was unaffected by this variation, J_{SC} and FF rose to their peaks and remained constant thereafter. The efficiency also rose to its optimum value and then dropped. Although J_{SC} remained constant for higher values of buffer bandgap, it increased initially with an increase in buffer layer bandgap because more photons were allowed to reach the absorber layer and create more electron-hole pairs [12]. This translates to an increase in efficiency and fill factor but efficiency eventually drops beyond buffer bandgap of 3.0 eV because as bandgap goes higher, photons cannot achieve the needed amount of energy to create enough electron-hole pairs [13] which is needed to increase efficiency. The performance of the solar cells then drops. The best value of buffer bandgap after optimization is 3.0 eV and this occurs at V_{OC} of 0.80 V, J_{SC} of 37.96 mA/cm^2. FF of 85.22 % and efficiency of 25.86 % (see Table 3).

Table 3. Dependence of solar cells' performance on buffer layer bandgap

Buffer bandgap(eV)	Voc (V)	Jsc (mA/cm2)	FF (%)	η (%)
1.6	0.80	37.95	85.21	25.84
1.8	0.80	37.95	85.22	25.85
2.0	0.80	37.95	85.22	25.85
2.2	0.80	37.96	85.22	25.85
2.4	0.80	37.96	85.22	25.85
2.6	0.80	37.96	85.22	25.85
2.8	0.80	37.96	85.22	25.85
3.0	0.80	37.96	85.22	25.86
3.2	0.80	37.96	85.22	25.85

Figure 7(a) shows the curves for short circuit current density against the open circuit voltage for the different values of buffer bandgap used in this study. It reveals overlapping curves and these overlaps are more prominent as the curves drop to meet the voltage axis. This means that while J_{SC} experiences slight variations, V_{OC} remains constant for all values of buffer layer band gap.

Figure 7(b) is a representation of the QE versus wavelength for the selected values of buffer (In_2S_3) layer bandgap. Selecting the range of wavelength to be 300 nm – 1200 nm, results to spectral overlap. We therefore speculate that In_2S_3 layer bandgap has negligible or no effect on the performance of CIGS solar cells studied.

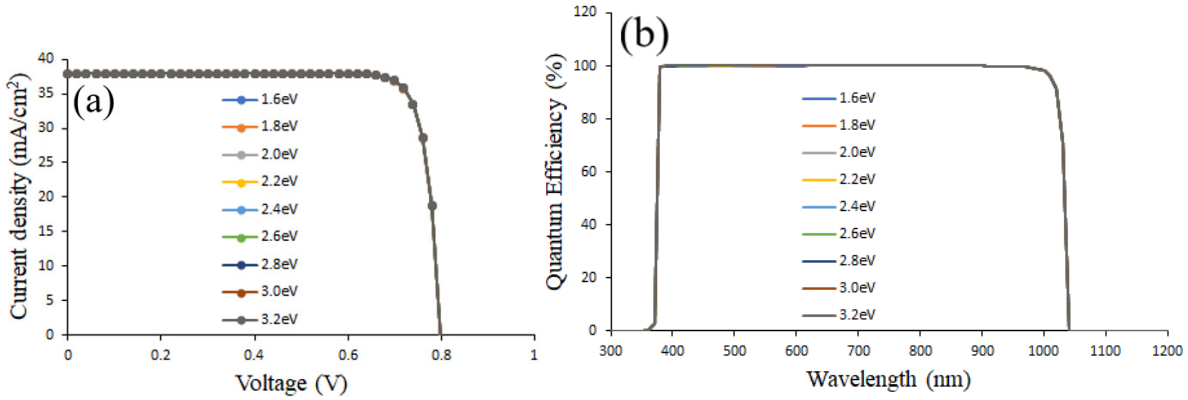

Figure 7. (a) J-V curves and (b) QE of CIGS solar cell with different values of buffer (In_2S_3) layer bandgap.

3.4 Effect of varying electron affinity of In_2S_3(buffer) layer

Figure 8 shows the variation of photovoltaic parameters with an increase in the electron affinity of the buffer layer. J_{SC} is observed to be constant until it experiences a slight increase beyond an electron affinity of 4.4 eV.

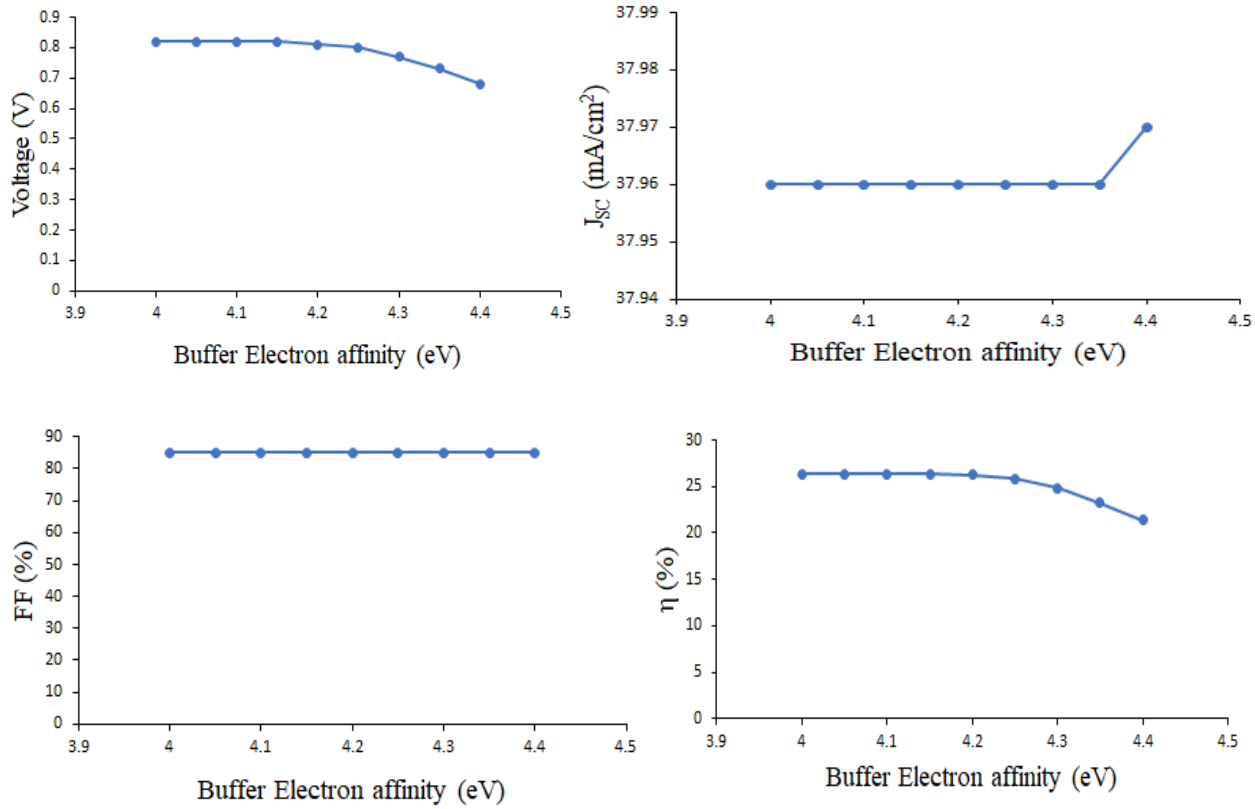

Figure 8. Variation of Voc, Jsc, FF and η with increasing electron affinity of buffer layer

This is due to the formation of cliffs which pose no barrier to photogenerated electrons. This would have been good for the solar cells' performance but as a cliff helps to boost Jsc it causes recombination between electrons injected from buffer layer and the interface defects [11]. We therefore see that V_{OC}, and efficiency, begin to decrease while fill factor remains unchanged. After optimization, the best value of buffer electron affinity is seen to be 4.05 eV at V_{OC} of 0.82 V, J_{SC} of 37.96mA/cm^2, FF of 84.98 % and efficiency of 26.36 % as shown in Table 4.

The J-V curves (Figure 9(a)) show that between buffer electron affinities of 4.00 eV and 4.15 eV, the open circuit voltage is the same but it varies thereafter, with the curve for the highest electron affinity appearing innermost (this indicates that the open circuit voltage is least for the highest electron affinity). The short circuit current density shows little or no change.

Figure 9(b) depict the QE versus wavelength of electron affinity values selected for buffer layer (In_2S_3). Choosing within a range of 4.00 eV and 4.15 eV, there is a clear overlap in the QE curves.

Table 4. Dependence of solar cells' performance on electron affinity of buffer layer

In_2S_3 electron affinity (eV)	Voc(V)	Jsc(mA/cm2)	FF(%)	η (%)
4.00	0.82	37.96	84.98	26.36
4.05	0.82	37.96	84.98	26.36
4.10	0.82	37.96	84.98	26.35
4.15	0.82	37.96	84.98	26.32
4.20	0.81	37.96	84.98	26.22
4.25	0.80	37.96	84.98	25.85
4.30	0.77	37.96	84.98	24.83
4.35	0.73	37.96	84.98	23.24
4.40	0.68	37.97	84.98	21.40

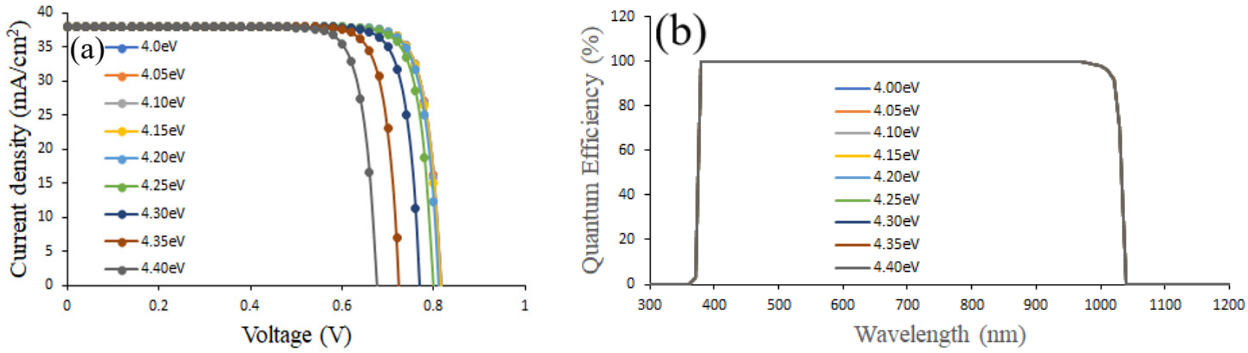

Figure 9. (a) J-V curves and (b) QE of CIGS solar cell different values of buffer (In_2S_3) layer electron affinity

3.5 Performance of optimized parameters

In accordance to the optimized parameters obtained in this research and those sourced from our previous work [3] (see Table 5), an efficiency of 31.13 %, current density of 31.55 mA/cm^3, voltage of 1.11 V and fill factor of 88.91 % were obtained (see Figure 10 and Table 6). These photovoltaic parameters obtained from optimization agree very much with those of the theoretical limits quoted by Ruhle [14]. Compared with the experimental data obtained in literature [15], which shows a PCE value of 22.6 %, the optimized device in this work demonstrates an enhanced value of ~37.74 % in PCE over the reported [15].

Table 5. Optimized parameters of the device

Optimized parameters	Absorber	Buffer
Multivalent defect density(cm^{-3})	1E + 10 [3]	----
Thickness (μm)	1.20 [3]	0.01[3]
Bandgap(eV)	1.40	3.00
Electron affinity (eV)	4.45	4.05

Table 6. photovoltaic parameters corresponding to optimized parameters of the CIGS solar cells compared with those of experimental researches and the maximum theoretical limit for solar cells with absorber bandgap of 1.4 eV

Simulation	V_{OC} (V)	J_{SC} (mA/cm^2)	FF (%)	η (%)
Initial	0.79	37.96	85.22	25.85
Optimized multivalent defect density (cm^{-3})	0.82	37.96	86.04	26.81
Optimized absorber thickness (***μ***m)	0.81	37.75	85.27	25.94
Optimized absorber bandgap(eV)	1.00	31.99	87.47	27.81
Optimized electron affinity of absorber (eV)	0.82	37.96	84.99	26.36
Optimized buffer thickness (***μ***m)	0.80	37.96	85.23	25.98
Optimized buffer bandgap (eV)	0.80	37.96	85.22	25.86
Optimized electron affinity of buffer (eV)	0.82	37.96	84.98	26.36
Final optimization	1.11	31.55	88.91	31.13
Maximum theoretical (Shockley-Queisser) limit	1.12	32.88	89.30	32.91 [14]
Experimental data	0.76	34.80	79.10	20.80 [16]
Experimental data	0.74	36.70	80.50	22.00 [17]
Experimental data	0.74	37.80	80.60	22.60 [15]

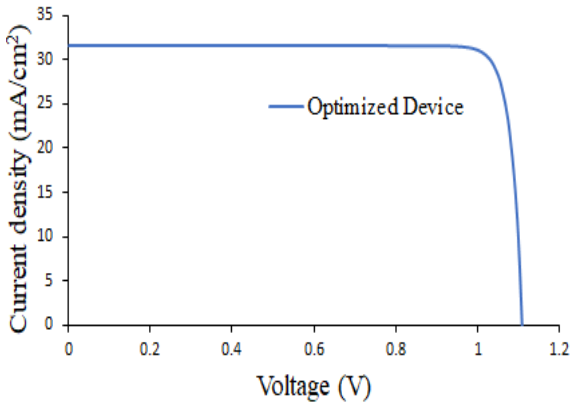

Figure 10. J-V curve of CIGS solar cell with optimized parameters

3.6 Effect of working temperature on the optimized device

Solar panels are usually installed in an open environment [18] and so the temperature under which they operate could affect their performance. When sunlight falls on solar cells, their temperatures rise. In this research the working temperature of the optimized cell was varied from 260 K through 340 K. Table 7 shows the dependence of solar cells performance on working temperature while Figure 11 gives the variation of photovoltaic parameters with increasing temperature. J_{SC} remains constant (Figure 11(b)) but V_{OC} keeps decreasing because of an increase in reverse saturation current with temperature. The fill factor reaches its peak at a temperature of 280 K and then begins to drop. This fall is due to light induced degradation [19]. The efficiency attains its optimum value at 270 K and also drops because when operating temperatures get higher than this optimum value, the electrons in the solar cell gain energy but instead of boosting electricity generation, they become unstable and recombine before they are collected [20]. Figure 12 shows the J-V curves of the CIGS solar cells with increasing temperature.

Table 7. Dependence of optimized solar cells' performance on temperature

Temperature (K)	V_{OC} (V)	J_{SC} (mA/cm^3)	FF (%)	η (%)
260	1.16	31.55	84.14	30.90
270	1.15	31.55	88.64	32.18
280	1.14	31.55	89.14	31.98
290	1.12	31.55	89.11	31.59
300	1.11	31.55	88.91	31.13
310	1.10	31.55	88.60	30.64
320	1.08	31.55	88.25	30.14
330	1.07	31.55	87.90	29.64
340	1.05	31.55	87.52	29.12

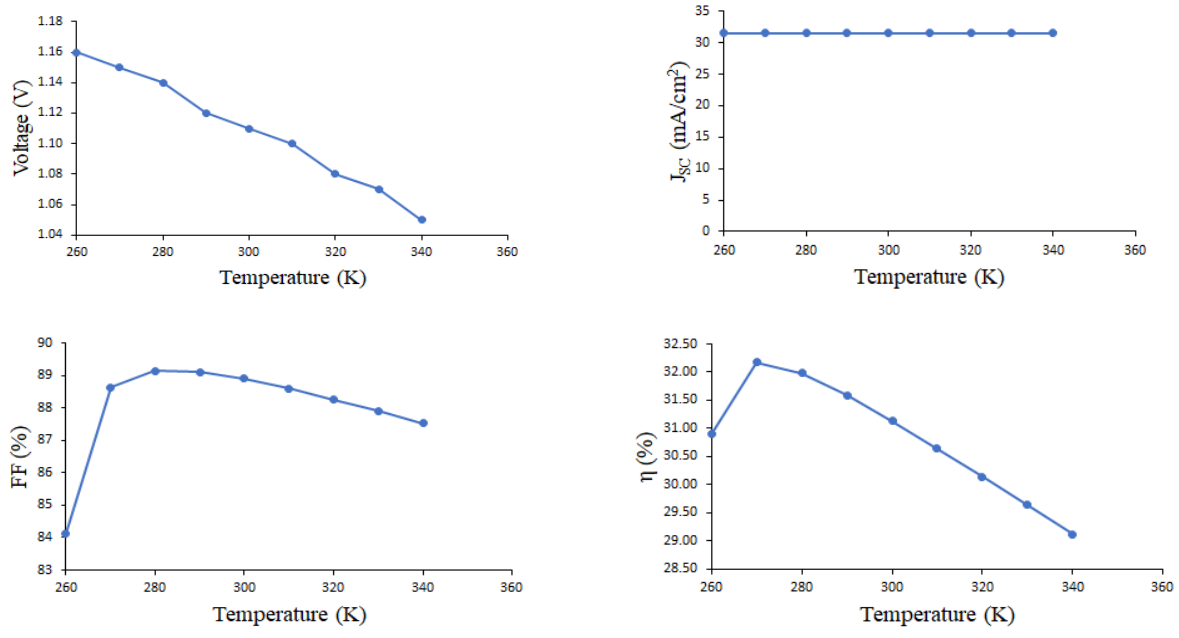

Figure 11. Variation of Voc, Jsc, FF and η with increasing temperature

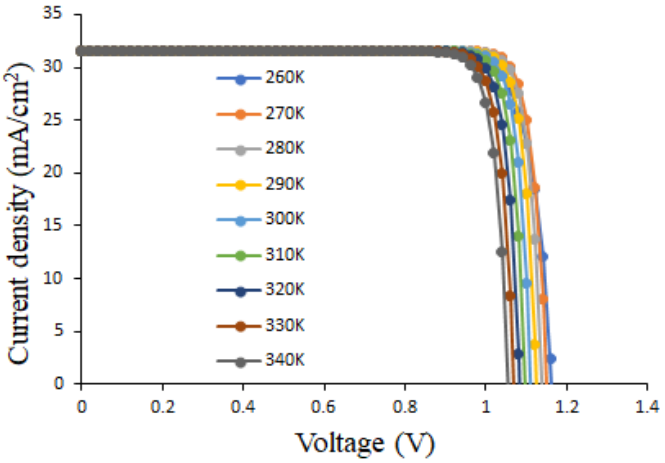

Figure 12. J-V curves of CIGS solar cells with increasing temperature

4. CONCLUSION

This research work investigated the influence of absorber bandgap, absorber layer electron affinity, buffer bandgap and buffer electron affinity by means of SCAPS simulation. The efficiency of the initial device which was set up in line with our previous work yielded an efficiency of 25.85% and on optimization of the aforementioned parameters, optimal values of 1.4 eV, 4.45 eV, 3.0 eV and 4.05 eV respectively, were obtained. These values were used together with optimum values of multivalent defect density (1E + 10 cm^{-3}) in absorber, absorber layer thickness (1.2µm) and buffer layer thickness (0.01 µm) obtained in our previously published work, to simulate a solar cell which turned out to be the best device having photovoltaic parameters with a V_{OC} of 1.11 V, J_{SC} of 31.55 mA/cm^2, fill factor of 88.91 %. and efficiency of 31.13 %. Except for J_{SC}, these values are higher than those obtained in our paper, where the best device had photovoltaic parameters with V_{OC} of 0.83 V, J_{SC} of 37.75 mA/cm^2, fill factor of 86.26 % and an efficiency of 27.00 %. This clearly shows that the cumulative effect of optimizing more parameters of the absorber and buffer layer produces better performing solar cells (as three parameters were used to produce the optimized solar cell in our former paper whereas in this work, seven were used). Lastly, the effect of working temperature on the optimized solar cell was investigated. The study showed that the best performance of the optimized device was achieved at 270 K and the photovoltaic parameters corresponding to this optimum working temperature are; V_{OC} of 1.15 V, J_{SC} of 31.55 mA/cm^2, FF of 88.64 % and an efficiency of 32.18 %. At 270 K, this best device would work optimally in cold countries of the world like Russia and Canada were temperatures can get as low as 268 K.

Acknowledgement

The authors would like to thank Professor Marc Burgelman, Department of Electronics and Information Systems, University of Gent for the development of the SCAPS software package and allowing its use.

Conflict of interest. Authors have declared that there was no conflict of interest.
Funding. This article did not receive any funding support.

ORCID IDs

Eli Danladi, https://orcid.org/0000-0001-5109-4690

REFERENCES

[1] O.I. Okoro, and T.C. Madueme, Nigerian Journal of Technology, **23,** 58 (2004). https://www.ajol.info/index.php/njt/article/view/123333/112876
[2] B. Padmanabham, Master's Degree Thesis, Arizona state University (2008).
[3] C.O. Lawani, G.J. Ibeh, O.O. Ige, E. Danladi, J.O. Emmanuel, A.J. Ukwenya, and P.O. Oyedare, Journal of the Nigerian Society of physical Sciences, **3**, 48 (2021). https://doi.org/10.46481/jnsps.2021.333
[4] S. Wei, S. Zhang, and A. Zunger, "Effects of Ga addition to $CuInSe_2$on its electronic, structural and defect properties", Applied Physics letters, **72,** 3199, (1998). http://dx.doi.org/10.1063/1.121548
[5] G. Hanna, A. Jasenek, U. Rau, and H.W. Schock, Thin Solid Film, **387,** 71 (2001). https://doi.org/10.1016/S0040-6090(00)01710-7
[6] C. Daniella, F. Popescu, P. Joan, and V. Andrei, Procedia-Social and Behavioural Sciences, **191**, 512 (2015). https://doi.org/10.1016/j.sbspro.2015.04.284
[7] C. Liu, and W. Liu, Optik, **127,** 7359-7366, (2016). https://doi.org/10.1016/j.ijleo.2016.05.045
[8] R. Scheer, and H. Schock, *Solar Energy & Photovoltaics*, (John Wiley & Sons, Inc., 2011), pp. 384.
[9] Z. Mohammadi, Journal of Fundamental and Applied Sciences, **8**, 935 (2016). https://doi.org/10.4314/jfas.v8i3s.114
[10] L. Puyvelde, Doctoral dissertation, Ghent university, Belgium (2015).
[11] A. Sylla, S. Toure, and J. Vilcot, International Journal of Science and Research, **6**, 855-860, (2015).
[12] M.I. Hossain, P. Chelvanathan, M. Zaman, M. Karim, M. Alghoul, and N. Amin, Chalcogenide Letters, **8**, 315-324, (2011). http://chalcogen.ro/315_Hossain.pdf

[13] M. Green, *Eagle Cliffs*, (Prentice Hall, 1982).
[14] S. Ruhle, Solar Energy, **130**, 139 (2016). https://doi.org/10.1016/j.solener.2016.02.015
[15] P. Jackson, R. Wuerz, D. Hariskos, E. Lotter, W. Witte, and M. Powalla, Physica Status Solidi, **10**, 583 (2016). https://doi.org/10.1002/pssr.201600199
[16] P. Jackson, D. Hariskos, R. Wuerz, W. Wischmann, and M. Powalla, Physica Status Solidi, **8**, 219-222, (2014). https://doi.org/10.1002/pssr.201409040
[17] ZWS, ZSW-CIGS22Percent-en.pdf (2016). https://www.zsw-bw.de/fileadmin/user_upload/PDFs/Pressemitteilungen/2016/pi07-2016-ZSW-CIGS22Percent-en.pdf
[18] K. Sobayel, K.S. Rahman, M.R. Karim, M.O. Aijaz, M.A. Dar, M.A. Shar, H. Misran, and N. Amin, Chalcogenide Letters, **15**, 333-340, (2018). https://chalcogen.ro/307_SobayelK.pdf
[19] M. Green, Progress in Photovoltaic Research and Application **11**, 333-340, (2003). https://doi.org/10.1002/pip.496
[20] P. Chelvanatan, M.I. Hossain, and N. Amin, Current applied physics, **10**, S387-S391, (2010). https://doi.org/10.1016/j.cap.2010.02.018

ПОКРАЩЕНА ПРОДУКТИВНІСТЬ СОНЯЧНОЇ БАТАРЕЇ $CuIn_{1-x}G_xSe_2$ ЗАВДЯКИ ОПТИМІЗАЦІЇ ВЛАСТИВОСТЕЙ АБСОРБЕРА ТА БУФЕРНОГО ШАРУ ЗА ДОПОМОГОЮ SCAPS-1D

Годвін Дж. Ібе[a], Селін О. Лавані[a], Джаєола О. Еммануель[b], Пітер О. Ойедаре[c], Елі Данладі[d], Олуміде О. Іге[a]
[a]Фізичний факультет Нігерійської оборонної академії, Кадуна, Нігерія.
[b]Відділ фундаментальних наук і загальних досліджень, Федеральний коледж механізації лісового господарства, Кадуна, Нігерія
[c]Департамент наукових лабораторних технологій, Федеральна політехніка Еде, штат Осун, Нігерія
[d]Фізичний факультет, Федеральний університет наук про здоров'я, Отукпо, штат Бенуе, Нігерія

Це дослідження є продовженням нашої раніше опублікованої статті на тему «Чисельне моделювання сонячних елементів із діселеніду міді, індій-галію з використанням одновимірного програмного забезпечення SCAPS». Було оптимізовано ще п'ять параметрів, а саме: ширину забороненої зони поглинача, спорідненість до електронів поглинача, ширину забороненої зони буферного шару, спорідненість до електронів буферного шару та робочу температуру за допомогою того самого інструменту моделювання, який використовувався спочатку. Коли ширина забороненої зони поглинача змінювалася між 0,8 еВ і 1,6 еВ, ефективність сонячної батареї зростала, поки не досягла свого піку в 27,81 %. Це сталося при ширині забороненої зони поглинача 1,4 еВ. Інші фотоелектричні параметри при цьому оптимальному значенні: V_{oc} 1,00 В, J_{sc} 31,99 мА/см^2 і FF 87,47 %. Змінюючи спорідненість до електронів поглинача від 4,20 еВ до 4,55 еВ, ми отримали оптимальне значення 4,45 еВ при V_{oc} 0,82 В, J_{sc} 37,96 мА/см^2, FF 84,99 % і ефективність 26,36 %. Оптимізація ширини забороненої зони буфера призвела до оптимального значення 3,0 еВ, коли ширина забороненої зони буфера змінювалася між 1,6 еВ і 3,2 еВ. Фотоелектричні параметри при цьому оптимальному значенні: V_{oc} 0,80 В, J_{sc} 37,96 мА/см^2, FF 85,22 % і ККД 25,86 %. Вплив буферної електронної спорідненості досліджували, варіюючи його значення між 4,00 еВ і 4,40 еВ, і було встановлено, що його найкраще значення становить 4,05 еВ при фотоелектричних параметрах з V_{oc} 0,82 В, J_{sc} 37,96 мА/см^2, FF 84,98 % і ККД 26,36 %. Ці оптимізовані значення всіх параметрів були використані для моделювання сонячної батареї, що призвело до пристрою з характеристиками: V_{oc} 1,11 В, J_{sc} 31,50 мА/см^2, FF 88,91 % і ККД 31,11 %. Змінюючи робочу температуру оптимізованої сонячної батареї, оптимізований пристрій має найкращу продуктивність при 270 К із фотоелектричними (PV) значеннями V_{oc} 1,15 В, J_{sc} 31,55 мА/см^2, FF 88,64 % і ефективністю 32,18 %. Отримані результати були обнадійливими і можуть служити керівництвом для тих, хто бере участь у практичних розробках сонячних елементів.

Ключові слова: SCAPS, буферний шар, сонячні елементи, фотоелектричні

EAST EUROPEAN JOURNAL OF PHYSICS. 3. 77-83 (2022)
DOI:10.26565/2312-4334-2022-3-10 ISSN 2312-4334

SLOW SURFACE EIGENMODES DIRECTED BY THE Mu-NEGATIVE METAMATERIAL SLAB†

Viktor K. Galaydych*, Oleksandr E. Sporov, Volodymyr P. Olefir, Mykola O. Azarenkov
V.N. Karazin Kharkiv National University, 4 Svobody Sq., Kharkiv, 61022, Ukraine
**Corresponding Author: galaydych@karazin.ua*
Received July 10, 2022; revised August 8, 2022; accepted August 15, 2022

The paper presents the results of the study of slow surface electromagnetic waves directed along the flat mu-negative metamaterial slab surrounded by ordinary dielectric material. It is considered the case of isotropic and homogeneous metamaterial without losses. This metamaterial possesses the positive permittivity and the negative permeability over a definite frequency band. It is found that two surface modes of TE polarization can propagate along such waveguide structure. The dispersion properties, the spatial distribution of the electromagnetic field, as well as the phase and group velocities of these slow modes are studied. The first mode is a conventional forward wave, and has a lower frequency and lower phase velocity than the second mode. The second mode may have zero group velocity at a certain frequency. Characteristics of these surface modes for different values of the mu-negative slab parameters have been studied. The studied surface electromagnetic waves can be used for practical applications as in laboratory experiments, as in various technologies.
Keywords: mu-negative metamaterial; electromagnetic surface wave; wave dispersion properties; spatial wave structure
PACS: 52.35g, 52.50.Dg

In recent years it was carried out the intensive study of the artificially created materials with special extraordinary electromagnetic properties – so called metamaterials. Such metamaterials are the innovative composite materials that consist of artificially constructed periodical structure of small-size units that play the role of atoms for electromagnetic waves. The main aim of creation of such innovation is to get definite combinations of electromagnetic characteristics that do not occur in nature. Firstly, the main attention of researches was paid to the double negative (so-called left-handed) metamaterials, with simultaneously negative value of permittivity and permeability [1,2]. These left-handed metamaterials are mainly interested with the possibility of realizing a negative refractive index for the creation of ideal lenses and other devices which contain such metamaterials [3-9]. Next, for these purposes there were also created mono-negative metamaterials, for example, with positive permittivity and negative permeability values – so called mu-negative metamaterials [10,11]. No doubt that creating such mono-negative metamaterials is easier in comparison with double-negative ones [2]. Just now it was found that along the interface between a medium with negative permeability and vacuum the surface electromagnetic waves can propagate [11]. The real devices are spatially bounded, so it is necessary to study the electrodynamic properties of the waveguide structure with flat mu-negative metamaterial slab surrounded by ordinary dielectric material. In this paper we represent a new surface electromagnetic eigenmodes that can propagate along such waveguide structure.

TASK SETTINGS

Let us study the electrodynamic properties of waveguide structure that is composed of mu-negative metamaterial layer with thickness d with negative permeability $\mu(\omega)<0$ and constant positive permittivity ε. The coordinate axis X is directed along this slab (Fig. 1).

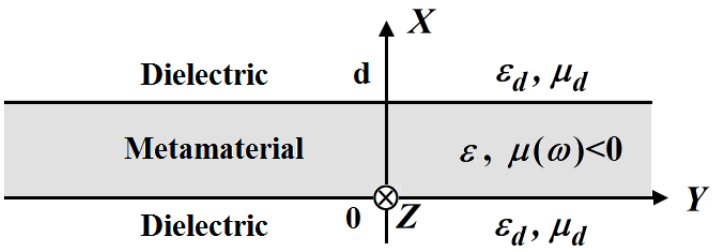

Figure 1. The geometry of problem

This metamaterial slab in immersed into ordinary unbounded dielectric without losses with permittivity ε_d and permeability μ_d. Further study was carried out for the waveguide structure with permittivity $\varepsilon=1$, and permeability

† ***Cite as:*** V.K. Galaydych, O.E. Sporov, V.P. Olefir, and M.O. Azarenkov, East Eur. J. Phys. **3**, 77 (2022), https://doi.org/10.26565/2312-4334-2022-3-10

$\mu(\omega)$ that depends on the circular wave frequency ω according to the following law, which is in accordance with the experimental data [10]

$$\mu(\omega) = 1 - \frac{F\omega^2}{\omega^2 - \omega_0^2}, \tag{1}$$

where ω_0 – is the characteristic frequency of the metamaterial and in our case $\omega_0 / 2\pi = 4\ \text{ГГц}$; the parameter $F = 0.56$.

Let study slow electromagnetic waves, that propagate along flat waveguide structure in the direction of the Z axis (Fig. 1). It was assumed that the wave disturbances exponentially tend to zero far away from both boundaries. The dependence of the wave components on time t and coordinates x and z are expressed the following form:

$$E, H \propto E(x), H(x)\exp[i(k_3 z - \omega t)], \tag{2}$$

here z lies at the separation plane, and x is the coordinate rectangular to the wave propagation direction and k_3 – is the longitudinal wavenumber.

In the considered case it is possible to split the system of Maxwell equations in to two sub-systems. One of them describes TE-waves and another – TM- waves.

Let us find the solution of the Maxwell system of equations for TE-wave that satisfy the boundary conditions at the interface between the metamaterial and the dielectric. As a result, one can obtain the wave field components and the dispersion equation of the eigen electromagnetic E-wave (TM-wave) of the considered planar structure.

The wave field components of the E-wave in the dielectric region $x \le 0$ can be written as:

$$\begin{cases} H_y(x) = H_y(0)e^{h_d x}, \\ E_x(x) = H_y(0)k_3 e^{h_d x} c / (\varepsilon_d\, \omega), \\ E_z(x) = i\, H_y(0) h_d e^{h_d x} c / (\varepsilon_d\, \omega), \end{cases} \tag{3}$$

where c – is speed of light in vacuum.

The wave field components of the E-wave in the metamaterial region $0 \le x \le d$ can be found in the following form:

$$\begin{cases} H_y(x) = H_y(0)\left[cosh(\kappa x) + \dfrac{h_d \varepsilon\ sinh(\kappa x)}{\varepsilon_d \kappa} \right], \\ E_x(x) = H_y(0)\dfrac{ck_3}{\varepsilon\varepsilon_d \kappa\omega}\left[\varepsilon_d \kappa\ cosh(\kappa x) + h_d \varepsilon\ sinh(\kappa x) \right], \\ E_z(x) = H_y(0)\dfrac{ic}{\varepsilon\varepsilon_d \omega}\left[h_d \varepsilon\ cosh(\kappa x) + \varepsilon_d \kappa\ sinh(\kappa x) \right]. \end{cases} \tag{4}$$

The wave field components of the E-wave (TM-wave) in the dielectric region $x \ge d$ may be expressed as:

$$\begin{cases} H_y(x) = H_y(0)e^{h_d(-x+d)}\left[\dfrac{\varepsilon_d \kappa\ cosh(\kappa d) + h_d \varepsilon\ sinh(\kappa d)}{\varepsilon_d \kappa} \right], \\ E_x(x) = H_y(0)\dfrac{ck_3}{\varepsilon_d^2 \kappa\omega} e^{h_d(-x+d)}\left[\varepsilon_d \kappa\ cosh(\kappa d) + h_d \varepsilon\ sinh(\kappa d) \right], \\ E_z(x) = -H_y(0)\dfrac{ich_d}{\varepsilon_d^2 \kappa\omega} e^{h_d(-x+d)}\left[\varepsilon_d \kappa\ cosh(\kappa d) + h_d \varepsilon\ sinh(\kappa d) \right]. \end{cases} \tag{5}$$

The dispersion equation for the E-wave (TM-wave) has the following form:

$$2h_d \varepsilon\varepsilon_d \kappa\ cosh(\kappa d) + \left(h_d^2 \varepsilon^2 + \varepsilon_d^2 \kappa^2 \right) sinh(\kappa d) = 0, \tag{6}$$

where $h_d = h_d(k_3, \omega) = \sqrt{k_3^2 - \varepsilon_d \cdot \mu_d \cdot k^2}$ – is transversal wave number in dielectric region, $k = \omega / c$ – the wavenumber in vacuum; $\kappa = \kappa(k_3, \omega) = \sqrt{k_3^2 - \varepsilon \cdot \mu(\omega) \cdot k^2}$ – the transversal wavenumber in metamaterial.

Analogous computations for TM- wave leads to the equations for the wave field components and the dispersion equation of the eigen electromagnetic H-wave (TE-wave) of the considered flat waveguide structure.

The wave field components of the electromagnetic H-wave (TE-wave) in dielectric region $x \le 0$ may be written as:

$$\begin{cases} E_y(x) = E_y(0)e^{h_d x}, \\ H_x(x) = -E_y(0)ck_3 e^{h_d x} / (\mu_d\, \omega), \\ H_z(x) = -i\, E_y(0)ch_d e^{h_d x} / (\mu_d\, \omega). \end{cases} \tag{7}$$

The wave field components of the electromagnetic H-wave (TE-wave) in metamaterial region $0 \le x \le d$ has the following form:

$$\begin{cases} E_y(x) = E_y(0)e^{h_d x}\left[cosh(\kappa x) + \dfrac{h_d \mu\ sinh(\kappa x)}{\mu_d \kappa} \right], \\ H_x(x) = -E_y(0)\dfrac{ck_3}{\kappa\mu\mu_d\omega}\left[\kappa\mu_d\ cosh(\kappa x) + h_d\mu\ sinh(\kappa x) \right], \\ H_z(x) = -E_y(0)\dfrac{ic}{\mu\mu_d\omega}\left[\mu h_d\ cosh(\kappa x) + \kappa\mu_d\ sinh(\kappa x) \right]. \end{cases} \tag{8}$$

The wave field components of the electromagnetic H-wave (TE-wave) in dielectric region $x \ge d$ can be written as:

$$\begin{cases} E_y(x) = E_y(0)e^{h_d(-x+d)}\left[\dfrac{\kappa\,\mu_d\ cosh(\kappa d) + h_d\mu\ sinh(\kappa d)}{\mu_d \kappa} \right], \\ H_x(x) = -E_y(0)\dfrac{ck_3}{\kappa\,\mu_d^2\,\omega}e^{h_d(-x+d)}\left[\kappa\,\mu_d\ cosh(\kappa d) + h_d\,\mu\ sinh(\kappa d) \right], \\ H_z(x) = E_y(0)\dfrac{ich_d}{\kappa\,\mu_d^2\,\omega}e^{h_d(-x+d)}\left[\kappa\,\mu_d\ cosh(\kappa d) + h_d\,\mu\ sinh(\kappa d) \right]. \end{cases} \tag{9}$$

The dispersion equation for the electromagnetic H-wave (TE-wave) can be written in the following form

$$2h_d\kappa\mu\mu_d\ cosh(\kappa d) + \left(h_d^2\mu^2 + \kappa^2\mu_d^2 \right) sinh(\kappa d) = 0\,. \tag{10}$$

RESULTS AND DISCUSSION

Let study the properties of the waves that govern by the dispersion equations (6, 10) for the arbitrary set of parameters. It was shown that in the frequency range when the metamaterial is mu-negative the equation for the TM-wave (6) has no solutions and only the equation (10) for TE-wave has the solutions. To study the properties of these solutions let us introduce the following dimensionless quantities: the normalized circular frequency $\Omega = \omega / \omega_0$, normalized wavenumber $\beta = k_3 c / \omega_0$ and normalized thickness of the metamaterial layer $\Delta = d\ \omega_0 / c$.

The solutions of the dispersion equation (10) for the TE modes for the such set of parameters: $\varepsilon = 1$, $\varepsilon_d = 1$, $\mu_d = 1$, $\Delta = 0.4$ (the case of thin metamaterial slab) are presented at Fig. 2, 3. It was found that the dispersion equation (10) possesses two eigen solutions that are shown at Fig. 2.

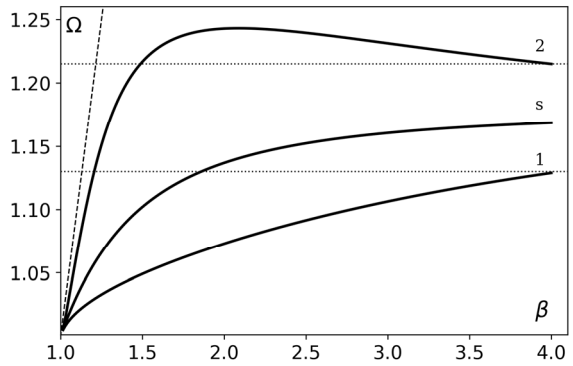

Figure 2. The solution of the dispersion equation (10) for TE-modes for $\varepsilon = 1, \varepsilon_d = 1, \mu_d = 1,\ \Delta = 0.4$. The curves marked by the numbers 1 and 2 corresponds to the two eigenmodes of waveguide structure. Line marked by the letter 's' corresponds to the eigen wave of the simplified model, presented in [12].

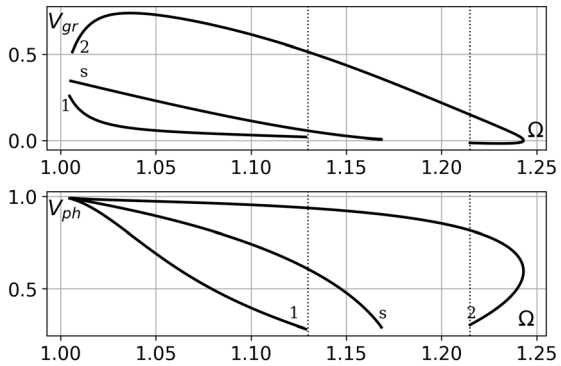

Figure 3. The group V_{gr} and phase V_{ph} normalized velocities of TE modes presented on the Figure 2. The parameters set and curve numbering are the same as for the Figure 2.

The presented solutions (eigenmodes of TE-type) of the dispersion equation (10) for the studied model are marked by the numbers 1 and 2. The line, marked by the letter 's' corresponds to the single eigenwave of the simplified waveguide model, presented in [12] under the same parameter set. The further analysis has shown that this solution for the simplified model corresponds to the low frequency solution (curve 1) for the model considered.

The mutual location of the dispersion curves 1 and 2 in Fig. 2 indicates the existence of three different regions of the frequency interval. In the Fig. 2 these regions are separated from each other by the dashed horizontal lines. In the first frequency region $1.04 < \Omega < 1.13$ two modes of TE-type that corresponds to different solutions of the dispersion equation (10) with the same frequency can simultaneously propagate in the considered flat bounded structure. In the second frequency region $1.13 < \Omega < 1.215$ the excitation of only one mode that corresponds to the solution 2 with harmonic spatial dependence is possible. Finally, in the third frequency region $1.215 < \Omega < 1.243$, the propagation of two harmonic waves that corresponds to the solution 2 with the same frequency, but with different wavelengths takes place.

Figure 3 presents the dependence of the group $V_{gr}=c^{-1}d\omega/dk_3$ and phase $V_{ph}=\omega/(k_3 c)$ normalized velocities for two eigen TE-modes upon the normalized frequency Ω. The parameters set and curve numbering are the same as for the Figure 2. One can see the analogous to Figure 2 three frequency regions that are separated from each other by the dashed vertical lines in Fig. 3. In the first frequency region $1.04 < \Omega < 1.13$ one can observe two slow modes that simultaneously propagate in the considered flat structure with the same frequency. These two modes possess group and phase velocities that coincide in direction but have different values, respectively. In the second frequency range $1.13 < \Omega < 1.215$ it is possible the excitation of slow mode 2 only. The phase velocity of this wave is about 0.9 of the speed of light, and its group velocity decreases with the frequency increase from $0.5c$ down to $0.2c$ according to an almost linear law. In the third frequency region $1.215 < \Omega < 1.243$ one can observe the propagation of two harmonic waves of the mode 2 with the same frequency but different wavelengths. The group velocities of these waves are of different signs.

The spatial wave field structure of such waves is presented in Figs. 4, 5. The calculations are carried out for the same parameters set as for the Figs. 2, 3: $\varepsilon = 1$, $\varepsilon_d = 1$, $\mu_d = 1$, $\Delta = 0.4$. The wave field components, normalized by the $E_y(0)$ are calculated for $\beta = 4$ and obtained from the dispersion equation (10) eigen frequency value $\Omega = 1.1288$ for the mode 1 (see Fig. 4), and for the $\Omega = 1.21496$ for the mode 2 (see Fig. 5).

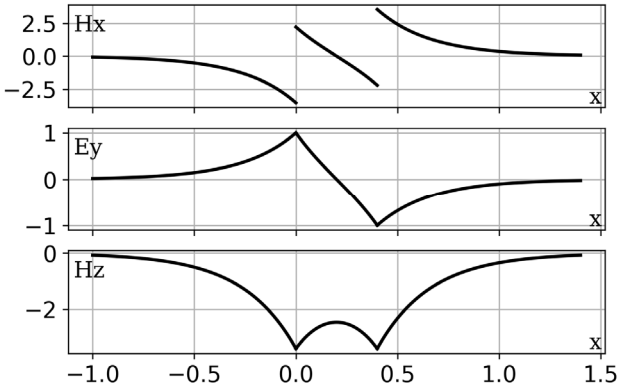

Figure 4. The wave field components normalized on the $E_y(0)$ for the mode 1 in the Fig. 2. The parameters set are the same as was used for the Fig. 2. The wave field structure is calculated for $\beta = 4$ and eigen wave frequency $\Omega = 1.1288$.

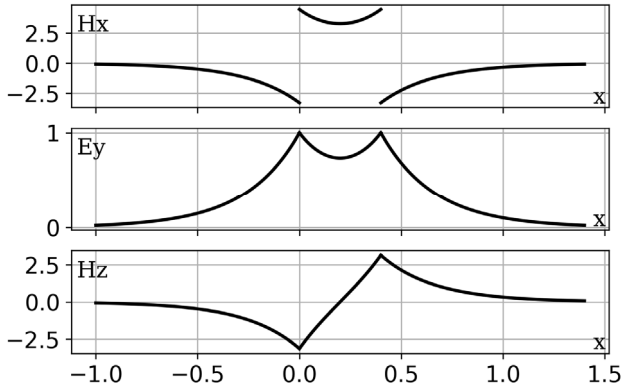

Figure 5. The wave field components normalized on the $E_y(0)$ for the mode 2 in the Fig. 2. The parameters set are the same as was used for the Fig. 2. The wave field structure is calculated for $\beta = 4$ and eigen wave frequency $\Omega = 1.21496$.

The solutions of the dispersion equation (10) in the case of rather thick metamaterial slab for the TE modes for the such set of parameters: $\varepsilon = 1$, $\varepsilon_d = 1$, $\mu_d = 1$, $\Delta = 0.8$ are presented at Fig. 6, 7. The numbering of the curve are the same as for the Fig. 2.

The increase of the metamaterial layer thickness leads to the gradually convergence of the both curves 1 and 2 to each other, and to the solution of the simplified waveguide model, presented in [12] under the same parameter set (see Fig. 8). This figure presents the variation of the wave eigen frequency Ω obtained due to the solution of the dispersion equation (10) when $\varepsilon = 1$, $\varepsilon_d = 1$, $\mu_d = 1$ for $\beta = 4$ while normalized metamaterial slab thickness varies from $\Delta = 0.4$ up to $\Delta = 0.8$.

Also, the increase of metamaterial thickness Δ leads to the frequency ranges change. So, for the increase of Δ from 0.4 up to 0.8 results in the increase of the first frequency range and the decrease of the second, and especially third frequency ranges where the only wave 2 can exist (see Fig. 6). The region where the TE mode 2 has negative group frequency value became extremely small (see Fig. 7). So, one can effectively control the propagation properties of TE modes due to the variation of metamaterial slab thickness.

The wave spatial wave structure for the mode 2 for the parameters set analogous to that of Fig. 6 for the region, where wave group velocity tends to zero: $V_{gr} \sim 0$ ($\beta \approx 2.804$, $\Omega \approx 1.178$) is presented at Fig. 8. This wave is of a surface wavy type and can be treated as the standing wave due to superposition of two TE type 2 modes that have equal both frequencies and wavenumber but propagate in opposite directions.

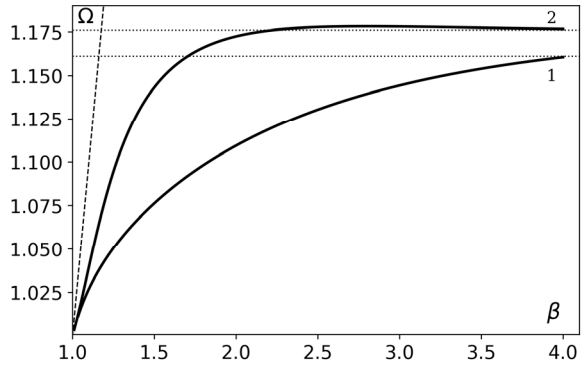

Figure 6. The solution of the dispersion equation (10) for TE-modes for $\varepsilon = 1$, $\varepsilon_d = 1$, $\mu_d = 1$, $\Delta = 0.8$. The curves marked by the numbers 1 and 2 corresponds to the two eigenmodes of waveguide structure.

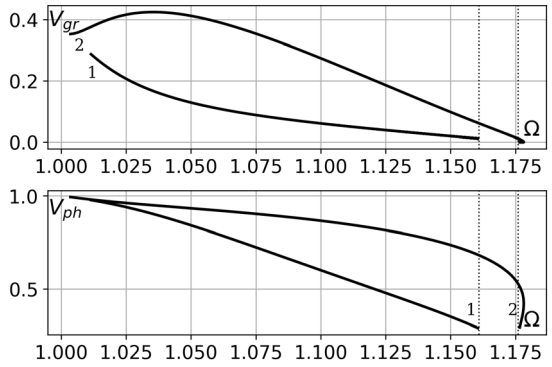

Figure 7. The group V_{gr} and phase V_{ph} normalized velocities of TE modes presented on the Figure 6. The parameters set and curve numbering are the same as for the Figure 6

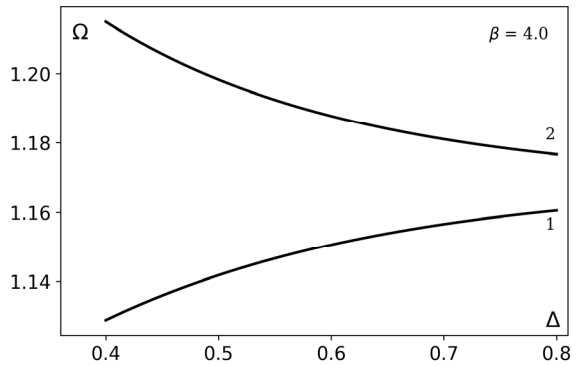

Figure 8. The variation of the normalized wave eigen frequency Ω obtained due to the solution of the dispersion equation (10) when $\varepsilon = 1$, $\varepsilon_d = 1$, $\mu_d = 1$ for $\beta = 4$.

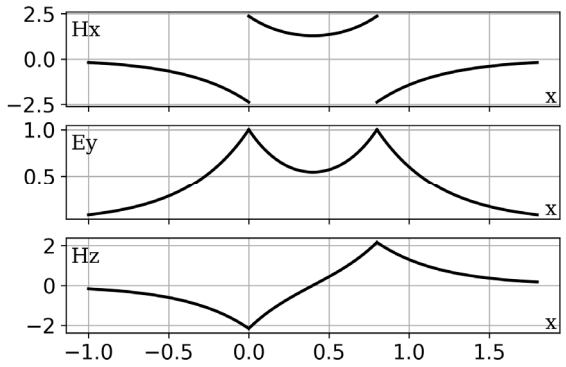

Figure 9. The wave field components normalized on the $E_y(0)$ for the mode 2 in the Fig. 6. The parameters set are the same as was used for the Fig. 6. The wave field structure is calculated for the region when $V_{gr} \sim 0$ ($\beta \approx 2.804$, $\Omega \approx 1.178$).

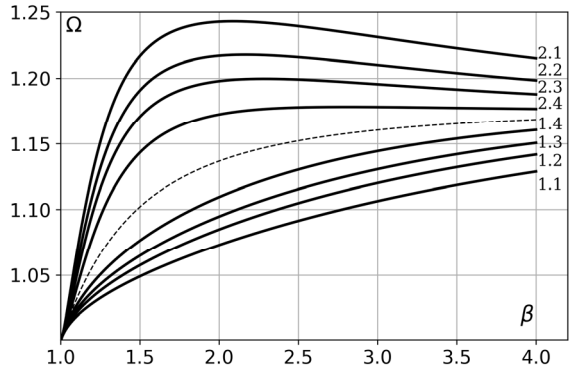

Figure 10. The solution of the dispersion equation (10) for TE-modes for $\varepsilon = 1$, $\varepsilon_d = 1$, $\mu_d = 1$. The curves marked by the numbers 1 and 2 before point corresponds to the two eigenmodes of waveguide structure. The numbers after the point corresponds to different Δ value: 1 – 0.4, 2 – 0.5, 3 - 0.6, 4 – 0.8. Dashed curve corresponds to the eigen wave of the simplified model, presented in [12].

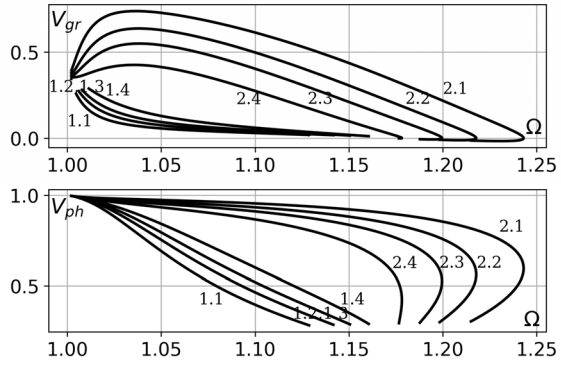

Figure 11. The group V_{gr} and phase V_{ph} normalized velocities of TE-modes presented on the Figure 10. The parameters set and curve numbering are the same as for the Figure 10.

The dependence of the normalized frequency Ω of the eigen TE waves of the considered structure versus normalized wavenumber β for $\varepsilon = 1, \varepsilon_d = 1,\ \mu_d = 1$. The curves marked by the numbers 1 and 2 before point corresponds to the first and second eigenwaves of waveguide structure. The numbers after the point corresponds to different Δ value: 1 – $\Delta = 0.4$, 2 – $\Delta = 0.5$, 3 – $\Delta = 0.6$, 4 – $\Delta = 0.8$. Dashed curve corresponds to the eigen wave of the simplified model, presented in [12]. It is shown, how gradually increase of metamaterial slab thickness leads to the appropriate convergence of two eigen modes of the considered waveguide structure to the eigen wave of the simplified model, presented in [12] for the same parameter set. It is necessary to mention the possibility of the effective control of the frequency ranges where two or only one eigen mode of the considered waveguide structure exist due to the appropriative choice of the metamaterial slab thickness.

The dependence of the group V_{gr} and phase V_{ph} normalized velocities for two eigen TE-modes versus the normalized frequency Ω for the same parameter set as for the Fig. 10 is presented in the Fig. 11.

The numbering of the curve is the same as for the Fig. 10. It is shown that due to variation of the metamaterial slab thickness it is possible to manage of the frequency region size where the mode that propagates along the considered structure is single and possess the negative group velocity.

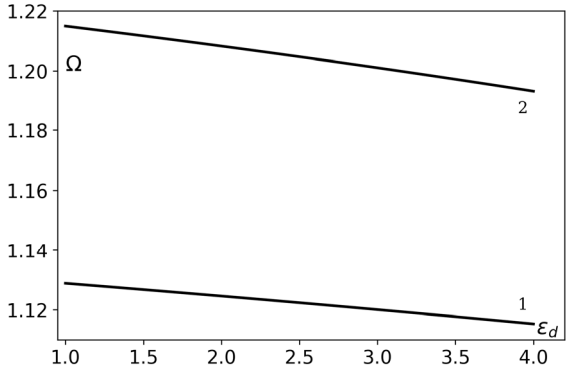

Figure 12. The dependence of the eigen TE wave normalized frequency Ω when $\varepsilon = 1,\ \mu_d = 1,\ \Delta = 0.4$ for $\beta = 4$ versus the ε_d value

The dependence of the obtained solutions of the dispersion equation (10) upon the permittivity constant of ordinary dielectric ε_d for the following parameter set $\varepsilon = 1, \mu_d = 1,\ \Delta = 0.4$ and for $\beta = 4$ is presented at the Fig. 12. It is obtained that the increase of the ε_d parameter leads to the slight decrease of the wave frequency Ω for both modes.

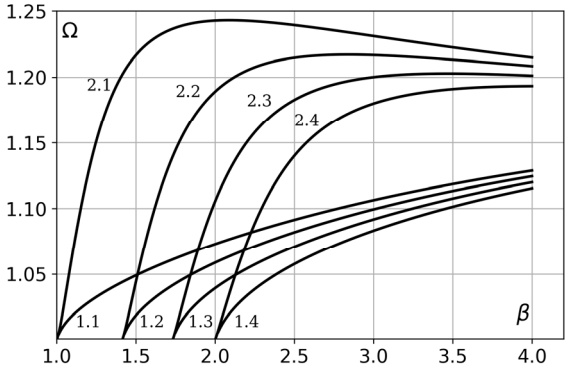

Figure 13. The solution of the dispersion equation (10) for TE-modes for $\varepsilon = 1,\ \mu_d = 1,\ \Delta = 0.4$. The curves marked by the numbers 1 and 2 before point corresponds to the two eigenmodes of waveguide structure. The numbers after the point corresponds to different ε_d value.

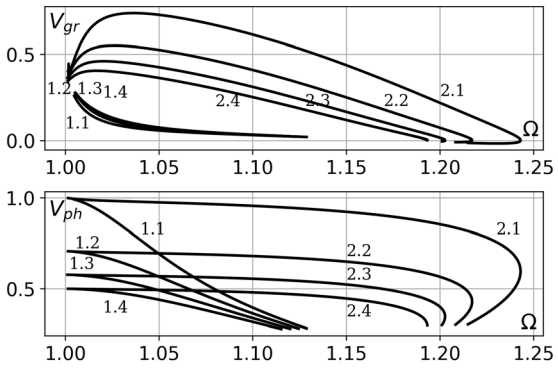

Figure 14. The group V_{gr} and phase V_{ph} normalized velocities of TE modes presented on the Figure 13. The parameters set and curve numbering are the same as for the Figure 13.

The detailed analysis of the impact of the ε_d parameter on the dispersion properties of the TE eigen waves on the waveguide considered is presented in Fig. 13. The calculations were made for the following problem parameter set: $\varepsilon = 1,\ \mu_d = 1,\ \Delta = 0.4$. The curves marked by the numbers 1 and 2 before the point corresponds to the first and second eigenwaves of waveguide structure. The numbers after the point corresponds to solutions for different ε_d value:

1 - $\varepsilon_d = 1$, 2 – $\varepsilon_d = 2$, 3 – $\varepsilon_d = 3$, 4 – $\varepsilon_d = 4$. It is shown, that the increase of the ε_d value results to the decrease and even to the disappearance of the third, most high-frequency region of the frequency interval. At the same time the first and the second frequency regions, where two eigen TE modes and one eigen TE mode waveguide structure can exist, respectively, stay almost unchangeable. Also, the increase of the ε_d value leads to the essential decrease of the maximum value of the wavelength of the surface modes that can propagate in this structure (see Fig. 13).

The dependence of the group V_{gr} and phase V_{ph} velocities for two eigen TE-modes versus the normalized frequency Ω for the same parameter set as for the Fig. 13 is presented in the Fig. 14. The numbering of the curve is the same as for the Fig. 13. It is shown, that changing the ε_d parameter value leads to the substantial decrease of phase and group velocities of the mode 2 and of the phase velocity of mode 1 (Fig. 14). The group velocity of the mode 1 remains practically unchanged. It is necessary to mention that due to changing ε_d value one can effectively control the size of the frequency region where the single mode 2 possesses negative group velocity (see Fig. 14).

CONCLUSION

It was studied the peculiarities of propagation of slow surface electromagnetic waves directed along the flat mu-negative lossless metamaterial slab surrounded by the ordinary dielectric material. It was found that two electromagnetic surface modes of TE can propagate at the interface between the mu-negative metamaterial layer and a conventional dielectric. It was studied the dispersion properties, spatial distribution of electric and magnetic field amplitudes of these eigenwaves of the considered structure for different problem parameters. It is necessary to mention the existence of new mode, as compared with previously studied simplified model [9]. This new mode can propagate in one mode regime and possesses the frequency range where its group velocity has a negative value. It was found that due to variation or metamaterial slab thickness, or ε_d parameter value one can effectively control the size of the frequency region where this single mode possesses negative group velocity. The obtained results can be useful for both modeling and manufacturing of modern devices based on metamaterials.

This work was supported by the Ministry of Education and Science of Ukraine, under the Projects 22-13-20 and 2-13-21.

ORCID IDs

Viktor K. Galaydych, https://orcid.org/0000-0002-2255-9716; **Oleksandr E. Sporov,** https://orcid.org/0000-0002-4610-9656
Volodymyr P. Olefir, https://orcid.org/0000-0002-8022-2556; **Mykola O. Azarenkov**, https://orcid.org/0000-0002-4019-4933

REFERENCES

[1] I.V. Shadrivov, M. Lapine, and Y.S. Kivshar, editors, *Nonlinear, tunable and active metamaterials* (Springer, 2015). https://link.springer.com/book/10.1007/978-3-319-08386-5
[2] R. Ruppin, Phys. Lett. A, **277**, 61 (2000). https://doi.org/10.1016/S0375-9601(00)00694-0
[3] J.A.Girón-Sedaset al., Superlattices and Microstructures, **117**, 423 (2018). https://doi.org/10.1016/j.spmi.2018.03.062
[4] S.Manjunathet et al., Adv. Optical Mater. **8**, 1901658 (2020). https://doi.org/10.1002/adom.201901658
[5] S.F. Mahmoud, and A.J. Viitanen, Progress in Electromagnetics, **51**, 127 (2005). https://doi.org/10.2528/PIER03102102
[6] V.K. Galaydych, N.A. Azarenkov, V.P. Olefir, and A.E. Sporov, Problems of Atomic Science and Technology, **1**, 96 (2017), https://vant.kipt.kharkov.ua/ARTICLE/VANT_2017_1/article_2017_1_96.pdf
[7] Y. Cho; S. Lee; D.-H. Kim; H. Kim; C. Song; S. Kong; J. Park; C. Seo; and J. Kim, IEEE Transactions on Electromagnetic Compatibility, **60**(4), 1001 (2018). https://doi.org/10.1109/TEMC.2017.2751595
[8] K.L. Tsakmakidis et al., Physical Review B 73, 085104 (2006). https://doi.org/10.1103/PhysRevB.73.085104
[9] V.K. Galaydych, N.A. Azarenkov, V.P. Olefir, and A.E. Sporov, East Eur. J. Phys. **3**, 145 (2021). https://doi.org/10.26565/2312-4334-2021-3-22
[10] J.B. Pendry et al., IEEE Trans. MTT-47, 2075 (1999). https://doi.org/10.1109/22.798002
[11] R. Yahiaoui et al., Appl. Phys. A, **114**, 997 (2014). https://doi.org/10.1007/s00339-013-8033-4
[12] V. Galaydych, and M. Azarenkov, Appl. Phys. B, **128**, 132 (2022). https://doi.org/10.1007/s00340-022-07854-3

ПОВІЛЬНІ ПОВЕРХНЕВІ ВЛАСНІ МОДИ, ЩО ПОШИРЮЮТЬСЯ ВЗДОВЖ ШАРУ МЮ-НЕГАТИВНОГО МЕТАМАТЕРІАЛУ

В.К. Галайдич, О.Є. Споров, В.П. Олефір, М.О. Азарєнков
Харківський національний університет імені В.Н. Каразіна
Україна, Харків, пл. Свободи, 4

У статті наведено результати дослідження повільних поверхневих електромагнітних хвиль, спрямованих уздовж плоскої мю-негативної пластини метаматеріалу, оточеної звичайним діелектричним матеріалом. Розглядається випадок ізотропного і однорідного метаматеріалу без втрат. Цей метаматеріал має додатню електричну та від'ємну магнітну проникності у певному діапазоні частот. Встановлено, що вздовж такої хвилевідної структури можуть поширюватися дві поверхневі моди ТЕ поляризації. Досліджено дисперсійні властивості, просторовий розподіл електромагнітного поля, а також фазові та групові швидкості цих повільних мод. Перша мода є звичайною прямою хвилею і має нижчу частоту та меншу фазову швидкість, ніж друга мода. Друга мода може мати нульову групову швидкість на певній частоті. Досліджено характеристики цих поверхневих мод для різних значень параметрів шару мю-негативного метаматеріалу. Досліджувані поверхневі електромагнітні хвилі можуть бути використані як в лабораторних експериментах, так і в різних технологіях.

Ключові слова: мю-негативний метаматеріал; електромагнітна поверхнева хвиля; дисперсійні властивості хвилі; просторова структура моди

East European Journal of Physics. **3.** 84-90 (2022)
DOI:10.26565/2312-4334-2022-3-11 ISSN 2312-4334

EFFECT OF Na DOPING ON SOME PHYSICAL PROPERTIES OF CHEMICALLY SPRAYED CZTS THIN FILMS†

Noura J. Mahdi, Nabeel A. Bakr*
Department of Physics, College of Science, University of Diyala, Diyala, Iraq
**Corresponding Author: nabeelalibakr@yahoo.com*
Received August 3, 2022; revised August 18, 2022; accepted August 25, 2022

In this work, sodium-doped copper zinc tin sulfide (CZTS) thin films are prepared by depositing them on glass substrates at temperature of (400±10) °C and thickness of (350±10) nm using Chemical Spray Pyrolysis (CSP) technique. 0.02 M of copper chloride dihydrate ($CuCl_2.2H_2O$), 0.01 M of zinc chloride ($ZnCl_2$), 0.01 M of tin chloride dihydrate ($SnCl_2.2H_2O$), and 0.16 M of thiourea ($SC(NH_2)_2$) were used as sources of copper, zinc, tin, and sulphur ions respectively. Sodium chloride (NaCl) at different volumetric ratios of (1, 3, 5, 7 and 9) % was used as a dopant source. The solution is sprayed on glass substrates. XRD diffraction, Raman spectroscopy, FESEM, UV-Vis-NIR, and Hall effect techniques were used to investigate the structural, optical, and electrical properties of the produced films. The XRD diffraction results revealed that all films are polycrystalline, with a tetragonal structure and a preferential orientation along the (112) plane. The crystallite size of all films was estimated using Scherrer's method, and it was found that the crystallite size decreases as the doping ratio increases. The FESEM results revealed the existence of cauliflower-shaped nanoparticles. The optical energy band gap was demonstrated to have a value ranging from 1.6 to 1.51 eV with a high absorption coefficient ($\alpha \geq 10^4$ cm^{-1}) in the visible region of the spectrum. Hall measurements showed that the conductivity of CZTS thin films with various Na doping ratios have p-type electrical conductivity, and it increases as the Na doping ratio increases.
Keywords: CZTS thin films, Na doping, Structural properties, Optical properties, Hall effect.
PACS: 88.40.jn; 73.61.−r; 81.15.Rs; 61.82.Fk; 78.20.−e

Cu_2ZnSnS_4 has been considered an alternative to the well-known Cu(In,Ga)Se_2(CIGS) materials for several years because it is a quaternary semiconductor made up of non-toxic and earth abundant minerals. It is manufactured by replacing the In/Ga in the CIGS system with Zn/Sn, making it a potential candidate for optoelectronic applications. Despite similarities in crystal structure, absorption coefficient, optical band gap Eg, and device architecture between (CZTS) quaternary compound and (CIGS) system, CZTS-based solar cells have a record efficiency of 12.6 %, which is significantly lower than that of CIGS (22.6 %) [1, 2]. Sodium-doped thin films extend the life of defects by passivating them, which has an impact on chemical composition by lowering ZnS development due to Sn loss inhibition [3]. Due to its photoelectric features, such as high absorption coefficient, P type carrier, abundance of its constituents, and absence of component toxicity, the quaternary Cu_2ZnSnS_4 combination is a potential material for low-cost absorption bands in solar cell applications [4, 5]. The efficiency of solar cells has been low in comparison to Cu (In, Ga)Se_2 so far, and this is due to defects and secondary stages [6,7]. Chemical spray pyrolysis has attracted many researchers because it contributes to the preparation of many thin-film materials at a low cost compared to other techniques that require high-cost and complex devices, as well as the fact that it does not require substrates or targets with high quality [8, 9]. The aim of this study is to deposit thin films of CZTS doped with sodium with various concentrations in order to enhance the properties of the CZTS thin films and to compare the experimental results with those of previous studies to better understand the effect of doping on the structural and optical properties of CZTS films.

EXPERIMENTAL PROCEDURE

Chemical spray pyrolysis was used to deposit Cu_2ZnSnS_4 (CZTS) thin films on soda-lime glass substrates at a temperature of 400±10 °C and a thickness of 350±10 nm. The glass substrates are cleaned with ultrasonic waves in distilled water, acetone, and distilled water for a period of no more than 10 minutes, and then dried with soft paper. The spray solution is prepared by dissolving 0.02 M of copper chloride dihydrate ($CuCl_2.2H_2O$), 0.01 M of zinc chloride ($ZnCl_2$), 0.01 M of tin chloride dihydrate ($SnCl_2.2H_2O$), and 0.16 M of thiourea ($SC(NH_2)_2$) in distilled water. Each powder is dissolved separately in a volume of (25 ml) of distilled water, and filtered separately before being mixed together to get the final solution used to prepare the undoped films (CZTS). The doping solution of 0.1 M concentration was made by dissolving 0.5844 g of NaCl in 100 ml of distilled water. This solution is added to the quaternary solution at a volumetric ratios of (1, 3, 5, 7, and 9) % as shown in Table 1. The final solution is mixed for 15 minutes with a magnetic stirrer until a clear homogenous solution is obtained. For weighing powders, an electronic balance (Mettler AE-160 type) with a sensitivity of 10^{-4} g was used. The spraying process is carried out for a period of 10 seconds and to prevent the substrate from losing its heat, the process is paused for 2 minutes. The process is repeated until the desired thickness of the films is achieved. The resulting films are stable with good adhesion and having thickness of 350±10 nm.

† ***Cite as:*** N.J. Mahdi, and N.A. Bakr, East Eur. J. Phys. **3**, 84 (2022), https://doi.org/10.26565/2312-4334-2022-3-11

Table 1. Volumetric doping ratios of sodium chloride used in CZTS thin films preparation.

Sample	Volumetric Doping Ratio %
CZTS1	0 (undoped)
CZTS2	1
CZTS3	3
CZTS4	5
CZTS5	7
CZTS6	9

RESULTS AND DISCUSSION

XRD analysis

Figure 1 shows the X-ray diffraction patterns of Na-doped CZTS films. The figure reveals peaks located at 2θ ~ 28.53°, 33.24°, 47.56° and 56.36°, assigned to the planes (112), (200), (220) and (312) of CZTS kesterite structure respectively based on (ICDD) card number (26-0575) and this is in agreement with the results of previous studies [10-12].

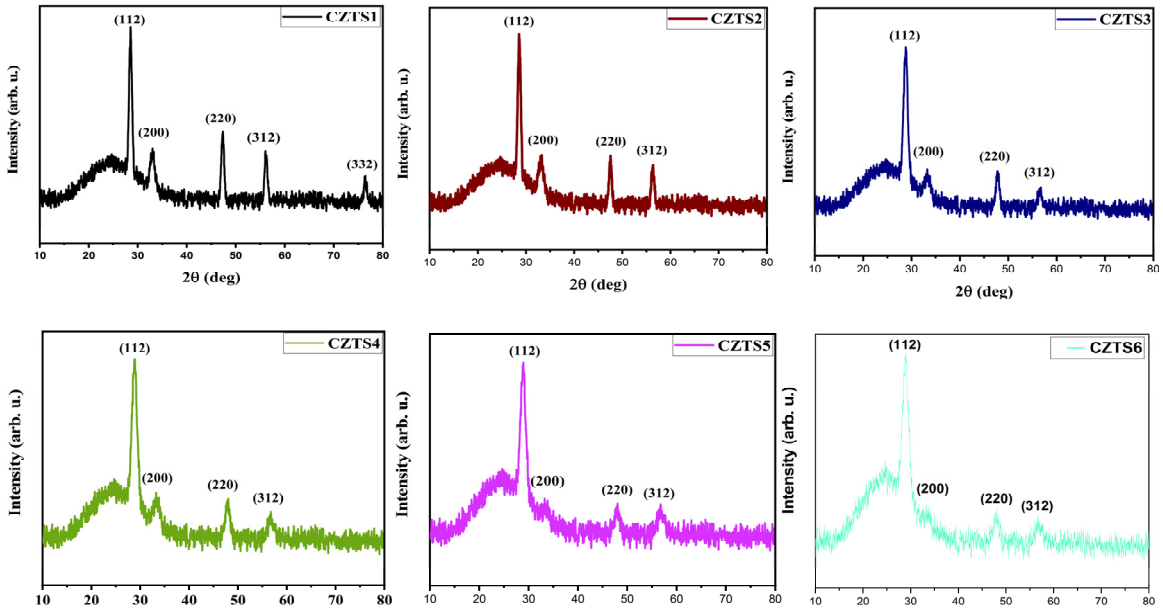

Figure 1. X-ray diffraction patterns of Na-doped CZTS thin films at different doping ratios

The peak appeared at 2θ ~ 76.5° in the XRD pattern of the undoped sample (CZTS1) is assigned to (332) plane and it disappears in the patterns of all doped samples. The X-ray diffraction patterns revealed that the films have multiple diffraction peaks, indicating that the films are polycrystalline with a tetragonal crystal structure, with the preferred growth direction (112) occurring at 2θ ~ 28.5°, which is consistent with previous studies [10,11]. From tetragonal structure the interplanar spacing (d) is given by [13]:

$$\frac{1}{d^2} = \left(\frac{h^2+k^2}{a^2}\right) + \frac{1}{c^2}, \quad (1)$$

Where h, k and l are the Miller indices and a, b and c are lattice constants of the tetragonal unit cell. The lattice constants were estimated and presented in the table (2). It can be seen that the extracted results are close to the standard values of the lattice constants a = b = 5.42 Å and c=10.84 Å. The lattice vector (c/2a) ratio in the ideal tetragonal configuration is 1, and it can be seen that this ratio of all samples is very close to the ideal one. The crystallite size of the Na-doped CZTS thin films is determined by using the Scherrer's formula shown below [14]:

$$D = K\lambda/\beta Cos\theta, \quad (2)$$

where K is the Scherrer's constant, λ is the wavelength of the X-rays incident on the target with a value of (1.54056 Å), β is the full-width at half maximum (FWHM) in radians and θ is the Bragg angle.

The resulting values for the crystallite size are shown in the Table 2. The maximum value of the crystals size is 12 nm belongs to the CZTS1 sample, and we can conclude that the increase in the Na-doping ratio affects the crystallinity of the grown films. It is possible to summarize what happens to metal ions when Na is introduced into the CZTS host network. Lattice distortion occurs due to the difference in the diameter of the ions and the arrangement of the valence electron, and thus the results show that the distortion in the lattice of the samples was small [15].

Table 2. Structural parameters of the XRD results of Na-doped CZTS thin films at different doping ratios.

Sample	2θ (deg.) (112)	d (Å)	FWHM (deg.) (112)	D (nm)	Lattice constants (Å)		c/2a	Unit cell volume (Å^3)
					a = b	c		
CZTS1	28.53	3.129	0.6829	12.00	5.432	10.798	0.994	318.613
CZTS2	28.61	3.114	0.7064	11.61	5.431	10.862	1.000	320.383
CZTS3	28.80	3.107	1.0125	8.10	5.440	10.962	1.008	324.405
CZTS4	28.85	3.107	1.2951	6.33	5.408	10.863	1.004	317.704
CZTS5	28.90	3.112	1.2951	6.33	5.407	10.950	1.013	320.130
CZTS6	28.95	3.112	1.3000	6.31	5.410	10.994	1.016	321.773

Raman spectroscopy analysis

Raman spectroscopy is widely used to determine the presence of secondary phases in materials. In addition to the presence of other less intense peaks that occur in the locations indicated in Table 3, the Raman spectra revealed that the samples' main peak is located at ~ 337 cm^{-1}, which has been attributed to the kesterite CZTS, and this is in agreement with the conclusions of previous studies [11, 12].

Table 3. Results of Raman spectroscopy of Na-doped CZTS thin films at different doping ratios.

Sample	Peak center (cm^{-1})	Peak width (cm^{-1})	Intensity (arb. u.)
CZTS1	287	8.15	7.50
	237	8.04	69.65
	366	5.55	3.01
CZTS2	287	9.14	10.41
	337	9.09	69.52
	366	6.55	7.61
CZTS3	288	15.79	5.81
	337	10.07	60.3
	366	8.17	3.18
CZTS4	286	17.99	5.68
	337	12.11	59.15
CZTS5	289	26.6	7.32
	337	16.17	59.27
CZTS6	288	28.33	8.06
	336	24.30	57.01

Raman spectra of thin Na-doped CZTS films at different doping ratios are shown in Figure 2. Strain, phonon confinement, defects, and nonstoichiometry of the size distribution are just a few of the factors that might influence the position of the Raman peak [16]. The variation in Raman intensity is caused by the high frequency dielectric constant changing [17].

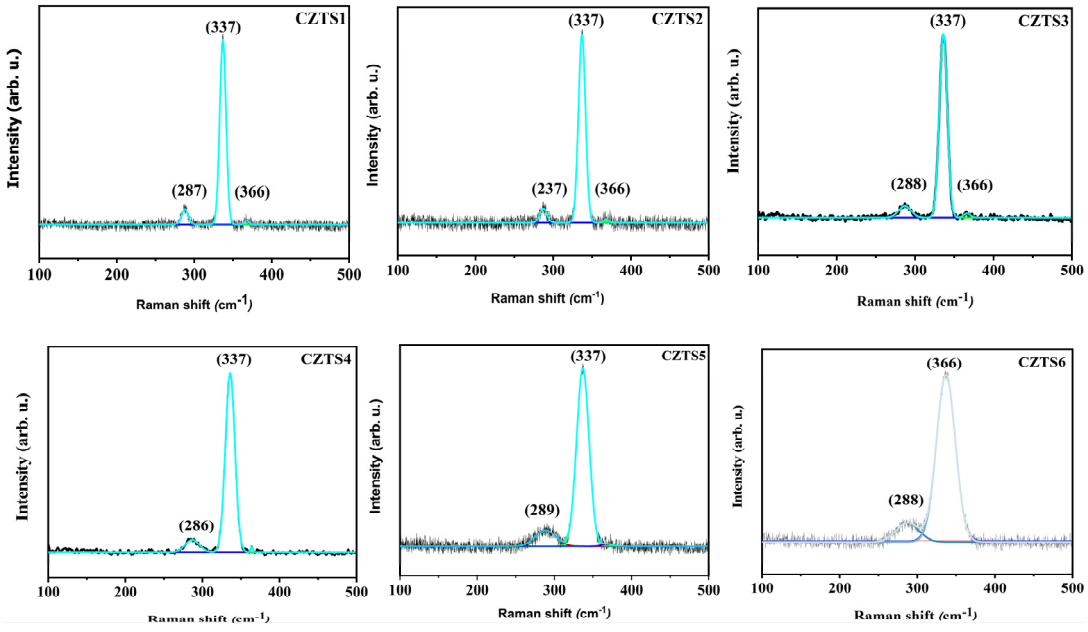

Figure 2. Raman spectra of Na-doped CZTS thin films at different doping ratios

Field Emission Scanning Electron Microscopy (FESEM) measurements

Figure 3 shows the FESEM micrographs (of 50 KX magnification) of the Na-doped CZTS thin films deposited in the present study. It can be seen that the surface structure of the films has a cauliflower-like shapes in the nano-scale with irregular particle size and distribution where the granular boundaries are clear. Also, there are a number of voids and cracks resulting from crystal defects and secondary growth on the surface. It can be concluded that a new layer starts to grow before the growth completion of the beneath layer.

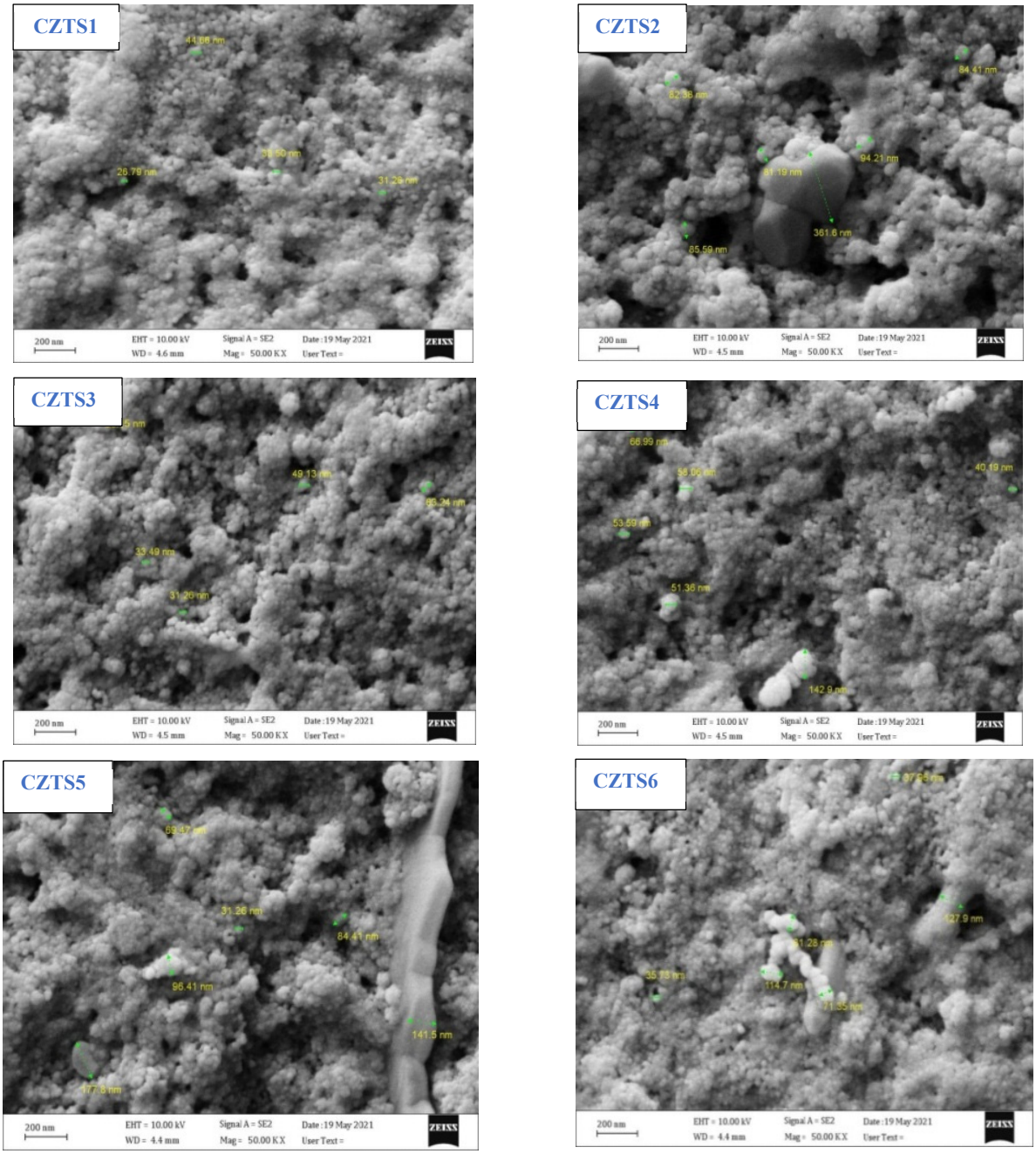

Figure 3. FESEM micro images of Na-doped CZTS thin films at different doping ratios

Optical measurements

The thin films optical absorption spectra were measured in the wavelength range of (300-900) nm using a UV-visible spectrophotometer. The investigation of the absorption coefficient based on photon energy is performed in the regions of high absorption to acquire thorough information about the energy band gaps of the films [18], and the absorption coefficient (α) is computed from the following equation [19]:

$$\alpha = 2.303A/t, \tag{4}$$

where (t) represents the thickness of the films and (A) is the absorbance.

The optical energy gap (E_g) of direct electronic transitions in films can be estimated from the absorbance spectrum using the equation:

$$\alpha h\upsilon = P(h\upsilon - E_g)^r, \quad (5)$$

where (P) is a constant dependent on the nature of the material, ($h\upsilon$) is the photon energy in (eV) units, E_g is the optical energy gap, and (r) is an exponential coefficient based on the transition nature (r =2 for allowed direct transition).

A graph is plotted between $(h\upsilon)^2$ and the incident photons energy ($h\upsilon$) (Tauc's plot) as represented in Figure 4. The energy gap value is estimated from intersection at the photon energy axis at the point $(\alpha h\upsilon)^2=0$. It can be noticed that the energy gap value of CZTS thin films decreases by increasing the Na-doping ratio. The energy gap values are 1.6, 1.58, 1.57, 1.53, 1.53 and 1.51 eV for the films CZTS1, CZTS2, CZTS3, CZTS4, CZTS5 and CZTS6 respectively.

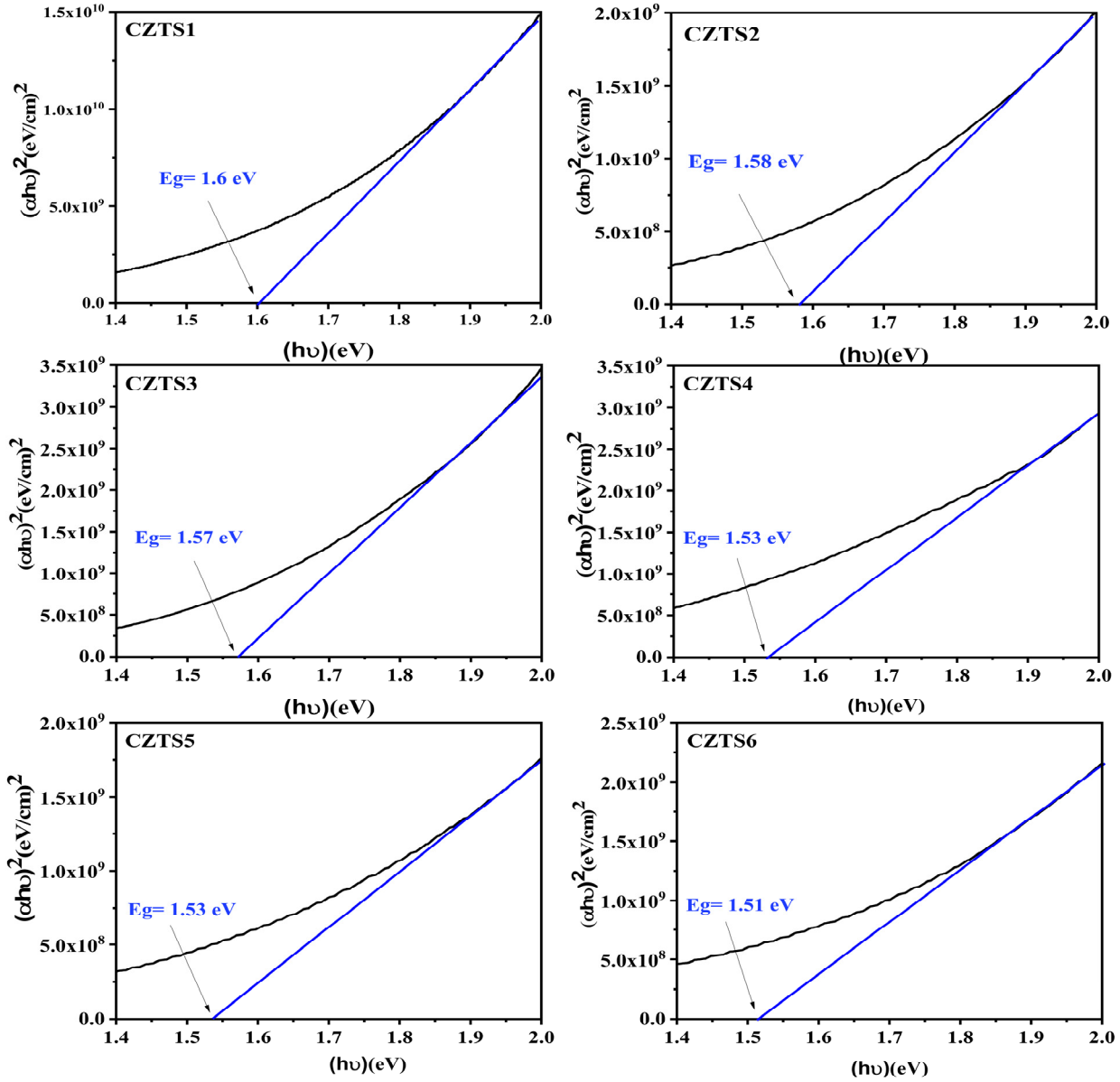

Figure 4. Tauc's plots of Na-doped CZTS thin films at different doping ratios.

The defects caused by Na are responsible for the reduction in band gap. When sodium is doped into a crystal, lattice distortion is induced leading to a change in the band gap. The substantial band gap decrease leads to the conclusion that the Na-doping model in the CZTS compound is an interstitial dopant, as it is the only model that combines band gap decrease and size reduction [20]. As a result, sodium acts to passivate defects in grain boundaries [21].

Electrical measurements

The Hall effect experiment was performed at room temperature to study electrical properties and specify the type, mobility and concentration of the majority charge carriers. According to Hall effect studies, the CZTS films have P-type conductivity, mobility of ~8.07 $cm^2/V.s$, and a maximum conductivity of ~1.81 $(\Omega.cm)^{-1}$, which corresponds to the films

CZTS6 as shown in Table 4. Figure 5 shows the variation of Hall conductivity with the Na doping ratio of CZTS thin films. Figure 6 shows the variation of the concentration and Hall mobility of the charge carriers as a function of Na doping ratio. From the two figures it can be concluded that the Na doping has improved the electrical properties of the deposited CZTS films.

Table 4. Results of the Hall effect experiment of Na-doped CZTS thin films at different doping ratios.

Sample	R_H (cm^3/C)	n (cm^{-3})×10^{18}	μ ($cm^2/V.s$)	ρ (Ω.cm)	σ $(\Omega.cm)^{-1}$
CZTS1	7.3724	0.8466	4.5521	1.6196	0.6174
CZTS2	7.0213	0.8889	5.4251	1. 2936	0.7730
CZTS3	6.1636	1.013	6.1331	1.0046	0.9954
CZTS4	5.5114	1.132	7.8556	0.7019	1.4247
CZTS5	4.4735	1.395	8.043	0.5563	1.7975
CZTS6	4.4627	1.399	8.0711	0.5528	1.8089

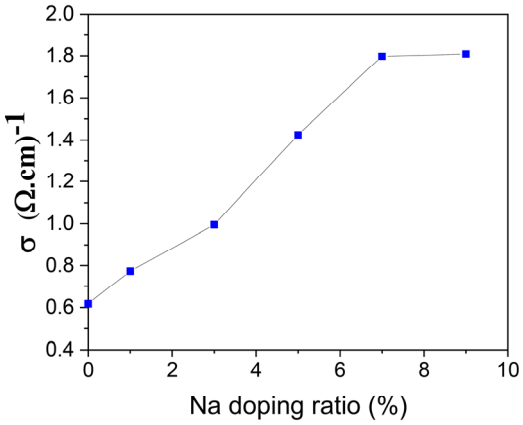

Figure 5. Variation of Hall conductivity of Na-doped CZTS thin films at different doping ratios.

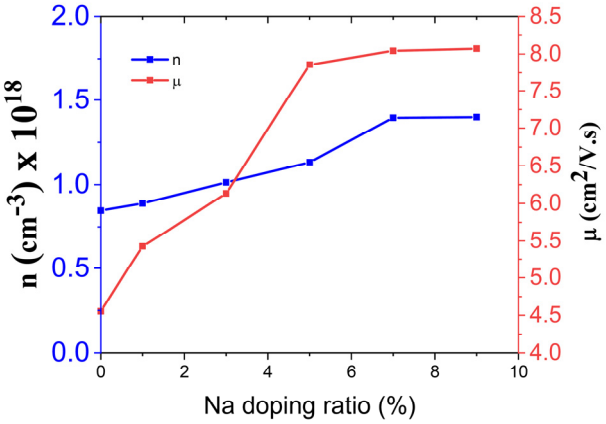

Figure 6. Variation of the concentration and Hall mobility of the charge carriers of Na-doped CZTS thin films at different doping ratios.

CONCLUSIONS

Na-doped CZTS thin films have been deposited successfully on glass substrates by chemical spray pyrolysis technique. The XRD experimental investigation of the films shows that they have kesterite tetragonal structure in the (112) favored direction. The crystallite size of all films was estimated using Scherrer's method, and it was found that the crystallite size decreases as the doping ratio increases. With increasing the Na volumetric doping ratio from 1 to 9 %, the optical band gap value decreases from 1.6 to 1.51 eV. Raman spectra of the films revealed a strong peak at ~ 337 cm^{-1} indicating the formation of the kesterite phase. On the other hand, all other observed low intensity peaks belong to the same phase confirming the absence of secondary phases. The FESEM surface morphology of the prepared Na-doped CZTS films was found to have cauliflower-like shapes in the nano-scale, with irregular particle size and distribution. Hall effect experiment on Na-doped CZTS films revealed that they have a P-type electrical conductivity with a low concentration of free holes. This test shows that the Na doping has improved the electrical properties of the deposited CZTS films.

ORCID IDs

Noura J. Mahdi, https://orcid.org/0000-0002-1219-0572; **Nabeel A. Bakr,** https://orcid.org/0000-0002-8819-5847

REFERENCES

[1] A. Polman, M. Knight, E.C. Garnett, B. Ehrler, and W.C. Sinke, "Photovoltaic materials: Present efficiencies and future challenges," Science, **352**(6283), aad4424 (2016). https://doi.org/10.1126/science.aad4424

[2] P. Jackson, R. Wuerz, D. Hariskos, E. Lotter, W. Witte, and M. Powalla, "Effects of heavy alkali elements in Cu(In,Ga)Se_2 solar cells with efficiencies up to 22.6%", Phys. Status Solidi, **10**(8), 583 (2016). https://doi.org/10.1002/pssr.201600199

[3] M.M.I. Sapeli, M.T. Ferdaous, S.A. Shahahmadi, K. Sopian, P. Chelvanathan, and N. Amin, "Effects of Cr doping in the structural and optoelectronic properties of Cu2ZnSnS4 (CZTS) thin film by magnetron co-sputtering", Materials Letters, **221**, 22 (2018). https://doi.org/10.1016/j.matlet.2018.03.056

[4] K.I. Nakazawa, "Electrical and optical properties of stannite-type quaternary semiconductor thin films", Japanese Journal of Applied Physics, **27**(11), 2094 (1988). https://doi.org/10.1143/JJAP.27.2094

[5] H. Katagiri, K. Jimbo, W.S. Maw, K. Oishi, M. Yamazaki, H. Araki, and A. Takeuchi, "Development of CZTS-based thin film solar cells", Thin Solid Films, **517**(7), 2455 (2009). https://doi.org/10.1016/j.tsf.2008.11.002

[6] M. Buffiere, DS. Dhawale, and F. El-Mellouhi, "Chalcogenide materials and derivatives for photovoltaic applications", Energy Technology, **7**(11), 1900819 (2019). https://doi.org/10.1002/ente.201900819

[7] S. Giraldo, Z. Jehl, M. Placidi, V. Izquierdo-Roca, A. Pérez- Rodríguez, and E. Saucedo, "Progress and perspectives of thin film kesterite photovoltaic technology: a critical review", Advanced Materials, **31**(16), 1806692 (2019). https://doi.org/10.1002/adma.201806692
[8] P.S. Patil, "Versatility of chemical spray pyrolysis technique", Mater. Chem. Phys. **59**(3), 185 (1999). https://doi.org/10.1016/S0254-0584(99)00049-8
[9] N. Nakayama, and K. Ito, "Sprayed films of stannite Cu_2ZnSnS_4", Applied Surface Science, **92**, 171 (1996). https://doi.org/10.1016/0169-4332(95)00225-1
[10] Z. Laghfour, S. Aazou, M. Taibi, G. Schmerber, A. Ulyashin, A. Dinia, and Z. Sekkat, "Sodium doping mechanism on sol-gel processed kesterite Cu_2ZnSnS_4 thin films", Superlattices and Microstructures, **120**, 747 (2018). https://doi.org/10.1016/j.spmi.2018.05.018
[11] Z. Tong, F. Liu, L. Jiang, and Y. Lai, "Improving the crystallization and carrier recombination of Cu_2ZnSnS_4 thin film deposited on Mo-coated soda-lime glass by extra sodium doping through solution process". Materials Letters, **254**, 50 (2019). https://doi.org/10.1016/j.matlet.2019.07.014
[12] M. Marzougi, M.B. Rabeh, and M. Kanzari, "Effect of Na Doping on Structural and Optical Properties in Cu_2ZnSnS_4 Thin Films Synthesized by Thermal Evaporation Method", Thin Solid Films, **672**, 41 (2019). https://doi.org/10.1016/j.tsf.2018.12.046
[13] C. Kittel, *Introduction to Solid State Physics*, (John Wiley and Sons Inc. 8th Edition, (2005).
[14] B.D. Cullity, *Elements of X-ray Diffraction*, (Addison-Wesley publishing company, 1956).
[15] E.M. Mkawi, "Kesterite Cu_2ZnSnS_4 Thin Films Synthesized Utilizing Electrodeposition: Influence of Metal Doping on the Properties", International Journal of Energy Research, **45**(2), 1908 (2021). https://doi.org/10.1002/er.5873
[16] N.A. Bakr, S.A. Salman, and S.A. Hameed, "Deposition and Characterization of Cu_2ZnSnS_4 Thin Films for Solar Cell Applications", International Journal of Applied Engineering Research, **13**(6), 3379 (2018). https://www.ripublication.com/ijaer18/ijaerv13n6_32.pdf
[17] D. Porezag, and M.R. Pederson, "Infrared Intensities and Raman-scattering Activities within Density-Functional Theory", Physical Review B, **54**(11), 7830 (1996). https://doi.org/10.1103/PhysRevB.54.7830
[18] N.A. Bakr, Z.T. Khodair, and S.M. Abdul Hassan, "Effect of Substrate Temperature on Structural and Optical Properties of Cu_2ZnSnS_4 (CZTS) Films Prepared by Chemical Spray Pyrolysis Method", Research Journal of Chemical Sciences, **5**(10), 51 (2014). http://surl.li/crxgq
[19] F. Zheng, X. Wen, T. Bu, S. Chen, J. Yang, W. Chen, F. Huang, and B. Jia, "Slow Response of Carries Dynamics in Perovskite Interface upon illumination", ACS Applied Materials and Interfaces, **10**(37), 31452 (2018). https://doi.org/10.1021/acsami.8b13932
[20] Z.K. Yuan, S. Chen, Y. Xie, J.S. Park, H. Xiang, X.G. Gong, and S.H. Wei, "Na-Diffusion Enhanced p-type Conductivity in Cu(In,Ga)Se_2: A New Mechanism for Efficient Doping in Semiconductors", Advanced Energy Materials, **6**(24), 1601191 (2016). https://doi.org/10.1002/aenm.201601191
[21] C.Y. Liu, Z.M. Li, H.Y. Gu, S.Y. Chen, H. Xiang, and X.-G. Gong, "Sodium Passivation of the Grain Boundaries in $CuInSe_2$ and Cu_2ZnSnS_4 for High-Efficiency Solar Cells", Advanced Energy Mater, **7**(8), 1601457 (2017). https://doi.org/10.1002/aenm.201601457

ВПЛИВ ЛЕГУВАННЯ Na НА ДЕЯКІ ФІЗИЧНІ ВЛАСТИВОСТІ ТОНКІХ ПЛІВОК CZTS З ХІМІЧНИМ НАПИЛЕННЯМ

Ноура Дж. Махди, Набіль А. Бакр
Факультет фізики, Науковий коледж, Університет Діяла, Діяла, Ірак

У цій роботі тонкі плівки сульфіду міді-цинку-олова (CZTS), леговані натрієм, отримують шляхом нанесення їх на скляні підкладки при температурі (400±10) °C і товщині (350±10) нм за допомогою хімічного розпилювального піролізу (CSP). техніка. Як джерело використовували 0,02 М дигідрату хлориду міді ($CuCl_2$,$2H_2O$), 0,01 М хлориду цинку ($ZnCl_2$), 0,01 М дигідрату хлориду олова ($SnCl_2$,$2H_2O$), 0,16 М тіосечовини ($SC(NH_2)_2$). іони міді, цинку, олова та сірки відповідно. Як джерело легуючої домішки використовувався хлорид натрію (NaCl) у різних об'ємних співвідношеннях (1, 3, 5, 7 та 9) %. Розчин напилюють на скляні підкладки. Для дослідження структурних, оптичних та електричних властивостей отриманих плівок використовувалися методи XRD-дифракції, рамановської спектроскопії, FESEM, UV-Vis-NIR та методу ефекту Холла. Результати дифракції XRD показали, що всі плівки є полікристалічними, з тетрагональною структурою та переважною орієнтацією вздовж площини (112). Розмір кристалітів усіх плівок було оцінено за допомогою методу Шеррера, і було виявлено, що розмір кристалітів зменшується зі збільшенням коефіцієнта легування. Результати FESEM показали існування наночастинок у формі цвітної капусти. Показано, що ширина забороненої зони оптичної енергії становить від 1,6 до 1,51 еВ з високим коефіцієнтом поглинання (α ≥104 см-1) у видимій області спектра. Вимірювання Холла показали, що провідність тонких плівок CZTS з різними коефіцієнтами легування Na має електропровідність p-типу, і вона зростає зі збільшенням коефіцієнта легування Na.

Ключові слова: тонкі плівки CZTS, легування натрієм, структурні властивості, оптичні властивості, ефект Холла.

East European Journal of Physics. **3.** 91-96 (2022)
DOI:10.26565/2312-4334-2022-3-12 ISSN 2312-4334

СТРУКТУРНІ, ЕЛЕКТРИЧНІ І ОПТИЧНІ ВЛАСТИВОСТІ ПЛІВОК ГРАФІТУ НАРИСОВАНИХ ОЛІВЦЯМИ РІЗНОЇ ТВЕРДОСТІ[†]

Сергій І. Курищук[a,*], Тарас Т. Ковалюк[a,b,‡], Іван П. Козярський[a,#], Михайло М. Солован[a,##]

[a]*Чернівецький національний університет імені Юрія Федьковича*
вул. Коцюбинського 2, 58012 Чернівці, Україна
[b]*Карловий університет, факультет математики та фізики*
Ке Карлову 5, 121 16 Прага 2, Чехія
**Corresponding Author: kuryshchuk.serhii@chnu.edu.ua*
[‡]E-mail: t.kovaliuk@mag.mff.cuni.cz, [#]E-mail: i.koziarskyi@chnu.edu.ua [##]E-mail: m.solovan@chnu.edu.ua
Received August 15, 2022; revised August 17, 2022; accepted August 20, 2022

В роботі представлено результати дослідження структурних, оптичних та електричних властивостей тонких плівок графіту в залежності від твердості стержнів (2H, H, HB, B та 2B) отриманих методом "Олівець-на-напівпровіднику". Такі дослідження мають велике значення для подальшої розробки високоефективних приладів на основі гетеропереходів для електроніки і оптоелектроніки. За допомогою скануючого електронного мікроскопа було одержано типові зображення поверхні утворені відбитими електронами (BSE) і показано при трьох збільшеннях (100x, 500x і 1000x). Оскільки стержні досліджуваних олівців складаються з сумішей глини та графіту було проведено більш детальний аналіз елементів з яких складаються стержні. EDS аналіз показав, що основними складниками досліджуваних стержнів є очищений графітовий порошок, а також O, Al і Si що входять до складу каоліну формула якого $H_4Al_2Si_2O_9$, або $Al_2O_3 \cdot 2SiO_2 \cdot 2H_2O$ - головна складова частина звичайної глини. Також було визначено елементний склад мікрооб'єму досліджуваних зразків. Не зважаючи на похибку, яка виникає при визначенні складу C і O (~ 12%) можна стверджувати, що все ж таки зберігається закономірність між вмістом графіту і твердістю олівця. Тобто чим більший вміст графіту — тим м'якший стержень. Вимірювання товщини плівок графіту проведено з використанням інтерферометра МИИ-4 за стандартною методикою. Середня товщина всіх досліджуваних плівок становила ~ 150 нм, оскільки товщина плівок отриманих таким методом в основному визначається шороховатістю поверхні соляної підкладки. Нарисовані плівки графіту володіють вищим питомим опором ніж об'ємні зразки (стержні олівців) з яких вони були виготовлені. Опір плівок зростає при зростанні твердості олівців, що обумовлено зростанням кількості домішки глини в графіті, яка є діелектриком. Встановлено, що зростання твердості олівця призводить до зростання пропускання.
Ключові слова: «олівець-на-напівпровіднику», графіт, провідність, пропускання, тонкі плівки.
PACS: 68.55.Ln, 71.55.Ak, 68.37.Hk, 68.37.−d, 78.20.Ci, 72.20. −i

У графіту є багато переваг в порівнянні з традиційними металами. Графіт володіє стійкістю до термічної дії, завдяки міцним зв'язкам атомів вуглецю, тому бар'єри Шотткі на основі плівок графіту зберігають випрямляючі властивості при достатньо високих температурах. Крім цього, графіт можна легувати акцепторними домішками, що призводить до зниження рівня Фермі та збільшує висоту бар'єру Шотткі, тоді як в металах робота виходу завжди незмінна та не може бути змінена легуванням [1,2].

Методи виготовлення тонких плівок графіту представляють великий науковий та практичний інтерес, обумовлений їх унікальними фізичними властивостями, високою електричною провідністю, хорошою прозорістю, високими механічними властивостями, високою рухливістю електронів при температурі +20˚C [3]. Технологія графену (одноатомного шару вуглецю), який представляє собою двовимірний напівпровідник [4,5] отримала широке практичне застосування.

Недавно тонкі плівки графіту було використано для виготовлення новітніх, екологічно чистих і дешевих наноструктурованих тонкоплівкових електронних приладів нового покоління [6-9]. Крім того, нещодавні дослідження поверхні та структурних властивостей нарисованих графітових тонких плівок показують, що вони складаються з розупорядкованих зв'язаних графітових мікро- та наночасток, а також з нанопластівців моно- або декілька шарового графену [10,11]. Тому такі тонкі плівки являються двох-вимірними наноструктурованими об'єктами.

Отже, метою роботи є дослідження впливу на структурні, електричні і оптичні властивості тонких плівок графіту твердості стержнів (2H, H, HB, B та 2B), обраних для створення даних плівок.

ЕКСПЕРИМЕНТАЛЬНА ЧАСТИНА

Перед початком нанесення плівок графіту, (слідуючи за технологією – «олівець-на-напівпровіднику» [12-17]), одну з поверхонь свіжосколеної монокристалічної соляної підкладки (NaCl) механічно шліфували до шорсткості R_a=0,2 мкм, R_z=0,23 мкм і R_{max}=1,1 мкм. Якісна графітова плівка малювалася на попередньо

[†] ***Cite as:*** S.I. Kuryshchuk, T.T. Kovaliuk, I.P. Koziarskyi, and M.M. Solovan, East Eur. J. Phys. **3**, 91 (2022), (in Ukrainian). https://doi.org/10.26565/2312-4334-2022-3-12

підготовленій поверхні соляної підкладки за допомогою чистого графітового стержня 1 мм у діаметрі та олівців з різною твердістю 2H, H, HB, B та 2B при постійній силі притиснення в 1 Н. Далі зразки обережно розміщуються на поверхні дистильованої води плівкою графіту вверх. Соляна підкладка повністю розчиняється у дистильованій воді. Варто відмітити, що таким чином отримується нарисована графітова плівка, яка не зв'язана з підкладкою, на якій вона була нарисована. Зв'язок між наночастками графіту, які формують нарисовану графітову тонку плівку, є достатнім аби компенсувати силу поверхневого натягу води. Отже, немає необхідності у використанні додаткового захисного шару на плівці для підвищення її механічної міцності. Плаваючу намальовану плівку графіту можна легко перенести на будь-яку іншу підкладку з гладкою або наноструктурованою поверхнею. У нашому випадку плівки графіту переносили на підкладки ситалу розмірами 5×10×0,5 мм для дослідження електричних властивостей та на скляні підкладки розмірами 18с18×0,5 мм для дослідження оптичних властивостей. Після перенесення плівки висушували у потоці гарячого повітря 80°С для видалення залишків води та формувався якісний оптичний контакт з гладкою поверхнею підкладки.

Дослідження оптичних властивостей тонких плівок графіту проводились за допомогою спектрофотометра СФ-2000, в області довжин хвиль 200-1200 нм.

Дослідження морфології поверхні і визначення елементного складу олівців різної твердості (2H, H, HB, B та 2B) було проведено за допомогою скануючого електронного мікроскопа (MIRA3 FEG, Tescan) оснащеного детектором відбитих електронів (BSE) і енергодисперсним рентгенівським детектором (EDX). Для забезпечення електричного контакту з предметним столиком і для фіксації стержні олівців (2H, H, HB, B та 2B) були відламані і зафіксовані за допомогою провідного вуглецевого скотчу. Відносна похибка при вимірюванні атомних часток хімічних елементі, які входять до складу не перевищує 2% для Al і Si та не більше 12% для C і O.

РЕЗУЛЬТАТИ ТА ЇХ ОБГОВОРЕННЯ

Структурні властивості тонких плівок CuO

З допомогою скануючого електронного мікроскопа було одержано типові зображення поверхні утворені відбитими електронами (BSE) (рис. 1) які показано при трьох збільшеннях (100x, 500x і 1000x).

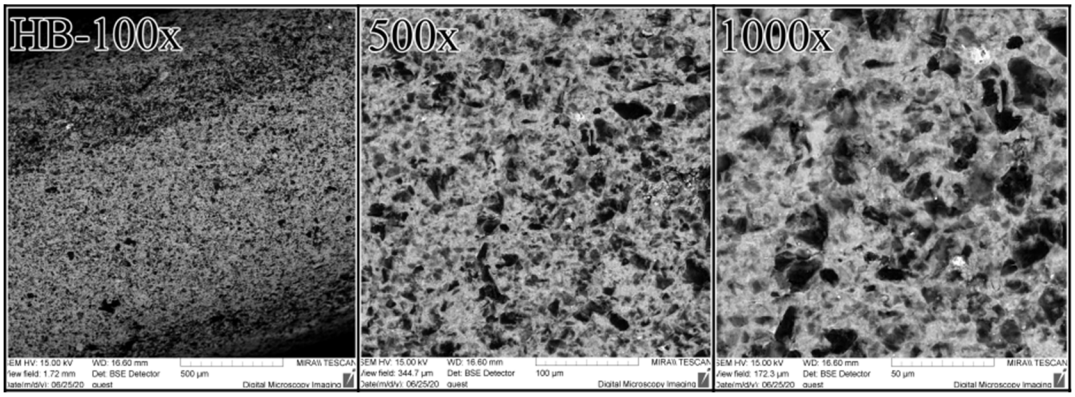

Рисунок 1. Зображення поверхні утворені відбитими електронами (BSE) при різному збільшенні (100x, 500x і 1000x) для олівця твердістю HB.

Контраст зображення утвореного відбитими електрони несе інформацію про розподіл електронної густини (області, збагачені елементом з великим атомним номером виглядають яскравіше: темна область – графіт, яскраві області O, Al, Si). Тому відбиті електрони, які генеруються одночасно з вторинними, окрім інформації про морфологію поверхні містять додаткову інформацію і про склад зразка.

На рис. 2 представлено зображення поверхні утворені відбитими електронами (BSE) для олівців різної твердості (2H, H, 2B, B та HB) при збільшенні в 1000x, а також розподіл елементів, які входять до складу стержнів для прикладу їх показано для олівця твердістю HB.

З рис. 2 також можна зробити висновок, що зразок 2B володіє найбільшим вмістом графіту (підтверджено елементним аналізом табл. 1) утворений контраст зображення є темнішим в порівнянні з іншими зразками, що свідчить про збагачення дослідженої області елементом з малим атомним номером.

Таблиця 1. Елементний склад зразків

Назва	Атомна частка хімічного елемента, який входять до складу зразка, %			
	C	Al	Si	O
2H	44	5.39	6.73	43.88
H	53.97	4.67	6.3	35.06
HB	54.47	5.83	6.97	32.74
B	57.09	4.85	6.41	31.65
2B	62.68	3.61	4.76	28.96

Опромінення зразків пучком електронів призвело не тільки до утворення вторинних і відбитих електронів, а також викликало появу характеристичного Х-хвильового випромінювання (типові залежності представлено на рис. 3 для олівця твердістю НВ).

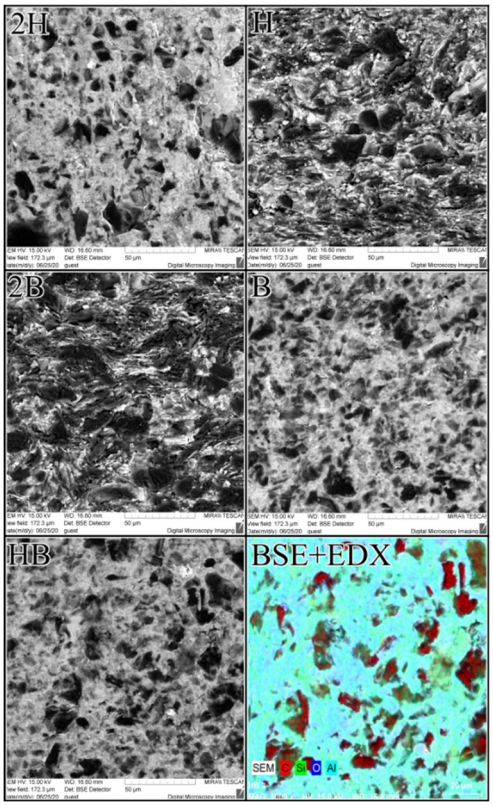

Рисунок 2. Зображення поверхні утворені відбитими електронами (BSE) для 2H, H, 2B, B та HB при збільшенні в 1000х.

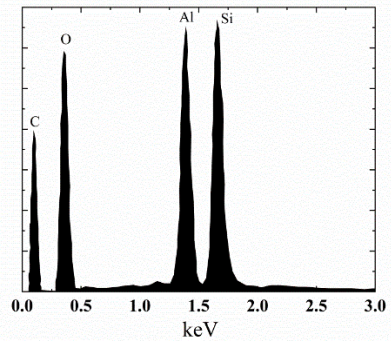

Рисунок 3. EDS-спектр стержня олівця з твердістю НВ

Оскільки стержні досліджуваних олівців складається з сумішей глини та графіту було вирішено провести більш детальний аналіз елементів з яких складаються стержні. EDS аналіз показав, що основними складниками досліджуваних стержнів є очищений графітовий порошок, а також O, Al і Si що входять до складу каоліну формула якого $H_4Al_2Si_2O_9$, або $Al_2O_3 \cdot 2SiO_2 \cdot 2H_2O$ - головна складова частина звичайної глини.

Аналіз характеристичного *X*-хвильового випромінювання дозволив визначити елементний склад мікрооб'єму досліджуваних зразків (для прикладу частина даних представлена в табл. 1).

Не зважаючи на похибку, яка виникає при визначенні складу C і O (~ 12%) можна стверджувати, що все ж таки зберігається закономірність між вмістом графіту і твердістю олівця. Тобто чим більший вміст графіту – тим м'якший стержень, що в свою чергу буде впливати на фізичні властивості плівок, як показано нижче.

На рис. 4. показано розподіл елементів (C, Si, O, Al), які входять до складу олівця з твердістю НВ.

Питомий опір в тонких плівках (коли товщина зразка набагато менша від відстані між контактами) характеризується "питомим опором на квадрат", (R_S). У цьому випадку питомий опір не залежить від лінійних розмірів зразка якщо він має форму прямокутника, а тільки від відношення (довжини до ширини). Опір частини тонкої плівки прямокутного перерізу можна задати виразом

$$R = \rho l / db \qquad (1)$$

Якщо $l = b$, тоді

$$R = \rho l / db = R_S \tag{2}$$

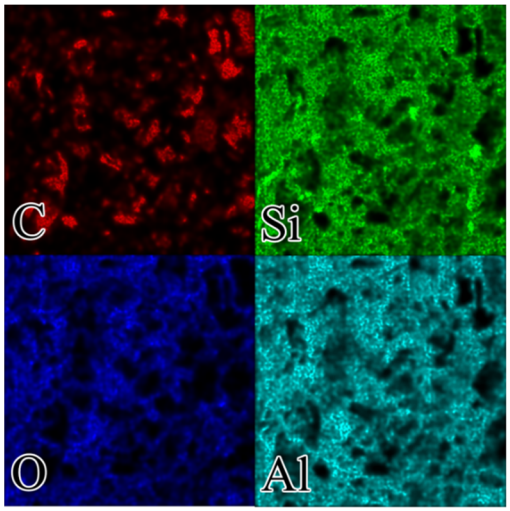

Рисунок 4. EDX елементний розподіл (C, Si, O, Al).

тому опір R_s одного квадрату тонкої плівки залежить не від розмірів квадрату, а лише від питомого опору і товщини. Величина R_s називається поверхневим опором плівки і виражається в омах на квадрат [17]. Ця величина має велике значення і широко використовується для порівняння плівок, зокрема плівок з одного матеріалу, осаджених при ідентичних умовах.

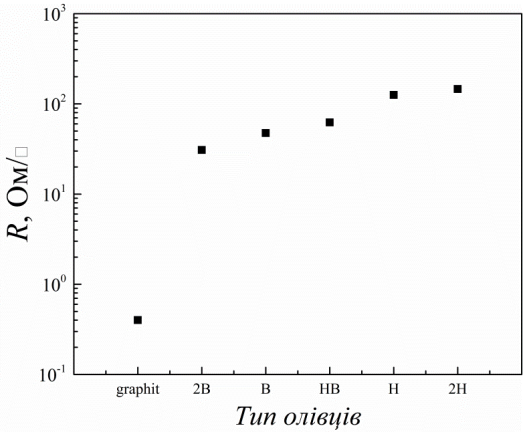

Рисунок 5. Поверхневий опір плівок графіту виготовлених за допомогою різних олівців.

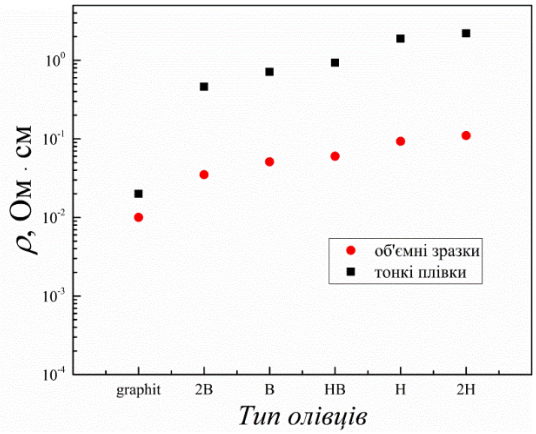

Рисунок 6. Залежність питомого опору плівок графіту від твердості олівців

На рисунку 5, приведено виміряні значення поверхневого опору чотирьохзондовим методом для плівок графіту виготовлених олівцями різної твердості.

З рисунка 5 видно, що опір плівок зростає при зростанні твердості олівців, що пов'язано із зростанням кількості домішки глини в графіті, яка є діелектриком. Відомо, що у полікристалічних вуглецевих матеріалах загальна провідність визначається двома складовими: електропровідністю кристалітів (металевою за своїм типом) і провідністю аморфного вуглецю-напівпровідника і тому вона залежить від вмісту домішки діелектрика.

Якщо відома товщина досліджуваних тонких плівок, то їх питомий опір легко визначити з виразу:

$$\rho = dR_s . \tag{3}$$

де d- товщина тонкої плівки.

Вимірювання товщини плівок графіту проводилося з використанням інтерферометра МИИ-4 за стандартною методикою. Середня товщина всіх досліджуваних плівок становила ~ 150 нм, оскільки товщина плівок отриманих таким методом в основному визначається шороховатістю поверхні соляної підкладки.

На рисунку 6 приведено значення питомого опору всіх досліджуваних тонких плівок розрахованого за допомогою співвідношення (3) та значення питомого опору стержнів олівців за допомогою, яких були виготовлені досліджувані тонкі плівки.

З рисунка 6 видно, що нарисовані плівки графіту володіють вищим питомим опором ніж об'ємні зразки (стержні олівців), з яких вони були виготовлені, що обумовлено розмірними ефектами. Як тільки товщина плівки стає співмірною по величині з довжиною вільного

пробігу носіїв заряду, межі плівки накладають геометричне обмеження на рух електронів провідності і, отже, на їх ефективну величину довжини вільного пробігу. Фізичні ефекти, що виникають із-за такого геометричного обмеження довжини вільного пробігу, називають ефектами «довжини вільного пробігу» або «розмірними» ефектами.

У провідність плівки створюють вклад тільки ті електрони, які рухаються майже паралельно поверхні, внаслідок чого довжина їх вільного пробігу залишається величиною порядку довжини пробігу в об'ємному матеріалі. Електрони провідності розсіюються в плівці не тільки її поверхнями і граткою, але і домішками, а також багатьма структурними дефектами, що збереглися.

Границі зерен у графіті та графітоподібних матеріалах сильно впливають на фізичні властивості матеріалу. Електричне поле зарядів на межі зерен утворює енергетичні бар'єри E_b для руху носіїв заряду. Між цими кристалітами створюються області певною товщиною δ, які є збіднені на основні носії заряду [19,20].

Сумарний струм через полікристалічний матеріал складається як з провідності зерен, так і механізмом переходу носіїв заряду з одного зерна в інше, тобто провідністю границь зерен. Провідність зерен багато більша за провідність границь зерен і в першу чергу залежить від питомого опору матеріалу. Оскільки в нас суміш провідного і діелектричного матеріалу, то провідність зерен визначається $\sigma=en\mu$. Через це при дослідженні руху носіїв заряду у полікристалічних тонких плівках в першу чергу треба розглядати провідність областей між кристалітами. Провідність полікристалічних тонких плівок σ з врахуванням енергетичних бар'єрів на межі зерен, описується виразом [21]:

$$\sigma = \frac{Le^2 n}{\sqrt{2\pi m^* kT}} \exp\left(-\frac{eV_b}{kT}\right), \tag{4}$$

де L – середній розмір кристалітів; m^* - ефективна маса носіїв заряду; n – концентрація носіїв заряду всередині кристаліта; $eV_b = E_b$ – висота бар'єра на границі зерен.

На рис. 7 зображено спектри пропускання тонких плівок графіту для п'ятьох графітових плівок, які були виготовлені олівцями різної твердості.

З рисунка бачимо, що зростання твердості олівця призводить до зростання пропускання плівок. Це може бути обумовлено збільшенням вмісту оксидних матеріалів в нарисованих плівках (які мають велику ширину забороненої зони, а отже і більше пропускання), внаслідок зростання кількості домішки глини в графіті більшої твердості.

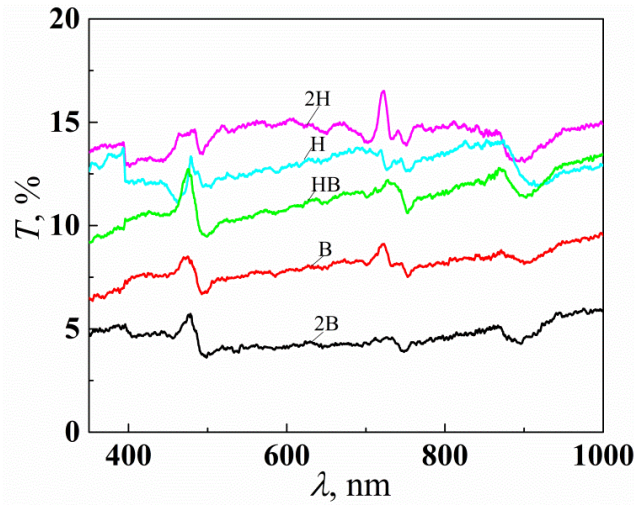

Рисунок 7. Спектри пропускання тонких плівок графіту, виготовлених різними олівцями

ВИСНОВКИ

1. Отримано тонкі плівки графіту методом "Олівець-на-напівпровіднику" та досліджено їх структурні, оптичні та електричні властивості.
2. Показано, що нарисовані плівки графіту володіють вищим питомим опором ніж об'ємні зразки (стержні олівців) з, яких вони були виготовлені, що обумовлено розмірними ефектами.
3. Встановлено, що опір плівок зростає при зростанні твердості використаних олівців, що обумовлено зростанням кількості домішки глини в графіті, яка є діелектриком.
4. Встановлено, що зростання твердості олівця призводить до зростання пропускання. Це може бути обумовлено збільшенням вмісту оксидних матеріалів в нарисованих плівках (які мають велику ширину забороненої зони, а отже і більше пропускання), внаслідок зростання кількості домішки глини в графіті більшої твердості.

ORCID IDs
Serhii I. Kuryshchuk, https://orcid.org/0000-0002-5937-2701; **Taras T. Kovalyuk,** https://orcid.org/0000-0002-7712-6758
Ivan P. Koziarskyi, https://orcid.org/0000-0002-4984-4349; **Mykhailo M. Solovan,** https://orcid.org/0000-0002-1077-5702

REFERENCES

[1] V.V. Brus, M.A. Gluba, X. Zhang, K. Hinrichs, J. Rappich, and N.H. Nickel, Solar energy, **107**, 74 (2014), https://doi.org/10.1016/j.solener.2014.05.021
[2] H. Parkhomenko, M. Solovan, V.V. Brus, E. Maystruk, and P.D. Maryanchuk, Optical Engineering, **57**(1), 017116 (2018), https://doi.org/10.1117/1.OE.57.1.017116
[3] K. Kostarelos, and K.S. Novoselov, Nature nanotechnology, **9**(10), 744 (2014), https://doi.org/10.1038/nnano.2014.224
[4] A.C. Neto, F. Guinea, N.M. Peres, K.S. Novoselov, and A.K. Geim, Reviews of modern physics, **81**(1), 109 (2009), https://doi.org/10.1103/RevModPhys.81.109
[5] M.D. Stoller, S. Park, Y. Zhu, J. An, and R.S, Ruoff, Nano letters, **8**(10), 3498 (2008), https://doi.org/10.1021/nl802558y
[6] M.M. Solovan, H.P. Parkhomenko, and P.D. Marianchuk, Journal of Physical Studies, **23**(4), (2019), https://doi.org/10.30970/jps.23.4801
[7] D. Neumaier, S. Pindl, and M.C. Lemme, Nature Materials, **18**(6), 525 (2019), https://doi.org/10.1038/s41563-019-0359-7
[8] M. Jung, P. Rickhaus, S. Zihlmann, A. Eichler, P. Makk, C. Schönenberger, Nanoscale, **11**(10), 4355 (2019), https://doi.org/10.1039/C8NR09963D
[9] R. You, Y.Q. Liu, Y.L. Hao, D.D. Han, Y.L. Zhang, and Z. You, Advanced Materials, **32**(15), 1901981 (2020), https://doi.org/10.1002/adma.201901981
[10] Y. Miyasaka, A. Nakamura, and J. Temmyo, Japanese Journal of Applied Physics, **50**(4S), 04DH12 (2011), https://doi.org/10.1143/JJAP.50.04DH12
[11] M. Yankowitz, Q. Ma, P. Jarillo-Herrero, and B.J. LeRoy, Nature Reviews Physics, **1**(2), 112 (2019), https://doi.org/10.1038/s42254-018-0016-0
[12] V.V. Brus, O.L. Maslyanchuk, M.M. Solovan, P.D. Maryanchuk, I. Fodchuk, V.A. Gnatyuk, and T. Aoki, Scientific reports, **9**(1), 1 (2019), https://doi.org/10.1038/s41598-018-37637-w
[13] V.V. Brus, M. Gluba, J. Rappich, F. Lang, P.D. Maryanchuk, and N.H. Nickel, ACS applied materials & interfaces, **10**(5), 4737 (2018), https://doi.org/10.1021/acsami.7b17491
[14] M.N. Solovan, G.O. Andrushchak, A.I. Mostovyi, T.T. Kovaliuk, V.V. Brus, and P.D. Maryanchuk, Semiconductors, **52**(2), 236 (2018), https://doi.org/10.1134/S1063782618020185
[15] V.V. Brus, and P.D. Maryanchuk, Carbon, **78**, 613 (2014), https://doi.org/10.1016/j.carbon.2014.07.021
[16] V.V. Brus, P.D. Maryanchuk, M.I. Ilashchuk, J. Rappich, I.S. Babichuk, and Z.D. Kovalyuk, Solar Energy, **112**, 78 (2015), https://doi.org/10.1016/j.solener.2014.11.023
[17] V.V. Brus, and P.D. Maryanchuk, Applied Physics Letters, **104**(17), 173501 (2014), https://doi.org/10.1063/1.4872467
[18] K. Chopra, and S. Das, *Thin-film solar cells (Vol. 450)*, (Mir, Moscow, 1986).
[19] N.F. Mott, and E.A. Davis, *Electronic Processes in Non-Crystalline Materials*, (Oxford University Press, Oxford, New York, 2012).
[20] J.Y.W. Seto, Journal of Applied Physics, **46**, 5247 (1975). https://doi.org/10.1063/1.321593
[21] V.V. Brus, M.I. Ilashchuk, I.G. Orletskyi, M.M. Solovan, G.P. Parkhomenko, I.S. Babichuk, and P.D. Maryanchuk. Nanotechnology, **31**(50), 505706 (2020), https://doi.org/10.1088/1361-6528/abce55

STRUCTURAL, ELECTRICAL AND OPTICAL PROPERTIES OF GRAPHITE FILMS ARE DRAWN WITH PENCILS OF DIFFERENT HARDNESS

Serhii I. Kuryshchuk[a], Taras T. Kovaliuk[a,b], Ivan P. Koziarskyi[a], Mykhailo M. Solovan[a]
[a]*Yuriy Fedkovych Chernivtsi National University, st. Kotsyubyns'kogo 2, 58012, Chernivtsi, Ukraine*
[b]*Charles University in Prague, Faculty of Mathematics and Physics, Ke Karlovu 5, 121 16 Prague 2, Czech Republic*

The paper presents the results of studying the structural, optical and electrical properties of thin films of graphite depending on the hardness of the rods (2H, H, HB, B and 2B) obtained by the "Pencil-on-semiconductor" method. Such studies are of great importance for the further development of highly efficient devices based on heterojunctions for electronics and optoelectronics. Typical images of the surface formed by reflected electrons (BSE) were obtained using a scanning electron microscope and shown at three magnifications (100x, 500x and 1000x). Since the cores of the studied pencils consist of mixtures of clay and graphite, a more detailed analysis of the elements that make up the cores was conducted. EDS analysis showed that the main components of the studied rods are purified graphite powder, as well as O, Al and Si, which are part of kaolin whose formula is $H_4Al_2Si_2O_9$, or $Al_2O_3 \cdot 2SiO_2 \cdot 2H_2O$ - the main component of ordinary clay. The elemental composition of the microvolume of the studied samples was also determined. Regardless of the error that occurs when determining the composition of C and O (~ 12%), it can be argued that there is still a regularity between the graphite content and the hardness of the pencil. That is, the higher the graphite content, the softer the rod. The thickness of the graphite films was measured using the MII-4 interferometer according to the standard method. The average thickness of all investigated films was ~ 150 nm since the thickness of the films obtained by this method is mainly determined by the roughness of the surface of the salt substrate. Drawn graphite films have a higher resistivity than bulk samples (pencil rods) from which they were made. The resistance of the films increases with an increase in the hardness of pencils, due to an increase in the number of clay impurities in graphite, which is a dielectric. It was found that an increase in stick hardness leads to an increase in transmission.

Keywords: "Pencil-on-semiconductor", graphite, conductivity, transmission, thin films.

EAST EUROPEAN JOURNAL OF PHYSICS. **3.** 97-103 (2022)
DOI:10.26565/2312-4334-2022-3-13 ISSN 2312-4334

BIANCHI TYPE V TSALLIS HOLOGRAPHIC DARK ENERGY MODEL WITH HYBRID EXPANSION LAW[†]

Manash Pratim Das*, Chandra Rekha Mahanta
Department of Mathematics, Gauhati University, Guwahati (India)
**Corresponding Author: manashpratimdas22222@gmail.com, crmahanta@gauhati.ac.in*
Received July 25, 2022; revised August 23, 2022; accepted August 25, 2022

A number of recent cosmological observations have provided increasing evidence that currently the universe is undergoing a phase of accelerated expansion, the root cause of which is supposed to be due to an exotic component of the universe with large negative pressure, dubbed dark energy. Out of the various candidates of dark energy proposed in the literature, the holographic dark energy emerged from the Holographic Principle is drawing much attention in the research field. In this paper, we investigate a spatially homogeneous and anisotropic Bianchi Type V space-time filled with non-interacting Tsallis holographic dark energy (THDE) with Hubble horizon as the IR cutoff and pressureless cold dark matter within the framework of General Relativity. Exact solutions of the Einstein field equations are obtained by considering the average scale factor a to be a combination of a power law and an exponential law, the so called hybrid expansion law first proposed by Akarsu *et al*. (2014). We study the cosmological dynamics of various models for different values of the non-additive parameter δ that appeared in the Tsallis entropy and that for ξ that appeared in the exponential function of the hybrid expansion law. We find that our model exhibits present cosmological scenario.
Keywords: Tsallis Holographic Dark Energy, Bianchi Type V, Hybrid Expansion Law, Accelerated expansion
PACS: 98.80.jk, 04.20.jb

The powerful astrophysical observations such as Supernovae Type Ia [1-3], Cosmic Microwave Background [4, 5], Large Scale Structure [6]etc. strongly indicate that the present rate of cosmic expansion is accelerating. As till late 1990's it was believed that the expansion of the universe is decelerating, so the results from the above experiments made the cosmologists to think in a different way. The reason behind this mysterious acceleration is yet unknown, so universally it is accepted that the universe is dominated by a strange kind of energy fluid, dubbed dark energy, which occupies nearly 68.3% of the total content of the universe. Till then the cosmologists are trying to find the true nature of dark energy as well as the root cause of the observed cosmic acceleration. The simplest candidate which satisfies all the conditions for accelerating the expansion rate of the universe and which acts opposite to gravity is the cosmological constant Λ that Einstein introduced in his field equations. Theoretically, the cosmological constant is supposed to be $\Lambda = 8\pi G\rho_{vac}$. But the calculated value of ρ_{vac} is much larger than the value of Λ determined from observations, and therefore due to its non-evolving nature it faces the fine-tuning and cosmic coincidence problems and hence some alternative approaches have been adopted. Since then, a number of dark energy candidates have been considered in the literature to explain the late time acceleration of the universe. Among them quintessence [7], phantom [8], k-essence [9], tachyon [10], dilatonic ghost condensate model [11], Chaplygin gas models [12], braneworld models [13] etc. are the most studied candidates of dark energy.

Holographic dark energy model is another possible candidate which emerges from the famous holographic principle proposed to explain the thermodynamics of black hole physics. According to the holographic principle the number of degrees of freedom directly related to entropy of a physical system scales with the enclosing surface area of the system rather than with its volume [14]. Fischler and Susskind [15] later extended this principle to the cosmological setting with a new versionwhich states that the gravitational entropy within a closed surface should not be always larger than the particle entropy that passes through the past light-cone of that surface. Later several researchers proposed different IR cutoff which led to some new problems in physics. Tsallis and Cirto in 2013 put forwarded a new model of holographic dark energy known as Tsallis Holographic dark energy (THDE) model by using Tsallis generalized entropy, $S_\delta = \gamma A^\delta$, where γ is an unknown constant and δ is a non-additive parameter [16]. Thus, the energy density of the Tsallis holographic dark energy can be obtained as $\rho_{THDE} = DL^{2\delta-4}$, where D is an unknown parameter [17]. If the Hubble horizon is used as the IR cutoff i.e. $L = \frac{1}{H}$, then the energy density of the THDE is obtained as $\rho_{THDE} = DL^{-2\delta+4}$. In literature several researchers (Ghaffari*et al*. 2018 [18], Korunur 2019 [19], Sharma and Pradhan 2019 [20], Dubey *et al*. 2020 [21], Liu 2021 [22], Mohammadi *et al*. 2021 [23], Pandey *et al.* 2022 [24], Kumar *et al*; 2022 [25]). have studied different aspects of Tsallis Holographic dark energy.

In this paper, we study the spatially homogeneous and anisotropic Bianchi Type V space-time filled with non-interacting Tsallis holographic dark energy (THDE) and cold dark matter. The paper is organized as follows: in Sect. **"METRIC AND FIELD EQUATIONS"**, we derive the cosmic evolution equations from the Einstein field equations in the background of Bianchi Type V line element. We solve the field equations in Sect. **"COSMOLOGICAL SOLUTIONS OF THE FILED EQUATIONS"** by considering the hybrid expansion law proposed by Akarsu *et al* (2014) [26]. In

[†]***Cite as:*** M.P. Das, and C.R. Mahanta, East Eur. J. Phys. **3**, 97 (2022), https://doi.org/10.26565/2312-4334-2022-3-13

Sect. **"RESULTS AND DISCUSSION"** we study cosmological dynamics of our model for $\delta = 1$, $1 < \delta < 2$ and for $\delta = 2$. Finally, we conclude the paper in Sect. **"CONCLUSION"** with a brief discussion.

METRIC AND FIELD EQUATIONS

We consider the spatially homogeneous and anisotropic Bianchi Type V space-time characterized by the line element

$$ds^2 = -dt^2 + A^2dx^2 + e^{2mx}(B^2dy^2 + C^2dz^2) \tag{1}$$

where *A*, *B*, *C* are functions of cosmic time *t* only and *m* is a constant.

We assume that the universe is filled with cold dark matter and non-interacting Tsallis holographic dark energy (THDE) with energy-momentum tensors T_{ij} and $\bar{T}_{ij}$resepectively

$$T_{ij} = \rho_m u_i u_j \tag{2}$$

$$\bar{T}_{ij} = (\rho_{THDE} + p_{THDE})u_i u_j + g_{ij}p_{THDE} \tag{3}$$

where ρ_{THDE} and p_{THDE} are the energy density and the pressure of the THDE respectively.

Einstein's field equations in natural units ($8\pi G = 1, c = 1$) are given by

$$R_{ij} - \frac{1}{2}g_{ij}R = -(T_{ij} + \bar{T}_{ij}) \tag{4}$$

where R_{ij} is the Ricci tensor, $R$is the Ricci scalar and$g_{ij}$is the metric tensor.

The THDE density with Hubble horizon as the IR cutoff is

$$\rho_{THDE} = DH^{-2\delta+4} \tag{5}$$

where D is an unknown parameter.

For $\delta = 1$, the THDE density becomes the usual holographic dark energy density. For $\delta = 2$, ρ_{THDE} =constant, i.e., the dark energy behaves like cosmological constant.

Now, in comoving coordinate system the equations (4) with (2) and (3) for the metric (1) lead to the following system of field equations:

$$\frac{\ddot{B}}{B} + \frac{\ddot{C}}{C} + \frac{\dot{B}\dot{C}}{BC} - \frac{m^2}{A^2} = -p_{THDE} \tag{6}$$

$$\frac{\ddot{C}}{C} + \frac{\ddot{A}}{A} + \frac{\dot{C}\dot{A}}{CA} - \frac{m^2}{A^2} = -p_{THDE} \tag{7}$$

$$\frac{\ddot{A}}{A} + \frac{\ddot{B}}{B} + \frac{\dot{A}\dot{B}}{AB} - \frac{m^2}{A^2} = -p_{THDE} \tag{8}$$

$$\frac{\dot{A}\dot{B}}{AB} + \frac{\dot{B}\dot{C}}{BC} + \frac{\dot{C}\dot{A}}{CA} - \frac{3m^2}{A^2} = \rho_m + \rho_{THDE} \tag{9}$$

$$2\frac{\dot{A}}{A} - \frac{\dot{B}}{B} - \frac{\dot{C}}{C} = 0 \tag{10}$$

where an over dot denotes differentiation with respect to cosmic time t.

From equation (10), integrating and suppressing the constant of integration, we get

$$A^2 = BC \tag{11}$$

The conservation of energy-momentum yields

$$\dot{\rho}_m + \dot{\rho}_{THDE} + 3H(\rho_m + \rho_{THDE} + p_{THDE}) = 0 \tag{12}$$

But the continuity equation for the cold dark matter is

$$\dot{\rho}_m + 3H\rho_m = 0 \tag{13}$$

And the continuity equation of the THDE is

$$\dot{\rho}_{THDE} + 3H(\rho_{THDE} + p_{THDE}) = 0 \tag{14}$$

The equation of state parameter for THDE is

$$\omega_{THDE} = \frac{p_{THDE}}{\rho_{THDE}} \tag{15}$$

Therefore, from (5), (14) and (15), we have

$$\omega_{THDE} = -1 - (-2\delta + 4)\frac{\dot{H}}{3H^2} \tag{16}$$

COSMOLOGICAL SOLUTIONS OF THE FILED EQUATIONS

From equations (6) - (9), we derive

$$B(t) = M_1 a \exp\left(N \int a^{-3} dt\right) \tag{17}$$

$$C(t) = M_2 a \exp\left(-N \int a^{-3} dt\right) \tag{18}$$

where M_1, M_2 and N are relevant constants used in the derivation and $a = (ABC)^{\frac{1}{3}}$ is the average scale factor.

In order to obtain a complete solution of the field equations, we consider the hybrid expansion law proposed by Akarsu *et al*. (2014) [24] as

$$a(t) = a_0 \left(\frac{t}{t_0}\right)^{\gamma} e^{\xi\left(\frac{t}{t_0}-1\right)} \tag{19}$$

where a_0 and t_0 are the present values of the scale factor and age of the universe respectively.

The value of γ is in the range $(0,1)$ and behavior of the universe at late time is determined by the value of ξ. In this work we take $\gamma = 0.5$ and investigate the behavior of the Tsallis holographic dark energy for different values of ξ.
Using (19) in (17) and (18), we get

$$B(t) = M_1 \left(k t^{3\gamma} e^{\frac{3\xi t}{t_0}}\right)^{\frac{1}{3}} \exp\left(NF(t)\right) \tag{20}$$

$$C(t) = M_2 \left(k t^{3\gamma} e^{\frac{3\xi t}{t_0}}\right)^{\frac{1}{3}} \exp\left(-NF(t)\right) \tag{21}$$

where $F(t) = \int (k t^{3\gamma} e^{\frac{3\xi t}{t_0}})^{-1} dt$ and k is a non zero constant.
Now, from (11) using (20) and (21), we get

$$A(t) = (M_1 M_2)^{\frac{1}{2}} \left(k t^{3\gamma} e^{\frac{3\xi t}{t_0}}\right)^{\frac{1}{3}} \tag{22}$$

RESULTS AND DISCUSSION

For the metric given in (1), the directional Hubble parameters are obtained as

$$H_1 = \frac{\dot{A}}{A} = \left(\frac{\gamma}{t} + \frac{\xi}{t_0}\right) \tag{23}$$

$$H_2 = \frac{\dot{B}}{B} = \left(\frac{\gamma}{t} + \frac{\xi}{t_0}\right) + NF'(t) \tag{24}$$

$$H_3 = \frac{\dot{C}}{C} = \left(\frac{\gamma}{t} + \frac{\xi}{t_0}\right) - NF'(t) \tag{25}$$

Hence the mean Hubble parameter (H) is obtained as

$$H = \frac{1}{3}\left(\frac{\dot{A}}{A} + \frac{\dot{B}}{B} + \frac{\dot{C}}{C}\right) = \frac{\gamma}{t} + \frac{\xi}{t_0} \tag{26}$$

The deceleration parameter and the jerk parameter are obtained as

$$q(t) = -\frac{\ddot{a}}{aH^2} = -1 + \frac{\gamma t_0^2}{(\xi t + \gamma t_0)^2} \tag{27}$$

$$j(t) = \frac{\dddot{a}}{aH^3} = 1 + \frac{(2t_0 - 3\xi t - 3\gamma t_0)\gamma t_0^2}{(\xi t + \gamma t_0)^3} \tag{28}$$

From equation (27) and (28), it is obvious that the universe transitioned from decelerating to accelerating phase. The scalar of expansion θ, the spatial volume$V$, the shear scalar σ^2 and the anisotropy parameter A_m for this model are obtained as

$$\theta = 3H = 3\left(\frac{\gamma}{t} + \frac{\xi}{t_0}\right) \tag{29}$$

$$\sigma^2 = \frac{1}{2}\left[\sum_{i=1}^{3} H_i^2 - \frac{1}{3}\theta^2\right] = \frac{N^2}{\left(kt^{3\gamma}e^{\frac{3\xi t}{t_0}}\right)^2} \tag{30}$$

$$V = a^3 = \left(a_0\left(\frac{t}{t_0}\right)^{\gamma} e^{\xi\left(\frac{t}{t_0}-1\right)}\right)^3 \tag{31}$$

$$A_m = \frac{1}{3}\sum_{i=1}^{3}\frac{(H_i-H)^2}{H^2} = \frac{2N^2}{3}\frac{\left(kt^{3\gamma}e^{\frac{3\xi t}{t_0}}\right)^{-2}}{\left(\frac{\gamma}{t}+\frac{\xi}{t_0}\right)^2} \tag{32}$$

Using (26) in (5) we get

$$\rho_{THDE} = D\left(\frac{\gamma}{t}+\frac{\xi}{t_0}\right)^{-2\delta+4} \tag{33}$$

Again using (26) in (13), we get

$$\rho_m = C\left[t^{-3\gamma}e^{-\frac{\xi t}{t_0}}\right] \tag{34}$$

where C is a constant of integration.
Hence, the total energy density and EoS parameter are

$$\Omega = \Omega_m + \Omega_{THDE} = \frac{C\left[t^{-3\gamma}e^{-\frac{\xi t}{t_0}}\right] + D\left(\frac{\gamma}{t}+\frac{\xi}{t_0}\right)^{-2\delta+4}}{3\left(\frac{\gamma}{t}+\frac{\xi}{t_0}\right)^2} \tag{35}$$

$$\omega_{THDE} = -1 + (-2\delta+4)\frac{\gamma t_0^2}{3(\gamma t_0+\xi t)^2} \tag{36}$$

Cosmology for $\delta = 1$:
For $\delta = 1$, the THDE density, total energy density and EoS parameter become

$$\rho_{THDE} = D\left(\frac{\gamma}{t}+\frac{\xi}{t_0}\right)^2 \tag{37}$$

$$\Omega = \frac{D}{3} + \frac{C\left[t^{-3\gamma}e^{-\frac{\xi t}{t_0}}\right]}{3\left(\frac{\gamma}{t}+\frac{\xi}{t_0}\right)^2} \tag{38}$$

$$\omega_{THDE} = -1 + \frac{2\gamma t_0^2}{3(\gamma t_0+\xi t)^2} \tag{39}$$

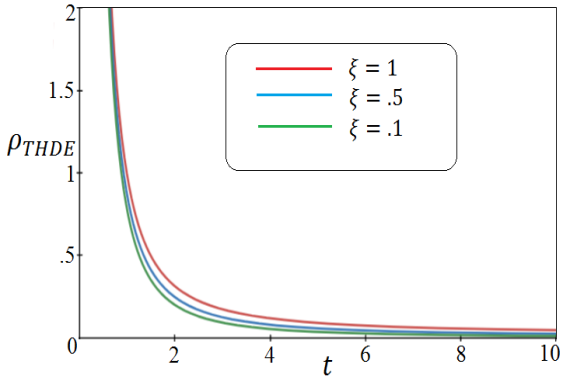

Figure 1. The plot of THDE density vs. cosmic time t with $D = 3, \gamma = 0.5$ and $\xi = 1, 0.5, 0.1$

The Figure 1 exhibits that the Tsallis holographic dark energy density decreases for any value of ξ while for smaller value of ξ, the THDE density decreases rapidly.

From Figures 2 and 3, we observe that the holographic dark energy dominates the universe and approaches flat, isotropic universe at late times for large value of ξ. For small value of ξ ($\ll 1$), the dark energy dominates the universe lately and the universe never reaches isotropic background.

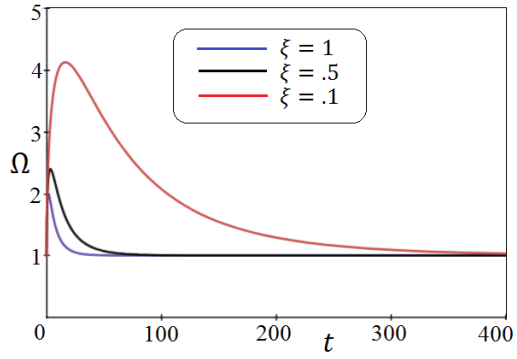

Figure 2. The plot of total energy density vs. cosmic time t with $D = 3, C = 1, t_0 = 13.8,\ \gamma = 0.5$ and $\xi = 1, 0.5, 0.1$

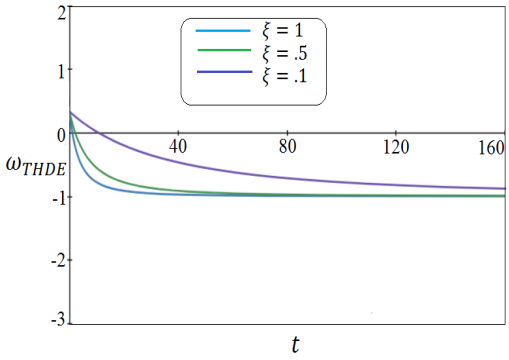

Figure 3. The plot of EoS parameter vs. cosmic time t with $t_0 = 13.8,\ \gamma = 0.5$ and $\xi = 1, 0.5, 0.1$

Cosmology for $1 < \delta < 2$:

In this case the value of δ lies between 1 and 2. We choose $\delta = 1.3$ and plot the graphs of the total energy density Ω versus the cosmic time t for $\xi = 12, 14, 15$ (Fig. 4).

From the graph, it is obvious that the total energy density approaches the present isotropic background for $\xi \approx 14$ and for smaller value of ξ it never approaches isotropic background. However, for relatively larger value of ξ, the total energy density will tend to 1 not at present time but at late time.

Hence we draw the graph of THDE density and EoS parameter vs. cosmic time t for $\xi = 14$ (Fig. 5).

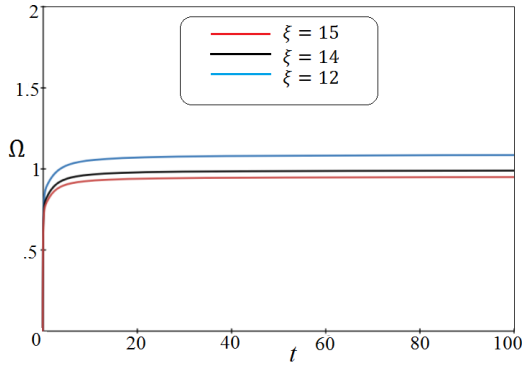

Figure 4. The plot of total energy density vs. cosmic time t with $D = 3, C = 1, t_0 = 13.8, \delta = 1.3,\ \gamma = 0.5$ and $\xi = 12, 14, 15$

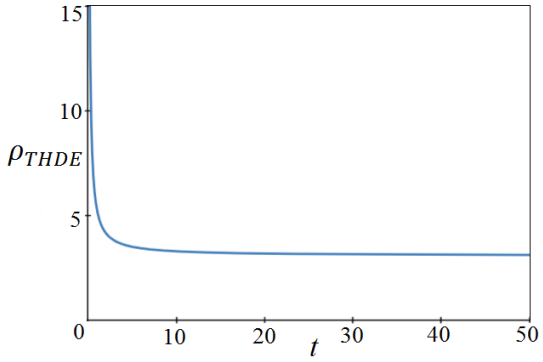

Figure 5. The plot of THDE density vs. cosmic time t with $D = 3, C = 1, t_0 = 13.8, \delta = 1.3,\ \gamma = 0.5$ and $\xi = 14$

Like the previous case ($\delta = 1$), here also THDE density decreases but it never tends to zero at late times (Fig. 6).

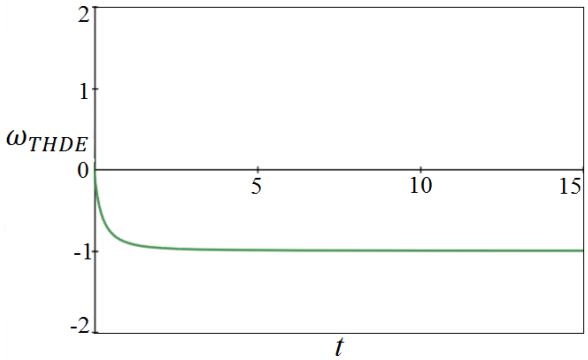

Figure 6. The plot of EoS parameter vs. cosmic time t with $t_0 = 13.8, \delta = 1.3,\ \gamma = .5$ and $\xi = 14$

From the above graph we see that the dark energy started to dominate the universe from the early era and behaves like cosmological constant at late times.

Cosmology for $\delta = 2$:

For $\delta = 2$, the Tsallis holographic dark energy becomes constant throughout the evolution, and the universe is highly anisotropic at late time. The expression of THDE density, total energy density and EoS parameter for $\delta = 2$ are obtained as

$$\rho_{THDE} = D \tag{40}$$

$$\Omega = \frac{C\left[t^{-3\gamma}e^{-\frac{\xi t}{t_0}}\right]+D}{3(\frac{\gamma}{t}+\frac{\xi}{t_0})^2} \tag{41}$$

$$\omega_{THDE} = -1 \tag{42}$$

From the Figure 7, it is clear that in this case the universe approaches flat and isotropic background for $\xi = 14$.

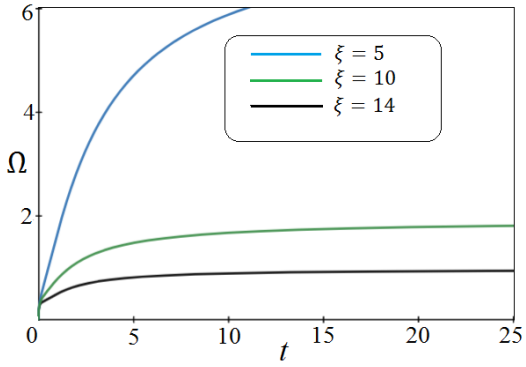

Figure 7. The plot of total energy density vs. cosmic time t with $t_0 = 13.8, \delta = 2,\ \gamma = 0.5$ and $\xi = 14, 10, 5$

CONCLUSION

In this paper, we study a spatially homogeneous and anisotropic Bianchi Type V universe filled with cold dark matter and non-interacting Tsallis holographic dark energy with Hubble horizon as the IR cutoff. Exact solutions of the Einstein field equations are obtained by considering the hybrid expansion law proposed by Akarsu *et al*. (2014) [24]. We study the cosmological dynamics of our model for $\delta = 1, 1 < \delta < 2$ and 2. We find that

- For $\delta = 1$, the THDE density (usual holographic dark energy density) decreases for any value of ξ and decreases rapidly for relatively smaller value of ξ. Also, the universe approaches a flat and isotropic universe at late times for any value of ξ while the universe approaches dark energy dominated era lately for $\xi \ll 1$.
- For $\delta = 1.3$, the universe approaches present isotropic background for $\xi \approx 14$. At this value, the THDE dark energy density decreases but does not tend to 0 at late times. Also, the dark energy dominates the universe from very early era.
- For $\delta = 2$, the THDE density is constant throughout the evolution of the universe and the dark energy behaves like cosmological constant. In this case also, the universe approaches isotropic background for $\xi \approx 14$.

ORCID IDs

Manash Pratim Das, https://orcid.org/0000-0002-1179-8068, **Chandra Rekha Mahanta**, https://orcid.org/0000-0002-8019-8824

REFERENCES

[1] S. Perlmutter, G. Aldering, M. Della Valle, S. Deustua, R.S. Ellis, S. Fabbro, A. Fruchter, et al, "Discovery of supernovae explosion at half the age of the universe", Nature, **391**, 51 (1998). https://doi.org/10.1038/34124
[2] S. Perlmutter, G. Aldering, G. Goldhaber, R.A. Knop, P. Nugent, P.G. Castro, S. Deustua, et al, "Measurement of Ω and Λ from 42 High-Red shift Supernovae", Astrophys. J. **517**, 565 (1999). https://doi.org/10.1086/307221
[3] A.G. Riess, A.V. Filippenko, P. Challis, A. Clocchiatti, A. Diercks, P.M. Garnavich, R.L. Gilliland, et al, "Observational evidence from supernovae for an accelerating universe and a cosmological constant", Astron. J. **116**, 1009 (1998). https://doi.org/10.1086/300499
[4] C.L. Bennett, M. Halpern, G. Hinshaw, N. Jarosik, A. Kogut, M. Limon, S.S. Meyer, et al, "First-Year Wilkinson Microwave Anisotropy Probe (WMAP) Observations: Preliminary Maps and Basic Results", Astrophys. J. **148**, 1 (2003). https://doi.org/10.1086/377253
[5] D.N. Spergel, L. Verde, H.V. Peiris, E. Komatsu, M.R. Nolta, C.L. Bennett, M. Halpern, et al, "First-Year Wilkinson Microwave Anisotropy Probe (WMAP)*Observations: Determination of Cosmological Parameters", Astrophys. J. Suppl. Ser. **148**, 175 (2003). https://doi.org/10.1086/377226
[6] L. Verde, A.F. Heavens, W.J. Percival, S. Matarrese, C.M. Baugh, J. Bland-Hawthorn, T. Bridges, et al, "The 2dF Galaxy Redshift Survey: the bias of galaxies and the density of the Universe", Mon. Not. R. Astron. Soc. **335**, 432 (2002). https://doi.org/10.1046/j.1365-8711.2002.05620.x
[7] V. Sahni, and A.A. Starobinsky, "The Case for a Positive Cosmological Lambda-term", Int. J. Mod. Phys. D, **9**, 373 (2000). https://doi.org/10.1142/S0218271800000542
[8] Caldwell, R. R., "A phantom menace? Cosmological consequences of dark energy component with super- negative equation of state", Phys. Lett. B, **545**, 23 (2002). https://doi.org/10.1016/S0370-2693(02)02589-3
[9] C. Armendariz-Picon, V. Mukhanov, and P.J. Steinhardt, "Essentials of k-essence", Phys. Rev. D, **63**, 103510 (2001). https://doi.org/10.1103/PhysRevD.63.103510

[10] A. Sen, "Rolling Tachyon", J. High Energy Phys., **204**, 48 (2002). https://doi.org/10.1088/1126-6708/2002/04/048
[11] M. Gasperini, F. Piazza, and G. Veneziano, "Quintessence as a runaway dilaton", Phys. Rev. D, **65**, 023508 (2001). https://doi.org/10.1103/PhysRevD.65.023508
[12] M.C. Bento, O. Bertolami, and A.A. Sen, "Generalized Chaplygin gas, accelerated expansion and dark-matter unification", Phys. Rev. D, **66**, 043507 (2002). https://doi.org/10.1103/PhysRevD.66.043507
[13] C. Deffayet, G. Dvali, and G. Gabadadze, "Accelerated universe from gravity leaking to extra dimension" Phys. Rev. D, **65**, 044023 (2002). https://doi.org/10.1103/PhysRevD.65.044023
[14] G.'t Hooft, "Dimensional Reduction in Quantum Gravity", (1993). https://doi.org/10.48550/arXiv.gr-qc/9310026
[15] W. Fischler, and L. Susskind, "Holography and Cosmology", (1998). https://doi.org/10.48550/arXiv.hep-th/9806039
[16] C. Tsallis, and L.J.L.Cirto, "Black hole thermodynamical entropy", Eur. Phys. J. C, **73**, 2487 (2013). https://doi.org/10.1140/epjc/s10052-013-2487-6
[17] M. Tavayef, A. Sheykhi, K. Bamba, and H. Moradpour, "Tsallis holographic dark energy", Physics Letters B, **781**, 195 (2018). https://doi.org/10.1016/j.physletb.2018.04.001
[18] S. Ghaffari, "Holographic dark energy model in the DGP braneworld with time varying holographic parameter", New astronomy, **67**, 76 (2019). https://doi.org/10.1016/j.newast.2018.09.002
[19] M. Korunur, "Tsallis holographic dark energy in Bianchi type-III spacetime with scalar fields", Mod. Phys. Lett. A, **34**, 1950310 (2019). https://doi.org/10.1142/S0217732319503103
[20] U.K. Sharma, and A. Pradhan, "Diagnosing Tsallis holographic dark energy models with statefinder and$\omega - \omega'$ pair", Mod. Phys. Lett. A, **34**, 1950101 (2019). https://doi.org/10.1142/S0217732319501013
[21] V.C. Dubey, A.K. Mishra, S. Srivastava, and U.K. Sharma, "Tsallis holographic dark energy models in axially symmetric space time", Int. J. Geom. Meth. Modern Phys. **17**, 2050011 (2020).https://doi.org/10.1142/S0219887820500115
[22] Y. Liu, "Tachyon model of Tsallis holographic dark energy", Eur. Phys. J. Plus, **136**, 579 (2021). https://doi.org/10.1140/epjp/s13360-021-01573-y
[23] A. Mohammadi, T. Golanbari, K. Bamba, and I.P. Lobo, "Tsallis holographic dark energy for inflation", Phys. Rev. D, **103**, 083505 (2021). https://doi.org/10.1103/PhysRevD.103.083505
[24] B.D. Pandey, P.S. Kumar, Pankaj, and U.K. Sharma, "New Tsallis holographic dark energy", Eur. Phys. J. C, **82**, 233 (2022). https://doi.org/10.1140/epjc/s10052-022-10171-w
[25] P.S. Kumar, Pankaj, and U.K. Sharma, "Quintessence model of Tsallis holographic dark energy", New Astronomy, **96**, 101829 (2022). https://doi.org/10.1016/j.newast.2022.101829
[26] Ö. Akarsu, S. Kumar, R. Myrzakulov, M. Sami, and L. Xu, "Cosmology with hybrid expansion law: scalar field reconstruction of cosmic history and observational constraints", J. Cosmol. Astropart. Phys. **01**, 022 (2014). https://doi.org/10.1088/1475-7516/2014/01/022

ГОЛОГРАФІЧНА МОДЕЛЬ ТЕМНОЇ ЕНЕРГІЇ БІАНЧІ ТИПУ V ЦАЛЛІСА З ГІБРИДНИМ ЗАКОНОМ РОЗШИРЕННЯ

Манаш Пратім Дас, Чандра Рекха Маханта
Факультет математики, Університет Гаухаті, Гувахаті (Індія)

Кілька останніх космологічних спостережень надали все більше доказів того, що в даний час Всесвіт переживає фазу прискореного розширення, першопричиною якого, як припускають, є екзотичний компонент Всесвіту з великим негативним тиском, який називається темною енергією. З різних кандидатів темної енергії, запропонованих у літературі, голографічна темна енергія, яка виникла з голографічного принципу, привертає велику увагу в галузі досліджень. У цій статті ми досліджуємо просторово однорідний та анізотропний простір-час Б'янкі типу V, заповнений невзаємодіючою голографічною темною енергією Цалліса (THDE) з горизонтом Хаббла як межею інфрачервоного випромінювання та холодною темною матерією без тиску в рамках загальної теорії відносності. Отримано точні розв'язки рівнянь поля Ейнштейна, розглядаючи середній масштабний коефіцієнт a як комбінацію степеневого та експоненціального законів, так званого гібридного закону розширення, вперше запропонованого Акарсу та ін. (2014). Ми вивчаємо космологічну динаміку різних моделей для різних значень неадитивного параметра δ, який з'явився в ентропії Цалліса, і для ξ, який з'явився в експоненціальній функції гібридного закону розширення. Ми виявили, що наша модель демонструє поточний космологічний сценарій.

Ключові слова: голографічна темна енергія Цалліса, тип Б'янкі V, закон гібридного розширення, прискорене розширення

East European Journal of Physics. 3. 104-114 (2022)
DOI:10.26565/2312-4334-2022-3-14 ISSN 2312-4334

NON-RELATIVISTIC STUDY OF MASS SPECTRA AND THERMAL PROPERTIES OF A QUARKONIUM SYSTEM WITH ECKART-HELLMANN POTENTIAL†

Etido P. Inyang[a]*, Effiong O. Obisung[d], Eddy S. William[b], Ituen B. Okon[c]
[a]*Department of Physics, National Open University of Nigeria, Jabi-Abuja, Nigeria*
[b]*Theoretical Physics Group, Department of Physics, University of Calabar, PMB 1115, Calabar, Nigeria*
[c]*Theoretical Physics Group, Department of Physics, University of Uyo, Nigeria*
[d]*Department of Physics, University of Calabar, PMB 1115, Calabar, Nigeria*
**Corresponding author email: etidophysics@gmail.com*
Received August 13, 2022; revised August 17, 2022; accepted August 22, 2022

In this present study, we model Eckart-Hellmann Potential (EHP) to interact in a quark-antiquark system. The solutions of the Schrödinger equation are obtained with EHP using the Nikiforov-Uvarov method. The energy equation and normalized wave function were obtained. The masses of the heavy mesons such as charmonium ($c\bar{c}$) and bottomonium ($b\bar{b}$) for different quantum numbers were predicted using the energy equation. Also, the partition function was calculated from the energy equation, thereafter other thermal properties such as mean energy, free energy, entropy, and specific heat capacity were obtained. The results obtained showed an improvement when compared with the work of other researchers and excellently agreed with experimental data.
Keywords: Schrödinger equation; Nikiforov-Uvarov method; Eckart-Hellmann Potential; heavy mesons; Thermal properties
PACS: 12.39.Jh

The mass spectra (MS) of the heavy mesons (HMs) interactions can be well studied by the Schrodinger equation (SE) [1--3]. In describing the interaction of the HMs, confining-type potentials are generally used, which is the Cornell potential (CP) with two terms of Coulomb interaction and a confining term [4]. More so, in solving this equation with any chosen potential, an analytical method is employed. Most of the analytical methods used are as follows, the Nikiforov-Uvarov (NU) method [5-8], the Nikiforov-Uvarov Functional Analysis (NUFA) method [9,10], series expansion method (SEM) [11,12], Laplace transformation method (LTM)[13],WKB approximation method [14,15] and so on[16]. The study of MS with CP has gained remarkable interest and has attracted the attention of many scholars [17-20]. For instance, Kumar et al.,[21] used the NUFA method to solve the SE with generalized Cornell potential. The result was used to predict the MS of the HMs. Using, the vibrational method and supersymmetric quantum mechanics Vega and Flores, [22] obtained the analytical solutions of the SE with CP. The eigenvalues were used to calculate the MS of the HMs. Also, Mutuk [23] solved the SE with CP using a neural network approach. The bottomonium, charmonium, and bottom-charmed spin-averaged spectra were calculated. Furthermore, Hassanabadi et al. [24], used the variational method to solve the SE with CP. The eigenvalues were used to calculate the mesonic wave function.

In recent times, the study of MS of the HMs with exponential-type potentials has aroused the interest of scholars [25, 26]. Potential models such as Yukawa potential [27], Varshni [28], screened Kratzer potential [29], Hulthen plus Hellmann potential [30], and so on have been used in the prediction of the MS of the HMs. For instance, Purohit et al [31] combined linear plus modified Yukawa potential to obtain the masses of the HMs through the solutions of the Klein-Gordon equation. The SE for most of the potentials with spin addition cannot be solved analytically; hence, numerical solutions such as Runge-Kutte approximation [32], Numerov matrix method [33], Fourier grid Hamiltonian method [34], and so on [35] are employed. Also, adding spin enables one to determine other properties of the mesons like decay properties and root mean square radii. However, we have considered our mesons as spinless particles for easiness [1, 25, 36-38]. Furthermore, the thermal properties (TPs) of the HMs have been calculated recently [39-41].

The Eckart potential [42], is a potential model that has great significance in physics. Also, Hellmann potential [43], has been widely utilized in physics [44]. Hence, Inyang et al [45], proposed the Eckart-Hellmann potential (EHP) model through their combination to study selected diatomic molecules.

The combination of at least two potential models has a propensity to fit experimental data more than a single potential [40], hence this study. This study aims to model EHP to fit in the Cornell potential, and to predict the mass spectra of the heavy mesons through the solutions of the SE using the NU method.

The EHP takes the form [45],

$$V(q) = -\frac{R_0 e^{-\sigma q}}{1-e^{-\sigma q}} + \frac{R_1 e^{-\sigma q}}{\left(1-e^{-\sigma q}\right)^2} - \frac{R_2}{q} + \frac{R_3 e^{-\sigma q}}{q}, \tag{1}$$

where $R_0, R_1, R_2,$ and R_3 are the strength of the potential, σ is the screening parameter to be determined later and q is inter-nuclear distance.

† ***Cite as:*** E.P. Inyang, E.O. Obisung, E.S. William, and I.B. Okon, East Eur. J. Phys. **3**, 104 (2022), https://doi.org/10.26565/2312-4334-2022-3-14

The exponential terms in Eq. (1) are expanded with the power series up to order three, so the potential can be used to study quarkonia system. Equations (2), (3), and (4) are obtained.

$$\frac{e^{-\sigma q}}{q}=\frac{1}{q}-\sigma+\frac{\sigma^2 q}{2}-\frac{\sigma^3 q^2}{6}+\ldots, \tag{2}$$

$$\frac{e^{-\sigma q}}{1-e^{-\sigma q}}=\frac{1}{\sigma q}-\frac{1}{2}+\frac{\sigma q}{12}+\ldots, \tag{3}$$

$$\frac{e^{-\sigma q}}{\left(1-e^{-\sigma q}\right)^2}=\frac{1}{\sigma^2 q^2}-\frac{1}{12}+\frac{\sigma^2 q^2}{240}+\ldots \tag{4}$$

Putting Eqs. (2), (3)and (4) into Eq. (1) we have

$$V(q)=-\frac{G_0}{q}+G_1 q+G_2 q^2+\frac{G_3}{q^2}+G_4, \tag{5}$$

where

$$\left.\begin{aligned} G_0&=\frac{R_0}{\sigma}+R_2-R_3,\ \mathrm{G}_1=-\frac{\sigma R_0}{12}+\frac{\sigma^2 R_3}{2}\\ G_2&=\frac{R_1\sigma^2}{240}-\frac{R_3\sigma^3}{6},\ \mathrm{G}_3=\frac{R_1}{\sigma^2},\ \mathrm{G}_4=\frac{R_0}{2}-\frac{R_1}{12}-\sigma R_3 \end{aligned}\right\} \tag{6}$$

2. The solutions of the SE with EHP

The NU method is adopted with details found in Ref. [46]. The SE of the form is used [47]

$$\frac{d^2\,\mathrm{U}(q)}{dq^2}+\left[\frac{2\mu}{\hbar^2}\left(E_{nl}-V(q)\right)-\frac{l\left(l+1\right)}{q^2}\right]\mathrm{U}(q)=0 \tag{7}$$

where l, is the angular momentum quantum number, μ, is the reduced mass for the quark-antiquark particle, q is the inter-particle distance, and $\hbar$ is reduced plank constant.

Then, we substitute Eq. (5) into Eq. (7), the radial wave equation is obtained as

$$\frac{d^2\,\mathrm{U}(q)}{dq^2}+\left[\frac{2\mu E}{\hbar^2}+\frac{2\mu G_0}{\hbar^2 q}-\frac{2\mu G_1 q}{\hbar^2}-\frac{2\mu G_2 q^2}{\hbar^2}-\frac{2\mu G_3}{\hbar^2 q^2}-\frac{2\mu G_4}{\hbar^2}-\frac{l(l+1)}{q^2}\right]\mathrm{U}(q)=0. \tag{8}$$

Transformation of q (in Eq. (8)) to w coordinates yields Eq.(9),

$$w=\frac{1}{q}, q\succ 0. \tag{9}$$

The second derivatives of Eq. (9) is given as,

$$\frac{d^2U(q)}{dq^2}=2w^3\frac{dU(w)}{dw}+w^4\frac{d^2U(w)}{dw^2}. \tag{10}$$

Substituting Eqs. (9) and (10) in Eq. (8) gives;

$$\frac{d^2\,\mathrm{U}(w)}{dw^2}+\frac{2w}{w^2}\frac{dU}{dw}+\frac{1}{w^4}\left[\begin{aligned}&\frac{2\mu E}{\hbar^2}+\frac{2\mu G_0 w}{\hbar^2}-\frac{2\mu G_1}{\hbar^2 w}\\&-\frac{2\mu G_2}{\hbar^2 w^2}-\frac{2\mu G_3 w^2}{\hbar^2}-\frac{2\mu G_4}{\hbar^2}-l\left(l+1\right)w^2\end{aligned}\right]\mathrm{U}(w)=0. \tag{11}$$

The approximation scheme (AS) on the terms is introduced by assuming that there is a characteristic radius r_0 of the meson. The AS is achieved by the expansion of $\frac{G_1}{w}$ and $\frac{G_2}{w^2}$ in a power series around r_0; i.e. around $\delta \equiv \frac{1}{r_0}$, up to the second-order [48].

By setting $y = w - \delta$ and around $y = 0$ we expand it in powers of series as;

$$\frac{G_1}{w} = \frac{G_1}{y+\delta} = \frac{G_1}{\delta\left(1+\frac{y}{\delta}\right)} = \frac{G_1}{\delta}\left(1+\frac{y}{\delta}\right)^{-1}. \tag{12}$$

Equation (12) yields

$$\frac{G_1}{w} = G_1\left(\frac{3}{\delta} - \frac{3z}{\delta^2} + \frac{z^2}{\delta^3}\right). \tag{13}$$

Similarly,

$$\frac{G_2}{w^2} = G_2\left(\frac{6}{\delta^2} - \frac{8w}{\delta^3} + \frac{3w^2}{\delta^4}\right). \tag{14}$$

Also, stroking Eqs. (13) and (14) into Eq. (11) gives:

$$\frac{d^2\,\mathrm{U}(w)}{dw^2} + \frac{2w}{w^2}\frac{dU(w)}{dw} + \frac{1}{w^4}\left[-\varepsilon + X_0 w - X_1 w^2\right]\mathrm{U}(w) = 0, \tag{15}$$

where

$$\left.\begin{aligned} -\varepsilon &= \left(\frac{2\mu E}{\hbar^2} - \frac{6\mu G_1}{\hbar^2\delta} - \frac{12\mu G_2}{\hbar^2\delta^2} - \frac{2\mu G_4}{\hbar^2}\right),\ X_0 = \left(\frac{2\mu G_0}{\hbar^2} + \frac{6\mu G_1}{\hbar^2\delta^2} + \frac{16\mu G_2}{\hbar^2\delta^3}\right) \\ X_1 &= \left(\frac{2\mu G_1}{\hbar^2\delta^3} + \frac{6\mu G_2}{\hbar^2\delta^4} + \frac{2\mu G_3}{\hbar^2} + \gamma\right),\ \gamma = l(l+1) \end{aligned}\right\}. \tag{16}$$

Linking Eq. (15) and Eq. (1) of Ref. [46], gives

$$\left.\begin{aligned} &\tilde{\tau}(w) = 2w,\ \sigma(w) = z^2 \\ &\tilde{\sigma}(w) = -\varepsilon + \alpha w - \beta w^2 \\ &\sigma'(w) = 2w,\ \sigma''(w) = 2 \end{aligned}\right\}. \tag{17}$$

Plugging Eq. (17) into Eq. (11) of Ref. [46],

$$\pi(w) = \pm\sqrt{\varepsilon - X_0 w + \left(X_1 + k\right)w^2}. \tag{18}$$

To determine k, in Eq. (18), the discriminant of the function (Eq. (19)) and Eq. (20) were obtained,

$$k = \frac{X_0{}^2 - 4X_1\varepsilon}{4\varepsilon}, \tag{19}$$

$$\pi(w) = \pm\left(\frac{X_0 w}{2\sqrt{\varepsilon}} - \frac{\varepsilon}{\sqrt{\varepsilon}}\right). \tag{20}$$

For acceptable solution, the negative part of Eq. (20) is essential for bound state problems, upon differentiating we get.

$$\pi_{-}'(w) = -\frac{X_0}{2\sqrt{\varepsilon}}. \tag{21}$$

By placing Eqs. (17) and (20) into Eq. (6) of Ref. [46]

$$\tau(w) = 2w - \frac{X_0 w}{\sqrt{\varepsilon}} + \frac{2\varepsilon}{\sqrt{\varepsilon}} \tag{22}$$

Differentiating Eq. (22) gives,

$$\tau'(w) = 2 - \frac{X_0}{\sqrt{\varepsilon}} \tag{23}$$

Usingto Eq. (19) and Eq. (21) of Ref. [46], gives,

$$\lambda = \frac{X_0{}^2 - 4X_1\varepsilon}{4\varepsilon} - \frac{X_0}{2\sqrt{\varepsilon}} \tag{24}$$

$$\lambda_n = \frac{nX_0}{\sqrt{\varepsilon}} - n^2 - n \tag{25}$$

Equating Eqs. (24) and (25), followed by the substitution of Eqs. (6) and (16) yielded the energy eigenvalue equation of the EHP

$$E_{nl} = \frac{R_0}{2} - \frac{R_1}{12} - R_0R_3 + \frac{3}{\delta}\left(-\frac{\sigma R_0}{12} + \frac{R_3\sigma^2}{2}\right) + \frac{6}{\delta^2}\left(\frac{R_1\sigma^2}{240} - \frac{R_3\sigma^3}{6}\right)$$
$$-\frac{\hbar^2}{8\mu}\left[\frac{\frac{2\mu}{\hbar^2}\left(\frac{R_0}{\sigma} + R_2 - R_3\right) + \frac{6\mu}{\hbar^2\delta^2}\left(-\frac{\sigma R_0}{12} + \frac{R_3\sigma^2}{2}\right) + \frac{16\mu}{\hbar^2\delta^3}\left(\frac{R_1\sigma^2}{240} - \frac{R_3\sigma^3}{6}\right)}{n + \frac{1}{2} + \sqrt{\left(\frac{1}{2}+l\right)^2 + \frac{2\mu}{\hbar^2\delta^3}\left(-\frac{\sigma R_0}{12} + \frac{R_3\sigma^2}{2}\right) + \frac{6\mu}{\hbar^2\delta^4}\left(\frac{R_1\sigma^2}{240} - \frac{R_3\sigma^3}{6}\right) + \frac{2\mu R_1}{\hbar^2\sigma^2}}}\right]^2 \tag{26}$$

The wave function, is obtained by putting Eqs. (17) and (20) into Eq. (4) of Ref. [46]

$$\frac{d\phi}{\phi} = \left(\frac{\varepsilon}{w^2\sqrt{\varepsilon}} - \frac{X_0}{2w\sqrt{\varepsilon}}\right)dw \tag{27}$$

Integration of Eq. (27) gives

$$\phi(w) = w^{-\frac{X_0}{2\sqrt{\varepsilon}}} e^{-\frac{\varepsilon}{w\sqrt{\varepsilon}}} \tag{28}$$

2.1 Determination of the weight function

Upon differentiating the left-hand of Eq. (6) of Ref. [46] we have,

$$\frac{\rho'(w)}{\rho(w)} = \frac{\tau(w) - \sigma'(w)}{\sigma(w)} \tag{29}$$

The substitution of Eqs. (17) and (22) into Eq. (29) and thereafter integrate, gave

$$\rho(w) = w^{-\frac{X_0}{\sqrt{\varepsilon}}} e^{-\frac{2\varepsilon}{w\sqrt{\varepsilon}}} \tag{30}$$

The substitution of Eqs. (17) and(30) into Eq. (5) of Ref. [46] gave

$$y_n(w) = B_n e^{\frac{2\varepsilon}{w\sqrt{\varepsilon}}} z^{\frac{X_0}{\sqrt{\varepsilon}}} \frac{d^n}{dw^n}\left[e^{-\frac{2\varepsilon}{w\sqrt{\varepsilon}}} w^{n-\frac{X_0}{\sqrt{\varepsilon}}}\right] \tag{31}$$

The Rodrigues' formula of the associated Laguerre polynomials is

$$L_n^{\frac{X_0}{\sqrt{\varepsilon}}}\left(\frac{2\varepsilon}{w\sqrt{\varepsilon}}\right) = \frac{1}{n!} e^{\frac{2\varepsilon}{w\sqrt{\varepsilon}}} w^{\frac{X_0}{\sqrt{\varepsilon}}} \frac{d^n}{dw^n}\left(e^{-\frac{2\varepsilon}{w\sqrt{z}}} w^{n-\frac{X_0}{\sqrt{\varepsilon}}}\right) \tag{32}$$

where $B_n = \frac{1}{n!}$.

Hence,

$$y_n(w) \equiv L_n^{\frac{X_0}{\sqrt{\varepsilon}}}\left(\frac{2\varepsilon}{w\sqrt{\varepsilon}}\right) \tag{33}$$

The substitution of Eqs. (28) and (33) into Eq. (2) of Ref. [46], gives the wave function in terms of associated Laguerre polynomials as

$$\psi(w) = N_{nl} w^{-\frac{X_0}{2\sqrt{\varepsilon}}} e^{-\frac{\varepsilon}{w\sqrt{\varepsilon}}} L_n^{\frac{X_0}{\sqrt{\varepsilon}}}\left(\frac{2\varepsilon}{w\sqrt{\varepsilon}}\right) \tag{34}$$

where N_{nl} is normalization constant, which can be obtained from

$$\int_0^\infty |\psi_{nl}(r)|^2 dr = 1 \tag{35}$$

Inserting (34) into (35) with $w = 1/r$ gives

$$N_{nl}^2 \int_0^\infty r^{X_0/\sqrt{\varepsilon}} e^{-2\sqrt{\varepsilon}r}\left[L_n^{X_0/\sqrt{\varepsilon}}\left(2\sqrt{\varepsilon}r\right)\right]^2 dr = 1 \tag{36}$$

By using the transformation $x = 2\sqrt{\varepsilon}r$ we obtained the well-known standard integral of the Laguerre polynomials

$$\frac{N_{nl}^2}{\left(2\sqrt{\varepsilon}\right)^{X_0/\sqrt{\varepsilon}+1}} \int_0^\infty x^{X_0/\sqrt{\varepsilon}} e^{-x}\left[L_n^{X_0/\sqrt{\varepsilon}}(x)\right]^2 dx = 1 \tag{37}$$

The solution of the standard integral [49] is given as

$$\int_0^\infty x^{X_0/\sqrt{\varepsilon}} e^{-x}\left[L_n^{X_0/\sqrt{\varepsilon}}(x)\right]^2 dx = \frac{\Gamma\left(n + X_0/\sqrt{\varepsilon} + 1\right)}{\Gamma(n+1)} \tag{38}$$

Comparing Eqs. (38) and (37) we obtained the normalization factor such that the total wave function of the mesons can be written in closed form as

$$\psi_{nl}(r) = \sqrt{\frac{\left(2\sqrt{\varepsilon}\right)^{X_0/\sqrt{\varepsilon}+1}\Gamma(n+1)}{\Gamma\left(n + X_0/\sqrt{\varepsilon} + 1\right)}} r^{X_0/2\sqrt{\varepsilon}} e^{-\sqrt{\varepsilon}r} L_n^{X_0/\sqrt{\varepsilon}}\left(2\sqrt{\varepsilon}r\right) \tag{39}$$

Special cases

1. When we set $R_0 = R_1 = 0$ Eq. (26) reduces to HP energy

$$E_{nl} = \frac{3R_3\sigma^2}{2\delta} - \frac{R_3\sigma^3}{\delta^2} - \frac{\hbar^2}{8\mu}\left[\frac{\frac{2\mu}{\hbar^2}(R_2 - R_3) + \frac{3\mu R_3\sigma^2}{\hbar^2\delta^2} - \frac{16\mu R_3\sigma^3}{6\hbar^2\delta^3}}{n + \frac{1}{2} + \sqrt{\left(\frac{1}{2}+l\right)^2 + \frac{\mu R_3\sigma^2}{\hbar^2\delta^3} - \frac{\mu R_3\sigma^3}{\hbar^2\delta^4}}}\right]^2 \tag{40}$$

2. When we set $R_2 = R_3 = 0$ Eq. (26) Echart potential energy

$$E_{nl} = E_{nl} = \frac{R_0}{2} - \frac{R_1}{12} - \frac{\sigma R_0}{4\delta} + \frac{R_1\sigma^2}{40\delta^2} - \frac{\hbar^2}{8\mu}\left[\frac{\frac{2\mu R_0}{\sigma\hbar^2} - \frac{\mu\sigma R_0}{2\hbar^2\delta^2} + \frac{\mu R_1\sigma^2}{40\hbar^2\delta^3}}{n + \frac{1}{2} + \sqrt{\left(\frac{1}{2}+l\right)^2 - \frac{\mu\sigma R_0}{6\hbar^2\delta^3} + \frac{6\mu R_1\sigma^2}{40\hbar^2\delta^4} + \frac{2\mu R_1}{\hbar^2\sigma^2}}}\right]^2 \tag{41}$$

3. When we set $R_0 = R_1 = R_3 = \sigma = 0$, Eq. (26) reduces to Coulomb potential energy

$$E_{nl} = -\frac{\mu {R_2}^2}{2\hbar^2 \left(n+l+1\right)^2} \tag{42}$$

The result of Eq. (42) is the same as reported by Ref. [31] in Eq. (36).

3. Thermal Properties of the SE with EHP

To obtain the TPs of the heavy mesons, we first calculate the partition function.
Equation 26 can be written in the form

$$E_{nl} = P_1 - \frac{\hbar^2}{8\mu}\left[\frac{P_2}{\left(n+\theta\right)}\right]^2 \tag{43}$$

where,

$$\theta = \frac{1}{2} + \sqrt{\left(\frac{1}{2}+l\right)^2 + \frac{2\mu}{\hbar^2\delta^3}\left(-\frac{\sigma R_0}{12} + \frac{R_3\sigma^2}{2}\right) + \frac{6\mu}{\hbar^2\delta^4}\left(\frac{R_1\sigma^2}{240} - \frac{R_3\sigma^3}{6}\right) + \frac{2\mu R_1}{\hbar^2\sigma^2}} \tag{44}$$

$$P_1 = \frac{R_0}{2} - \frac{R_1}{12} - R_0R_3 + \frac{3}{\delta}\left(-\frac{\sigma R_0}{12} + \frac{R_3\sigma^2}{2}\right) + \frac{6}{\delta^2}\left(\frac{R_1\sigma^2}{240} - \frac{R_3\sigma^3}{6}\right) \tag{45}$$

$$P_2 = \frac{2\mu}{\hbar^2}\left(\frac{R_0}{\sigma} + R_2 - R_3\right) + \frac{6\mu}{\hbar^2\delta^2}\left(-\frac{\sigma R_0}{12} + \frac{R_3\sigma^2}{2}\right) + \frac{16\mu}{\hbar^2\delta^3}\left(\frac{R_1\sigma^2}{240} - \frac{R_3\sigma^3}{6}\right) \tag{46}$$

3.1 Partition function $Z(\beta)$

The partition function (PF) takes the form [39],

$$Z(\beta) = \sum_{n=0}^{\lambda} e^{-\beta E_{nl}} \tag{47}$$

where, $\beta = \frac{1}{KT}$, K is the Boltzmann constant, T is the absolute temperature, n is the principal quantum number, and λ is the maximum quantum number.
Replacing Eq. (43) into Eq. (47) gives

$$Z(\beta) = \sum_{n=0}^{\lambda} e^{-\beta\left(P_1 - \frac{\hbar^2}{8\mu}\left[\frac{P_2}{\left(n+\theta\right)}\right]^2\right)} \tag{48}$$

In the classical limit, at high temperature T, the summation is replaced by an integral,

$$Z(\beta) = \int_{\theta}^{\lambda+\theta} e^{M_1\beta + \frac{N_1\beta}{\rho^2}}\, d\rho \tag{49}$$

where,

$$\left.\begin{aligned} n+\theta &= \rho \\ M_1 &= -P_1 \\ N_1 &= \frac{\hbar^2 P_2^2}{8\mu} \end{aligned}\right\} \tag{50}$$

Integrating Eq. (49) gives the PF as,

$$Z(\beta) = e^{M_1\beta}\left(\frac{\rho e^{\frac{N_1\beta}{\rho^2}} - N_1\beta\sqrt{\pi}\, erfi\left(\frac{\sqrt{N_1\beta}}{\rho}\right)}{\sqrt{N_1\beta}}\right), \qquad \theta \le \rho \le \lambda + \theta \tag{51}$$

The imaginary error function $erfi(y)$ is given as [40],

$$erfi(\mathrm{y}) = \frac{erf(iy)}{i} = \frac{2}{\sqrt{\pi}}\int_0^{y} e^{t^2}\, dt. \tag{52}$$

Other TPs can be obtained as follows:

3.2 Mean energy $U(\beta)$

$$U(\beta) = -\frac{\partial}{\partial\beta} InZ(\beta), \tag{53}$$

3.3 Free energy $\mathrm{F}(\beta)$

$$F(\beta) = -KT \ln Z(\beta) \tag{54}$$

3.4 Entropy $\mathrm{S}(\beta)$

$$S(\beta) = K \ln Z(\beta) - K\beta \frac{\partial}{\partial\beta} \ln Z(\beta) \tag{55}$$

3.5 Specific heat capacity $\mathrm{C}(\beta)$

$$C(\beta) = \frac{\partial U}{\partial T} = -K\beta^2 \frac{\partial U}{\partial \beta} \tag{56}$$

4. Results and discussion

The prediction of the MS of the HMs is carried out using the relation [50,51]

$$M = 2m + E_{nl} \tag{57}$$

where m is quarkonium mass and E_{nl} is energy eigenvalues.

Plugging Eq. (26) into Eq. (57) gives,

$$\begin{aligned} M &= 2m + \frac{R_0}{2} - \frac{R_1}{12} - R_0 R_3 + \frac{3}{\delta}\left(-\frac{\sigma R_0}{12} + \frac{R_3\sigma^2}{2}\right) + \frac{6}{\delta^2}\left(\frac{R_1\sigma^2}{240} - \frac{R_3\sigma^3}{6}\right) \\ &- \frac{\hbar^2}{8\mu}\left[\frac{\frac{2\mu}{\hbar^2}\left(\frac{R_0}{\sigma} + R_2 - R_3\right) + \frac{6\mu}{\hbar^2\delta^2}\left(-\frac{\sigma R_0}{12} + \frac{R_3\sigma^2}{2}\right) + \frac{16\mu}{\hbar^2\delta^3}\left(\frac{R_1\sigma^2}{240} - \frac{R_3\sigma^3}{6}\right)}{n + \frac{1}{2} + \sqrt{\left(\frac{1}{2}+l\right)^2 + \frac{2\mu}{\hbar^2\delta^3}\left(-\frac{\sigma R_0}{12} + \frac{R_3\sigma^2}{2}\right) + \frac{6\mu}{\hbar^2\delta^4}\left(\frac{R_1\sigma^2}{240} - \frac{R_3\sigma^3}{6}\right) + \frac{2\mu R_1}{\hbar^2\sigma^2}}}\right]^2 \end{aligned} \tag{58}$$

The reduced mass is defined as $\mu = \frac{m}{2}$. For bottomonium and charmonium, the numerical values of these masses are $m_b = 4.823\, GeV$ and $m_c = 1.209\, GeV$, and the corresponding reduced mass is $\mu_b = 2.4115\, GeV$ and $\mu = 0.6045\, GeV$ correspondingly [52]. The potential parameters were also calculated by fitting with experimental data. Experimental data are taken from [53].

We observed that the results obtained from the prediction of mass spectra of charmonium and bottomonium for different quantum states are in agreement with experimental data and are seen to be improved when compared with other theoretical predictions with different analytical methods from literature as shown in Tables 1 and 2.

Table 1. Mass spectra of charmonium in (GeV)

$m_c = 1.209\ GeV, \mu = 0.6045\ GeV$, $\mathrm{R}_0 = 89960.89\ GeV$, $\mathrm{R}_1 = 0.230\ GeV, R_2 = -8.995999582 \times 10^6$ GeV,
$\mathrm{R}_3 = 0.5014478276$ GeV, σ=0.01, $\delta = 1.7\ GeV$, $\hbar = 1$

State	Present work	AIM [21]	LTM [17]	SEM [15]	Experiment [53]
1S	3.096	3.096	3.0963	3.095922	3.096
2S	3.686	3.686	3.5681	3.685893	3.686
1P	3.255	3.214	3.5687	-	3.525
2P	3.779	3.773	3.5687	3.756506	3.773
3S	4.040	4.275	4.0400	4.322881	4.040
4S	4.269	4.865	4.5119	4.989406	4.263
1D	3.504	3.412	4.0407	-	3.770
2D	4.146	-	-	-	4.159

Table 2: Mass spectra of bottomonium in (GeV)

$\left(m_b = 4.823\ GeV, \mu = 2.4115\ GeV,\ R_0 = 1.805186081 \times 10^6\ GeV,\ R_1 = 3.084\ GeV,\right.$
$\left. R_2 = -1.805170402 \times 10^8 \text{GeV}, R_3 = 0.5014694079\ \text{GeV},\ \sigma = 0.01, \delta = 1.70\ GeV, \hbar = 1\right)$

State	Present work	AIM [21]	LTM [17]	SEM [15]	Experiment [53]
1S	9.460	9.460	9.745	9.515194	9.460
2S	10.023	10.023	10.023	10.01801	10.023
1P	9.619	9.492	10.025	-	9.899
2P	10.114	10.038	10.303	10.09446	10.260
3S	10.355	10.585	10.302	10.44142	10.355
4S	10.567	11.148	10.580	10.85777	10.580
1D	9.864	9.551	10.303	-	10.164

In Fig. 1, we plotted the MS against the principal quantum number (PQN) for different values of angular quantum number. It was noticed that the MS first increases as the PQN increases and the latter tends to converge towards a point. The plots of the TPs are shown in Figs. (2-6). The partition function (PF) is plotted against temperature (β) at various values of maximum quantum number (λ) of 10 and 20. It was observed that the PF increases linearly as the β is increased. Figure 3 depict the variation of free energy (FE) with temperature at different values of λ . The FE increase at the beginning at the same rate as the temperature increases and then decreases and converge at a point when the FE is equal to 1. The plot of internal energy (IE) with temperature is shown in Fig 4. The IE is seen to increase exponentially at $\lambda = 10$ and when $\lambda = 20$ no increment was noticed. In Fig 5, the entropy is plotted against temperature. It was observed that the entropy increases with an increase in temperature for both values of λ . In Fig. 6, the plot of specific heat capacity with temperature is shown. A decrease is noticed when the temperature increases for different values of λ .

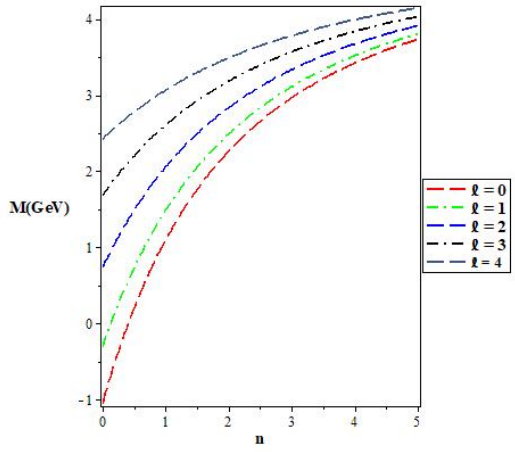

Figure 1. Variation of mass spectra with a principal quantum number for different angular quantum number

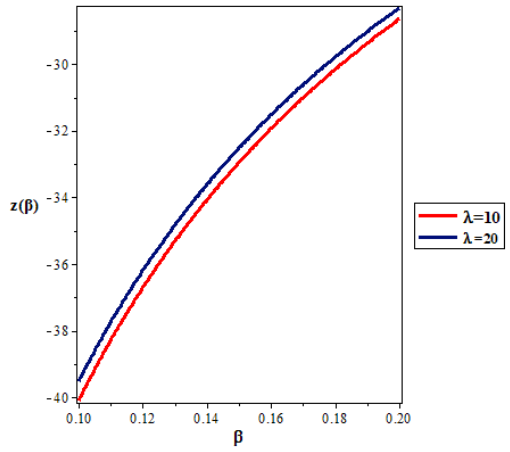

Figure 2. Variation of partition function with temperature for different values of λ

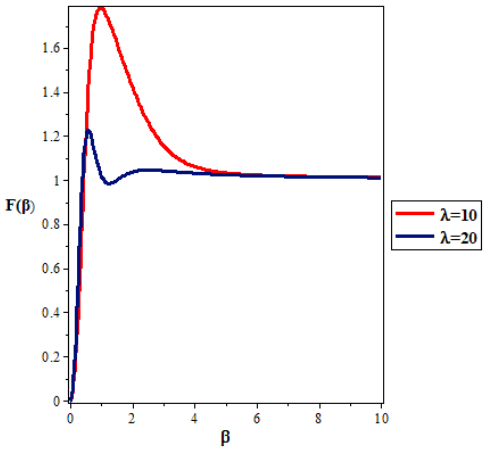

Figure 3. Variation of free energy with temperature for different values of λ

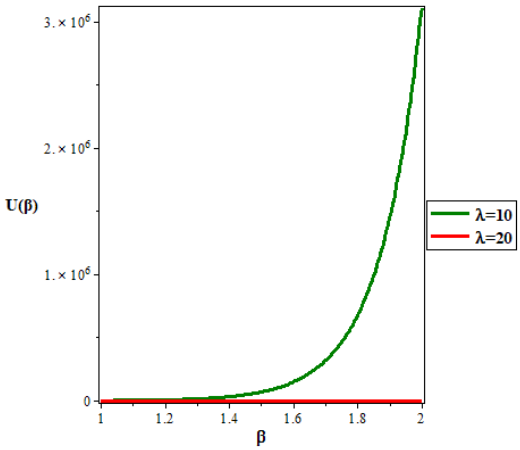

Figure 4. Variation of internal energy with temperature for different values of λ

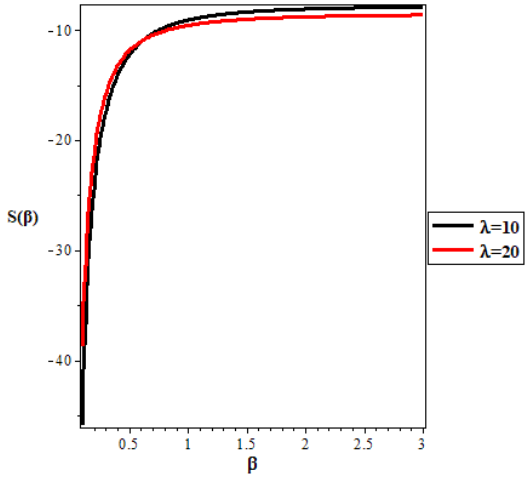

Figure 5. Variation of entropy with temperature for different values of λ

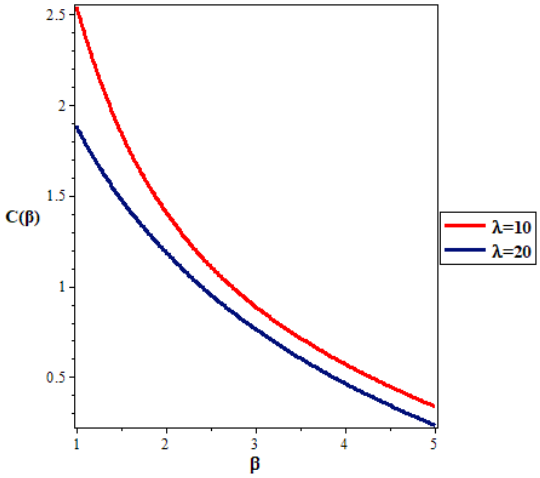

Figure 6. Variation of specific heart capacity with temperature for different values of λ

5. CONCLUSION

In this present study, the solutions of the SE were obtained with EHP using the NU method. The energy equation and normalized wave function were obtained. The energy spectrum was used to predict the MS of the HMs. Also, the PF was calculated from the energy equation, thereafter other TPs were obtained. The results obtained showed an improvement when compared with the work of other researchers and excellently agreed with experimental data.

Competing interests. The authors declare that they have no competing interests.

ORCID IDs

Etido P. Inyang, https://orcid.org/0000-0002-5031-3297; **Eddy S. William**, https://orcid.org/0000-0002-5247-5281
Ituen B. Okon, https://orcid.org/0000-0002-8172-7249

REFERENCES

[1] H. Ciftci, and H.F. Kisoglu, "Nonrelativistic-Arbitrary l-states of quarkonium through Asymptotic Iteration method", Advances in High Energy Physics, 4549705 (2018). https://doi.org/10.1155/2018/4549705

[2] H. Mutuk, "Mass Spectra and Decay constants of Heavy-light Mesons: A case study of QCD sum Rules and Quark model", Advan. in High Energy Phys. 8095653 (2018). https://doi.org/10.1155/2018/8095653

[3] M. Allosh, Y. Mustafa, N.K. Ahmed, and A.S. Mustafa, "Ground and Excited state mass spectra and properties of heavy-light mesons", Few-Body Syst. **62**, 26 (2021). https://doi.org/10.1007/s00601-021-01608-1

[4] E. Omugbe, O.E. Osafile, I.B. Okon, E.P. Inyang, E.S. William, and A. Jahanshir, "Any L-state energy of the spinlessSalpeter equation under the Cornell potential by the WKB Approximation method: An Application to mass spectra of mesons", Few-Body Systems, **63**(1), 7 (2022). https://doi.org/10.1007/s00601-021-01705-1

[5] E.S. William, E.P. Inyang, and E.A. Thompson, "Arbitrary ℓ-solutions of the Schrödinger equation interacting with Hulthén-Hellmann potential model", Revista Mexicana Fisica, **66,** 730 (2020). https://doi.org/10.31349/RevMexFis.66.730

[6] E. Omugbe, "Non-relativistic eigensolutions of molecular and heavy quarkonia interacting potentials via the Nikiforov-Uvarov method", Canadian Journal of Physics, **98**, 1125 (2020). https://doi.org/10.1139/cjp-2020-0039

[7] E.S. William, E.P. Inyang, I.O. Akpan, J.A. Obu, A.N. Nwachukwu, and E.P. Inyang, "Ro-vibrational energies and expectation values of selected diatomic molecules via Varshni plus modified Kratzer potential model", Indian Journal of Physics, (2022). https://doi.org/10.1007/s12648-022-02308-0

[8] E.P. Inyang, and E.O. Obisung, "The study of electronic states of NI and ScI molecules with screened Kratzer Potential", East Eur. J. Phys. **3**, 32 (2022). https://doi.org/10.26565/2312-4334-2022-3-04

[9] E.P. Inyang, E.S. William, E. Omugbe, E.P. Inyang, E.A. Ibanga, F. Ayedun, I.O. Akpan, and J.E. Ntibi, "Application of Eckart-Hellmann potential to study selected diatomic molecules using Nikiforov-Uvarov-Functional analysis method", Revista Mexicana de Fisica, **68**, 14 (2022). https://doi.org/10.31349/RevMexFis.68.020401

[10] E.P. Inyang, E.S.William , J.E.Ntibi, J.A.Obu, P.C.Iwuji, and E.P.Inyang "Approximate solutions of the Schrodinger equation with Hulthen plus screened Kratzer potential using the Nikiforov-Uvarov-Functional analysis method: An Application to diatomic molecules"., Canadian Journal of Physics (2022). https://doi.org/10.1139/cjp-2022-0030

[11] E.P. Inyang, E.P. Inyang, I.O. Akpan, J.E. Ntibi, and E.S.William, "Analytical solutions of the Schrödinger equation with class of Yukawa potential for a quarkonium system via series expansion method", European Journal of Applied Physics **2**, 26 (2020). http://dx.doi.org/10.24018/ejphysics.2020.2.6.26

[12] E.P. Inyang, P.C. Iwuji, J.E. Ntibi, E.S. William, and E.A. Ibanga, "Solutions of the Schrodinger equation with Hulthen –screened Kratzer potential: Application to diatomic molecules", East. Eur. J. Phys. **1**, 11 (2022). https://doi.org/10.26565/2312-4334-2022-2-02

[13] M. Abu-Shady, T.A. Abdel-Karim, and E.M. Khokha, "Exact solution of the N-dimensional Radial Schrödinger Equation via Laplace Transformation method with the Generalized Cornell potential", J. Quantum Phys. **45**, 587 (2018). https://doi.org/10.48550/arXiv.1802.02092

[14] E. Omugbe, O.E. Osafile, I.B. Okon, E.S. Eyube, E.P. Inyang, U.S. Okorie, A. Jahanshir, and C.A. Onate, "Non-relativistic bound state solutions with α-deformed Kratzer-type potential using the super-symmetric WKB method: application to theoretic-information measures", European Physical Journal D, **76**, 72 (2022), https://doi.org/10.1140/epjd/s10053-022-00395-6
[15] E. Omugbe, O.E. Osafile, E.P. Inyang, and A. Jahanshir, "Bound state solutions of the hyper-radial Klein-Gordon equation under the Deng-Fan potential by WKB and SWKB methods", Physica Scripta, **96**(12), 125408 (2021). https://doi.org/10.1088/1402-4896/ac38d4
[16] C.O. Edet, S. Mahmoud, E.P. Inyang, N. Ali, S.A. Aljunid, R. Endut, A.N. Ikot, and M. Asjad, "Non-Relativistic Treatment of the 2D Electron System Interacting via Varshni-Shukla Potential Using the Asymptoptic Iteration Method", Mathematics, **10**, 2824 (2022). https://doi.org/10.3390/math10152824
[17] M. Abu-shady, C.O. Edet, and A.N. Ikot, "Non-relativistic Quark model under external magnetic and Aharanov-Bohm (AB) fields in the presence of Temperature-Dependent confined Cornell potential", Canadian Journal of Physics, (2021) https://doi.org/10.11139/cjp-2020-0101
[18] R. Kumar, and F. Chand, "Asymptotic study to the N-dimensional Radial Schrodinder Equation for the quark-antiquark system", Commun. In Theor. Phys .**59**, 467 (2013). https://doi.org/10.1088/0253-6102/59/5/02
[19] J.P. Prasanth, K. Sebastian, and V.M. Bannur, "Revisiting Cornell potential model of the Quark-Gluon plasma", Physica A, **558**,124921 (2020). https://doi.org/10.1016/j.physa.2020.124921
[20] H. S. Chung, J. Lee, and D. Kang, "Cornel potential parameters for S-wave heavy quarkonia", Journal of the Korean physical society, **52**, 1151 (2008). https://doi.org/10.3938/jkps.52.1151
[21] R. Kumar, R.M. Singh, S.B. Bhahardivaj, R. Rani, and F. Chand, "Analytical solutions to the Schrodinger equation for generalized Cornell potential and its application to diatomic molecules and heavy mesons", Mod. Phys. Lett. A. **37**, 2250010 (2022). https://doi.org/10.1142/S0217732322500109
[22] A. Vega, and J. Flores, "Heavy quarkonium properties from Cornell potential using variational method and supersymmetric quantum mechanics", Pramana – J. Phys. **87**, 73 (2016). https://doi.org/10.1007/s12043-016-1278-7
[23] H. Mutuk, "Cornell Potential: A Neural Network Approach", Advan. in High Energy Phys. **22,** 3105373 (2019). https://doi.org/10.1155/2019/3105373
[24] H. Hassanabadi, M. Ghafourian, and S. Rahmani, "Study of the Heavy-Light mesons properties via the Variational method for Cornell interaction", Few-Body Syst. **57**, 249 (2016). https://doi.org/10.1007/s00601-015-1040-6
[25] M. Abu-Shady, and S.Y. Ezz-Alarab, "Trigonometric Rosen–Morse Potential as a Quark–Antiquark Interaction Potential for Meson Properties in the Non-relativistic Quark Model Using EAIM". Few-Body Systems, **60**, 66 (2019). https://doi.org/10.1007/s00601-019-1531-y
[26] M. Abu-shady, H.M. Mansour, and A.I. Ahmador, "Dissociation of Quarkonium in Hot and Dense media in an Anisotropic plasma in the Non-relativistic Quark model", Advances in High Energy Physics, 4785615 (2019). https://doi.org/10.1155/2019/4785615
[27] E.P. Inyang, E.P. Inyang, J.E. Ntibi, E.E. Ibekwe, and E.S. William, **"**Approximate solutions of D-dimensional Klein-Gordon equation with Yukawa potential via Nikiforov-Uvarov method**",** Indian Journal of Physics, **95**, 2733 (2021). https://doi.org/10.1007/s12648-020-01933-x
[28] E.P. Inyang, E.P. Inyang, E.S. William, and E.E. Ibekwe, "Study on the applicability of Varshni potential to predict the mass-spectra of the Quark-Antiquark systems in a non-relativistic framework", Jordan Journal of Physics, **14**, 337 (2021). https://journals.yu.edu.jo/jjp/Draft/Vol14No4/8-%20Study%20on%20the%20Applicability,%20Inyang%20et%20al.pdf
[29] E.E. Ibekwe, U.S. Okorie, J.B. Emah, E.P. Inyang, and S.A. Ekong, "Mass spectrum of heavy quarkonium for screened Kratzer potential (SKP) using series expansion method", Eur. Phys. J. Plus, **87**, 136 (2021). https://doi.org/10.1140/epjp/s13360-021-01090-y
[30] I.O. Akpan, E.P. Inyang, E.P. Inyang, and E.S. William, "Approximate solutions of the Schrödinger equation with Hulthen-Hellmann Potentials for a Quarkonium system", Revista Mexica De Fisica, **67**, 482 (2021). https://doi.org/10.31349/RevMexFis.67.482
[31] K.R. Purohit, P. Jakhad, and A.K. Rai, "Quarkonium spectroscopy of the linear plus modified Yukawa potential", Phys. Scripta, **97**, 044002 (2022). https://doi.org/10.1088/1402-4896/ac5bc2
[32] S. Patel, P.C. Vinodkumar, and S. Bhatnagar, "Decay rates of charmonia within a quark-antiquark confining potential", Chinese Physics C, **40**, 053102 (2016). https://doi.org/10.1088/1674-1137/40/5/053102
[33] V. Mateu, P.G. Ortega, D.R. Entem, and F. Fernadez, "Calibrating the nave Cornell model with NRQCD", The European Physical Journal C, **79**, 323 (2019). https://doi.org/10.1140/epjc/s10052-019-6808-2
[34] F. Brau, and C. Sernay, "The three-dimensional Fourier grid Hamiltonian method", Journal of computational physics, **139**, 136 (1998). https://doi.org/10.1006/jcph.1997.5866
[35] A. Bhaghyesh, "Charmonium properties using the Discrete variable representation (DVR) method", Advances in High Energy Physics, 9991152 (2021). https://doi.org/10.1155/2021/9991152
[36] S. Jacobs, M.G. Olsson, and C. Suchyta, "Comparing the Schrodinger and Spinless Salpeter equations for heavy-quark bound states", Physical Review D, **33**, 3338 (1986). https://doi.org/10.1103/physrevd.33.3338
[37] B. Grinstein, "A modern introduction to quarkonium theory", International Journal of Modern Physics, **15**, 461 (2000). https://doi.org/10.1142/S0217751X00000227
[38] W. Lucha, F. Schoberl, and D. Gromes, "Bound states of quarks", Physics Reports, **200**, 127 (1991). https://doi.org/10.1016/0370-1573(91)90001-3
[39] E. P. Inyang, A.N.Ikot, I.O.Akpan, J.E.Ntibi, E.Omugbe, and E. S. William, "Analytic study of thermal properties and masses of heavy mesons with quarkonium potential", Result in Physics. (2022) 105754. https://doi.org/10.1016/j.rinp.2022.105754
[40] E.P. Inyang, E.P. Inyang, I.O. Akpan, J.E. Ntibi, and E.S. William, "Masses and thermodynamic properties of a Quarkonium system", Canadian Journal Physics, **99**, 990 (2021). https://doi.org/10.1139/cjp-2020-0578
[41] E.P. Inyang, E.O. Obisung, P.C. Iwuji, J.E. Ntibi, J. Amajama, and E.S. William, "Masses and thermal properties of a charmonium and Bottomonium mesons", J. Nig. Soc. Phys. Sci. 4 (2022). https://doi.org/884.10.46481/jnsps.2022.884

[42] C. Eckart, "The Penetration of a potential Barrier by Electrons", Phys. Rev. **35**, 1303 (1930). https://doi.org/10.1103/PhysRev.35.1303
[43] H. Hellmann, "A New Approximation Method in the Problem of Many Electrons", J. Chem. Phys. **3**, 61 (1935). https://doi.org/10.1063/1.1749559
[44] C.A. Onate, J.O. Ojonubah, A. Adeoti, E.J. Eweh, and M. Ugboja, "Approximate Eigen Solutions of D.K.P. and Klein-Gordon Equations with Hellmann Potential", Afr. Rev. Phys. **9**, 497 (2014). http://eprints.lmu.edu.ng/1594/1/ONATE%2032.pdf
[45] E.P. Inyang, E.S. William, J.O. Obu, B.I. Ita, E.P. Inyang, and I.O. Akpan, "Energy spectra and expectation values of selected diatomic molecules through the solutions of Klein-Gordon equation with Eckart-Hellmann potential model", Molecular Physics, **119**(23), e1956615 (2021). https://doi.org/10.1080/00268976.2021.1956615
[46] S.K. Nikiforov, and V.B. Uvarov. *Special functions of Mathematical Physics*, (Birkhauser, Basel, 1988)
[47] E.P. Inyang, E.S. William, and J.A. Obu, "Eigensolutions of the N-dimensional Schrödinger equation` interacting with Varshni-Hulthen potential model", Rev. Mexi. Fisi. **67**, 193 (2021). https://doi.org/10.31349/RevMexFis.67.193
[48] M. Abu-Shady, "N-dimensional Schrödinger equation at finite temperature using the Nikiforov-Uvarov method", J. Egypt. Math. Soc. **23**, 4 (2016). https://doi.org/10.1016/j.joems.2016.06.006
[49] I.S. Gradshteyn, and I.M. Ryzhik, *Tables of integrals, series and product, 7th ed*. (Academic Press, Boston, 2007).
[50] E.P. Inyang, E.P. Inyang, J. Karniliyus, J.E. Ntibi, and E.S. William, "Diatomic molecules and mass spectrum of heavy quarkonium system with Kratzer-screened Coulomb potential (KSCP) through the solutions of the Schrödinger equation", European Journal of Applied Physics, **3**, 55 (2021). https://doi.org/10.24018/ejphysics.2021.3.2.61
[51] E.P. Inyang, P.C. Iwuji, J.E. Ntibi, E. Omugbe, E.A. Ibanga, and E.S. William "Quark-antiquark study with inversely quadratic Yukawa potential using Nikiforov-Uvarov-Functional analysis method", East Eur. J. Phys. **2**, 43 (2022), https://periodicals.karazin.ua/eejp/article/view/18535/16839
[52] R. Olive, D.E. Groom, and T.G. Trippe, "Particle Data Group", Chin. Phys. C, **38**, 60 (2014).
[53] M. Tanabashi, C.D. Carone, T.G. Trippe, and C.G. Wohl, Particle Data Group, Phys. Rev. D, **98**, 546 (2018).

НЕРЕЛЯТИВІСТСЬКЕ ДОСЛІДЖЕННЯ МАС-СПЕКТРІВ І ТЕПЛОВИХ ВЛАСТИВОСТЕЙ КВАРКОНІЄВОЇ СИСТЕМИ З ПОТЕНЦІАЛОМ ЕКАРТА-ГЕЛЬМАНА

Етідо П. Іньянг[a], Еффіонг О. Обісунг[d], Едді С. Вільям[b], Ітуен Б. Окон[c]
[a]Фізичний факультет, Національний відкритий університет Нігерії, Джабі-Абуджа, Нігерія
[b]Група теоретичної фізики, Фізичний факультет, Університет Калабара, PMB 1115, Калабар, Нігерія
[c]Група теоретичної фізики, Фізичний факультет, Університет Уйо, Нігерія
[d]Фізичний факультет, Університет Калабара, PMB 1115, Калабар, Нігерія

У цьому дослідженні ми моделюємо потенціал Екарта-Гельмана (EHP) для взаємодії в системі кварк-антикварк. Розв'язки рівняння Шредінгера отримані з ЕГП методом Нікіфорова-Уварова. Отримано рівняння енергії та нормовану хвильову функцію. Маси важких мезонів, таких як чармоній ($c\bar{c}$) і боттоній ($b\bar{b}$), для різних квантових чисел були передбачені за допомогою рівняння енергії. Крім того, розподільча функція була розрахована з рівняння енергії, після чого були отримані інші теплові властивості, такі як середня енергія, вільна енергія, ентропія та питома теплоємність. Отримані результати показали покращення порівняно з роботами інших дослідників і чудово узгоджувалися з експериментальними даними.

Ключові слова: рівняння Шредінгера; метод Нікіфорова-Уварова; потенціал Екарта-Гельмана; важкі мезони; теплові властивості